A FINITE ELEMENT ANALYSIS OF THE MONOLITHIC DOME

by

Nanette South

A thesis

Submitted in partial fulfillment

of the requirements for the degree of

Master of Science in Engineering Structures and Mechanics

Idaho State University

December 2005

To the Graduate Faculty:

The members of the committee appointed to examine the thesis of NANETTE SOUTH find it satisfactory and recommend that it be accepted.

Habib Sadid

Major Advisor:
Dr. Habib Sadid

Arya Ebrahimpour

Committee Member:
Dr. Arya Ebrahimpour

Linda Hill.

Graduate Faculty Representative:
Dr. Linda Hill

Acknowledgements

I would like to thank my thesis advisor, Dr. Habib Sadid, for his encouragement and help in my educational pursuits. I would like to thank my parents who have supported and inspired me throughout my education. Their unconditional love, support, and encouragement were crucial to my success. Thanks to my siblings, Sarah, Jenny, David, Melinda, Rebecca, Jessica, Michael, and Jamie who helped me pursue my education in any way they could and knew how. Finally, I would like to thank my children, Matthew, Kaleb, Erika, and Sydney, for their love and understanding throughout this difficult process. They have been a source of unwavering support for which I am truly grateful. They are an inspiration to me.

TABLE OF CONTENTS

List of Figures i

List of Tables v

Abstract vi

Chapter 1: An Introduction to the History of Thin-Shell Dome Structures in the U.S. and Monolithic Domes 1

Chapter 2: An Introduction to Shell Theory 11

Chapter 3: An Introduction to Finite Element Analysis and NE/Nastran 19

Chapter 4: A Comparison between Shell Theory and FEA for a Hemispherical Dome 30

Chapter 5: A Comparison between Shell Theory and FEA for a Truncated Dome 48

Chapter 6: A Comparison between Shell Theory and FEA for a Non-Hemispherical Dome 54

Chapter 7: An Introduction to Shell Theory for Domes, Rings, and Wall Interactions 59

Chapter 8: Dome-Ring-Wall Example and Comparison, 69

Chapter 9: Buckling Analysis of Truncated Monolithic Dome using Finite Element Analysis 76

Chapter 10: Conclusions 97

References 98

List of Figures

Figure 1-1 - The Hayden Planetarium on West 81st Street in New York City 2

Figure 1-2 - Hershey Arena under Construction 4

Figure 1-3 - Palazzo delle Esposizioni 5

Figure 1-4 - Algeciras Market 6

Figure 1-5 - Exterior View of Queensgate Market 7

Figure 1-6 - The Monolithic Dome Construction 10

Figure 2-1 - Definitions for domes from Billington 13

Figure 2-2 - Dome Forms from Billington 15

Figure 2-3 - Dome Equilibrium from Billington 17

Figure 3-1 - Various Types of Finite Elements from Logan 21

Figure 4-1 - Rough Mesh of 56m Span Hemispherical Dome in NASTRAN 31

Figure 4-2 - Distribution of Hoop Stresses for Roughly Meshed 56m Span Dome 32

Figure 4-3 - Distribution of Meridional Stresses for Roughly Meshed 56m Span Dome 32

Figure 4-4 - Medium Mesh of 56m Span Hemispherical Dome in NASTRAN 33

Figure 4-5 - Distribution of Hoop Stresses for Medium Mesh of 56m Span Dome 34

Figure 4-6 - Distribution of Meridional Stresses for Medium Mesh of 56m Span Dome 34

Figure 4-7 - Fine Mesh of 56m Span Hemispherical Dome in NASTRAN 35

Figure 4-8 - Distribution of Hoop Stresses for Fine Mesh of 56m Span Dome 36

Figure 4-9 - Distribution of Meridional Stresses for Fine Mesh of 56m Span Dome 36

Figure 4-10 - Height vs. Fx for 56m Span Hemispherical Dome 39

Figure 4-11 - Height vs. Fy for 56m Span Hemispherical Dome 40

Figure 4-12 - Height vs. X-Moments for 56m Span Hemispherical Dome 41

Figure 4-13 - Height vs. Y-Moments for 56m Span Hemispherical Dome 42

Figure 4-14 - Comparison of FEA and Shell Theory with Height vs. Hoop Stress for 56m Span Hemispherical Dome. 45

Figure 4-15 - Comparison of FEA and Shell Theory with Height vs. Meridional Stress for 56m Span Hemispherical Dome. 46

Figure 5-1 - Fine Mesh of 56m Span Truncated Hemispherical Dome in NASTRAN 50

Figure 5-2 - Distribution of Hoop Stresses for Truncated 56m Span Dome 51

Figure 5-3 - Distribution of Meridional Stresses for Truncated of 56m Span Dome 51

Figure 5-4 - Meridional Stress Distribution around opening 52

Figure 5-5 - Hoop Stress Distribution around opening 53

Figure 6-1 - Fixed Dome for Comparison Between FEA and Billington Example 54

Figure 6-2 - Meridional Force Distribution in Dome 56

Figure 6-3 - Hoop Force Distribution in Dome 57

Figure 6-4 - Moment Distribution in Dome 58

Figure 7-1 - Dome Edge Reactions from Billington 59

Figure 7-2 - Dome Edge Constructions from Billington. (a) Dome-Ring Edge Construction, (b) Dome-Wall Edge Construction, (c) Dome-Ring-Wall Edge Construction. 60

Figure 7-3 - Dome-Ring Analysis from Billington 61

Figure 7-4 - Dome-Ring-Wall Analysis from Billington 65

Figure 8-1 - Texhoma, Oklahoma-- Texhoma School District 69

Figure 8-2 - Domed Tank Dimensions from Billington 70

Figure 8-3 - Idealization of Dome-Ring-Wall Junctions for FEA from Billington 71

Figure 8-4 - Hoop Force Distribution in Water Tank 72

Figure 8-5 - Meridional Force Distribution in Water Tank 73

Figure 8-6 - Distribution of Moment in Water Tank 74

Figure 9-1 - Faith Chapel Christian Center 76

Figure 9-2 - Layout of the Planned Expansion for Faith Chapel 77

Figure 9-3 - Plexiglass Tower Spanning 12 ft. Diameter Skylight at Apex of Dome 78

Figure 9-4 - Load Application Points on 18 ft. Diameter Circle around 12 ft. Diameter Skylight. 80

Figure 9-5 - Controlling Eigenvalue, $\lambda = 140.14960$, for Buckling Analysis 83

Figure 9-6 - Controlling Buckling Mode Shape Associated with $\lambda = 140.14960$ 84

Figure 9-7 - 101.5 ft. diameter hemisphere with 1′ x 1′ ribs 20′ long at 30° off 2′ x 1′ ring at top of dome around 12′ diameter skylight 85

Figure 9-8 - Controlling Buckling Eigenvalue $\lambda_{40} = 97.916557$ for 101.5 ft. diameter hemisphere with 1′ x 1′ ribs 20′ long at 30° off 2′ x 1′ ring at top of dome around 12′ diameter skylight. Shell thickness = 4in. 86

Figure 9-9 - Controlling Buckling Mode Shape Associated with $\lambda_{40} = 97.916557$ 87

Figure 9-10 - Controlling Buckling Eigenvalue $\lambda_{49} = 129.$ for 101.5 ft. diameter hemisphere with 1′ x 1′ ribs 20′ long at 30° off 2′ x 1′ ring at top of dome around 12′ diameter skylight. Shell thickness = 5 in. 88

Figure 9-11 - Controlling Buckling Mode Shape Associated with $\lambda_{49} = 129$ 89

Figure 9-12 - Ring Beam, Radial Ribs, and Transverse Ribs around Skylight Opening 90

Figure 9-13 - Controlling Buckling Eigenvalue λ = 141 for 101.5 ft. diameter hemisphere with 1′ x 1′ radial ribs 20′ long at 30° off 2′ x 1′ ring at top of dome around 12′ diameter skylight. Two 1′x1′ transverse ribs are located at 10′ and 20′ from ring beam. Shell thickness = 5in. 91

Figure 9-14 - Controlling Buckling Mode Shape Associated with λ = 141 92

Figure 9-15 - Hoop Stresses at the Top of Ribbed Dome. Maximum stress = -21 ksf. Maximum stress at top of dome = -17 ksf. 93

Figure 9-16 - Meridional Stresses at the Top of Ribbed Dome. Maximum stress = -21 ksf. Maximum stress at top of dome = -17 ksf. 94

Figure 9-17 - Mx = -0.603 kips-ft/ft at top of dome 95

Figure 9-18 - My = -0.4 kips-ft/ft at top of dome 95

List of Tables

Table 4-1 - Shell Theory vs. FEA Stress Results for 56m Span Hemispherical Dome 35

Table 4-2 - Elements, Forces, and Moments from Bottom Edge to Apex of 56m Span Dome 37

Table 4-3 - Comparison of Stresses Between FEA and Theory from Bottom Edge to Apex of 56m Span Dome 42

Table 5-1 - Shell Theory vs. FEA Stress Results for 56m Span Hemispherical Truncated Dome 50

Table 6-1 - Forces in a Spherical Dome on Fixed Supports 55

Table 6-2 - Shell Theory Results vs. Finite Element Analysis Results 58

Table 7-1 - Displacements for Dome-Ring-Wall Analysis (Errors) (Rectangular ring cross section) 66

Table 8-1 - Comparison of Forces and Moments Between Dome-Ring Solution and FEA 74

A FINITE ELEMENT ANALYSIS
OF THE MONOLITHIC DOME
Thesis Abstract—Idaho State University (2005)

Four of the major influences in the history of thin-shell structures are discussed. David B. South and his brothers, Barry and Randy South, are presented as the inventors of the Monolithic Dome. Monolithic Domes are thin-shell structures constructed by applying polyurethane foam to the interior surface of an airform followed by attaching rebar to the foam. About three inches of shotcrete is then sprayed onto the interior surface. Basic stress resultants are developed from membrane theory as presented by David P. Billington. The finite element analysis process (FEA) is discussed as well as an introduction to NE/NASTRAN, a finite element analysis program. Comparisons of stress resultants between shell theory and FEA are made for a hemispherical dome, a truncated, hemispherical dome, and a non-hemispherical dome. Shell theory for domes, rings and wall interactions is introduced to facilitate a comparison between theory and FEA for the dome-ring-wall problem. Finally, a finite element buckling analysis is presented for a non-hemispherical, truncated dome with a tower. The current design practice utilizes shell theory. The finite element analysis process was found to be very accurate when compared with shell theory results and more powerful when complicated problems were presented.

Chapter 1

AN INTRODUCTION TO THE HISTORY OF THIN-SHELL DOME STRUCTURES IN THE U.S. AND MONOLITHIC DOMES

In the history of thin-shell structures, four of the major influences are: Anton Tedesko (1903-1994), who is attributed with much of the success of thin-shell structures in the U.S; Pier Luigi Nervi (1891-1979), who in Italy gave structural integrity to the complex curves and geometry of reinforced-concrete structures such as the Orbetello aircraft hangar (begun 1938) and Turin's exposition hall (1948-50); and the Spaniard Eduardo Torroja (1891-1961) and his pupil Felix Candela (1910-1997) who followed his lead. Essentially, each of the latter three attempted to create an umbrella roof the interior space of which could be subdivided as required, such as Torroja's grandstand for the Zarzuela racetrack in Madrid (1935) (16).

The Monolithic Dome, as examined in this thesis, can be attributed to David B. South (1939-). David B. South, president of the Monolithic Dome Institute, and his brothers - Barry and Randy South - developed an efficient method for building a strong dome using a continuous spray-in-place process. In 1976, after years of planning and development they built the first Monolithic Dome in Shelley, Idaho (18).

Anton Tedesko (1903-1994)

Tedesko's contribution to the history of thin-shell dome structures in the United States began in Germany. During the early twentieth century, planetariums became very popular in Europe and the U.S. The Carl Zeiss Company of Germany was one of the leading manufacturers of the machinery that produced the sky shows. The problem in the early 1900's was that the quality of the space used for viewing rarely matched the quality of the projector. Thus, The Carl Zeiss Company sought a high-quality dome design that could be produced efficiently. Zeiss hired engineers, Dyckerhoff and Widmann, who created the solution known as the "Zeiss Dywidag System." This system was patented in the U.S. and licensed to the Roberts & Schaefer Company in Chicago, which employed the structural engineer, Anton Tedesko, who had worked with Zeiss in Europe (2).

The introduction and success of thin-shell structures in the United States is attributed to Anton Tedesko, according to Hines and Billington. They assert that Tedesko's introduction of thin concrete shells in the U.S. is captured in the story of three structures: a hemispherical dome (Hayden Planetarium), a small set of long barrels (Brook Hill Farm Dairy Exhibit at the 1933 "Century of Progress" World's Fair in Chicago, Illinois using the Z-D system), and a large wide-spanning, short barrel roof (Hershey Sports Arena). All were built within three years of each other.

Hines and Billington say that Tedesko succeeded in arranging that the Hayden Planetarium be the first full-scale American thin concrete shell, see Figure 1-1. He insisted that the dome be built on more traditional falsework than on the Zeiss network from Germany. Tedesko served as the principal advisor to the Weiskopf and Pickworth engineers, to whom he gave copious amounts of calculations as guidelines.

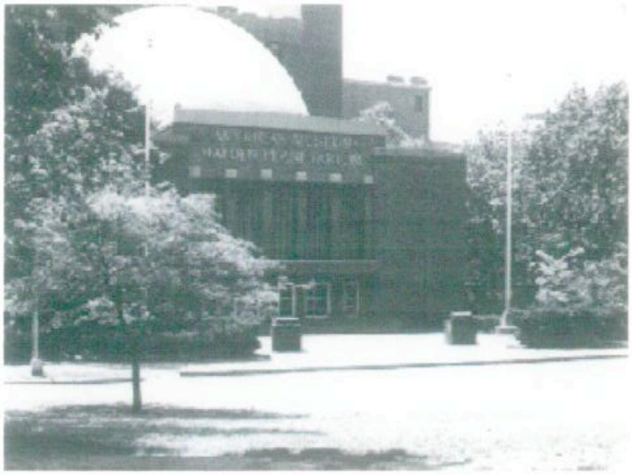

Figure 1-1 - The front entrance to the original Hayden Planetarium on West 81st Street in New York City (2).

For the World's Fair in 1933, Tedesko failed to obtain the contract for theGerman Pavilion but did get the stalls for Brook Hill Farm's dairy exhibit. Since the Brook Hill stalls were temporary, Tedesko tested them under ultimate loads before taking them down after the Fair. Thus, Roberts and Schaefer published the first load tests carried out on barrel shells in the United States (Hines and Billington).

A memorial tribute in the National Academy of Engineering journal says that the Depression slowed the progress of thin shell construction. There were many designs and few built structures. One of the first major breakthroughs was when the Hershey Chocolate Company wanted to build a shell structure for a sports arena. According to the Hershey Community Archives, Mr. Hershey had asked D. Paul Witmer, manager of the Hershey Lumber Company to solicit plans for a new building. Through a contact with the Portland Cement Company, Witmer was put in touch with Anton Tedesko. On January 21, 1936, Tedesko presented his idea for a huge arena to Mr. Witmer, who then presented it to Milton Hershey. After some initial skepticism, Mr. Hershey became excited by the innovation and gave his approval. Ground was broken on March 11, 1936.

The Archives state that the Sports Arena is composed of a barrel vault roof—the Zeiss-Dywidag type. The concrete shell is 3.5 in. thick at the uppermost part, and is stiffened at 39 foot intervals by massive two-hinged arch ribs. The roof crown is 100 feet above the floor. The shell was constructed as five separate units, with expansion joints between units. The journal from the National Academy of Engineering states that Tedesko established his own rules for the design and construction which were later adopted by the industry. According to the Hershey archives, when it opened on December 19, 1936, the Hershey Arena was the first large scale barrel shell roof structure in the U.S. (See Figure 1-2). Its construction established Anton Tedesko as the preeminent engineer for such structures.

Figure 1-2 – Hershey Arena Under Construction (4).

Publicity from the Hershey Arena opened the door for other shell structures and during World War II, Tedesko was the manager of the Roberts and Schaefer office in Washington, where, according to the National Academy of Engineering, the Army, Navy, and Air Force had many shells designed for their installations.

Pier Luigi Nervi (1891 – 1979)

Pier Luigi Nervi also influenced the development of thin-shell structures in the United States. According to Sara Askari (5), Nervi was born in the town of Sondrio in the Italian Alps. He attended the University of Bologna and joined the army engineering corps and a group called "The Society for Concrete Construction" following World War I. It was not until after he left the group in 1923 that his unique approach to building garnered critical attention. In 1926-27 he designed the Cinema Augusteo in Naples, and two years later he began work on the Municipal Stadium in Florence. Between 1935 and 1943 Nervi dedicated himself to studies of the covering construction of very big dimensions. Figure 1-3 shows an example of this work in the cover of the hall in Palazzo delle Esposizioni in Turino—1948 (6).

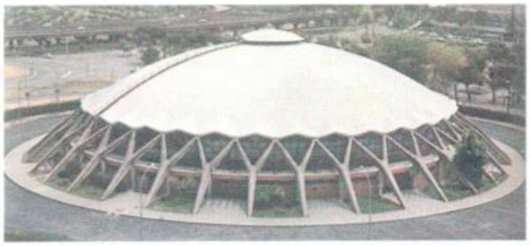

Figure 1-3—Palazzo delle Esposizioni (5).

According to Askari, after World War II, Nervi made a breakthrough in the field of reinforced concrete: the invention of ferro-cemento. Ferro-cemento used steel mesh as a core and layers of cement were brushed on top. The mesh was thin, flexible, and elastic. Ferro-cemento enabled Nervi to design any form he wanted. Ferro-cemento could easily be prefabricated in plaster molds. Over the next thirty years Nervi took on about twenty-five concrete projects. Just after WWII, he designed the Turin Exhibition Hall which has been hailed as "one of the most impressive interior spaces of the century." He built the George Washington Bridge bus terminal in New York City which one critic compared to "an alighted butterfly."

Other Nervi buildings in the United States include a field house for Dartmouth College and the Cathedral of San Francisco. For his work he was awarded an honorary degree by Harvard University and given the gold medal of the American Institute of Architects (7).

Eduardo Torroja (1891 – 1961)

Eduardo Torroja was a Spanish architect and engineer notable as a pioneer in the design of concrete-shell structures. Torroja graduated as an engineer in 1923 and began working with a contractor. He became a consulting engineer in 1927 (12). With José Maria Aguirre he founded, in 1934, an experimental institute to develop new uses and theories for reinforced concrete. An example of his building technique is the Algeciras market in Spain built in 1933 (see Figure 1-4) (14). This concrete structure has a 48 m. diameter shell placed over eight pillars joined by a prestressed tie beam (15).

Figure 1-4—Algeciras Market (13).

Torroja built a water reservoir for Madrid in 1936 and in 1939 he became a Professor at the Escuela de Caminos in Madrid as well as Director of the Instituto Tecnico de la Construccion y del Cemento (13).

Felix Candela (1910 – 1997)

A student of Eduardo Torroja, Felix Candela was born in Madrid in 1910. He entered Madrid's Escuela Superior de Arquitectura in 1927 and graduated in 1935. Sidetracked by his political struggle against Franco, he did not practice architecture until he immigrated to Mexico in 1939 (8).

Felix Candela did not invent the concrete shell nor was he the first to use hyperbolic parabaloids, but the Huddersfield Gem website asserts he was the all time greatest practitioner of shell design, citing his light, audaciously thin structures revealing engineering of great sophistication. His name has become synonymous with the hyperbolic parabaloid (hypar) (11).

His development of the hypar umbrella with four tympans was groundbreaking for architects and engineers and highly influential. This influence is clear in the Queensgate market (8). Queensgate Market, Huddersfield, opened in 1970, replacing the previous 1878 market building. The striking feature of the interior is its roof structure, based on 21 asymmetric hyperbolic paraboloids (hypar) which appear like giant mushrooms (See Figure 1-5) (19).

Figure 1-5—Exterior View of Queensgate Market (19).

Candella believed that strength should come from form, not mass. This belief led to an extensive exploration of tensile shell structures. His nickname became "The Shell Builder" because of this structural favoritism (8). The encyclopedia Brittanica calls Felix Candela a "designer of reinforced-concrete (ferroconcrete) structures distinguished by thin, curved shells that are extremely strong and unusually economical." (9)

Frequently forced to act as architect, structural engineer and contractor in order to further his work, Candella saw architects as engineers who possess the ability to design both great cathedrals and low cost housing (8).

From 1949 he built, designed or engineered hundreds of ferro concrete structures. Among his best-known works are the Cosmic Ray Pavilion (1950–51) for Mexico's University City; the Church of La Virgen Milagrosa (1953), Mexico City; and Los Manantiales restaurant (1958), Xochimilco (10).

In 1961, Felix Candela was awarded the gold medal of the institution of Structural Engineers (11).

David B. South (1939 -)

The Monolithic story begins with David B. South and his interest in dome building. That interest started when David was still in high school and never waned. In fact, it intensified. By 1975, David and his two brothers, Barry and Randy, had successfully built their first Monolithic Dome-- a potato storage facility in Shelley, Idaho, 105' in diameter and 35' high (17).

In 1979, the first patent was awarded for the Monolithic Dome construction process. And since 1976, Monolithic Domes have been constructed in 45 states and many foreign countries (18).

The Monolithic Dome Construction Process

A Monolithic Dome starts as a concrete ring foundation reinforced with steel rebar. Vertical steel bars embedded in the ring beam footing are later attached to the steel reinforcing of the dome itself (18).

The Airform, fabricated to a proper shape and size, is attached to the concrete base. Using fans, the Airform is inflated - creating the shape of the dome. The Airform is both the form for construction of the dome and the outer roof membrane of the shell when it is finished. Inflator fans run throughout the construction of the dome shell (18).

Approximately three inches of polyurethane foam insulation is applied to the interior surface of the Airform. Then, steel reinforcing bars, or rebar, are attached to the foam using special hooks embedded in the foam. The rebar is placed in a specially engineered layout of hoop (horizontal) and vertical steel rebar (18).

Shotcrete, a special spray mix of concrete, is sprayed onto the interior surface of the polyurethane foam, embedding the rebar. After three inches of shotcrete is applied, the Monolithic Dome is a steel reinforced concrete structure (See Figure 1-6), (18).

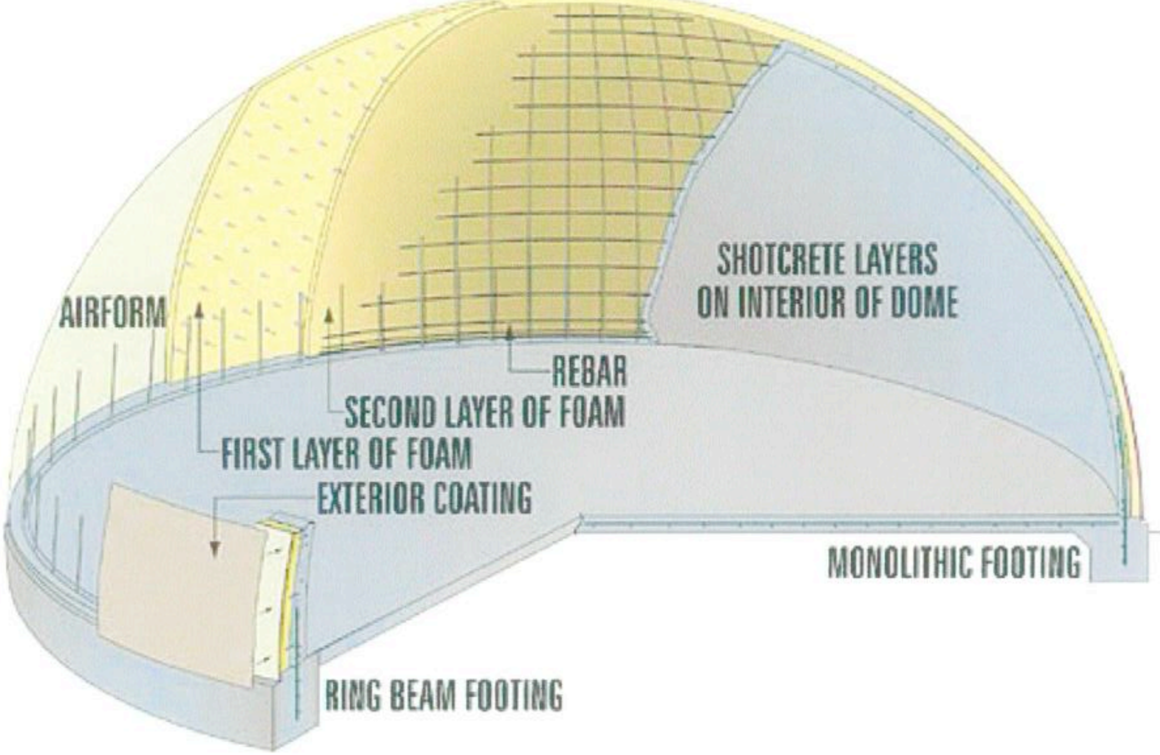

Figure 1-6—The Monolithic Dome Construction (18).

Chapter 2

AN INTRODUCTION TO SHELL THEORY

To make a comparison between the finite element analysis of the strength of the Monolithic Dome and theory, the traditional shell equations and stress resultants must be introduced.

The development of the stress resultants from membrane theory as presented in Billington's "Thin Shell Concrete Structures" are the foundations for modern day dome analysis.

Figure 2-1 defines a differential shell element in the spherical coordinate system. For a shell of revolution, due to symmetry in the static equilibrium equations, all purely geometric terms involving $\partial\theta$ vanish and we find for domes the equations:

$$\frac{\partial N'_{\theta}}{\partial \theta} r_1 + N_{\theta\phi} \frac{\partial r_o}{\partial \phi} + \frac{\partial (N'_{\phi\theta} r_o)}{\partial \phi} + p_{\theta} r_o r_1 = 0$$

$$\frac{\partial (N'_{\phi} r_o)}{\partial \phi} - N'_{\phi} \frac{\partial r_o}{\partial \phi} + \frac{\partial N'_{\theta\phi}}{\partial \theta} r_1 + p_{\phi} r_o r_1 = 0 \qquad \boxed{(2\text{-}1)}$$

$$\frac{N'_{\theta}}{r_2} + \frac{N'_{\phi}}{r_1} + p_z = 0$$

Then, when the loading is symmetrical with respect to the axis, all terms involving ∂θ vanish and the partial differential terms, ∂φ, can now be written as ordinary differentials dφ since nothing varies with θ. The circumferential component of load, p_θ, is zero, and the shear stress resultants vanish along the meridians and parallel circles. Therefore, the first equation vanishes and the remaining two reduce to:

$$\frac{d(N'_\phi r_o)}{d\phi} - N'_\theta \frac{dr_o}{d\phi} + p_\phi r_o r_1 = 0 \qquad \boxed{(2\text{-}2)}$$

$$\frac{N'_\theta}{r_2} + \frac{N'_\phi}{r_1} + p_z = 0$$

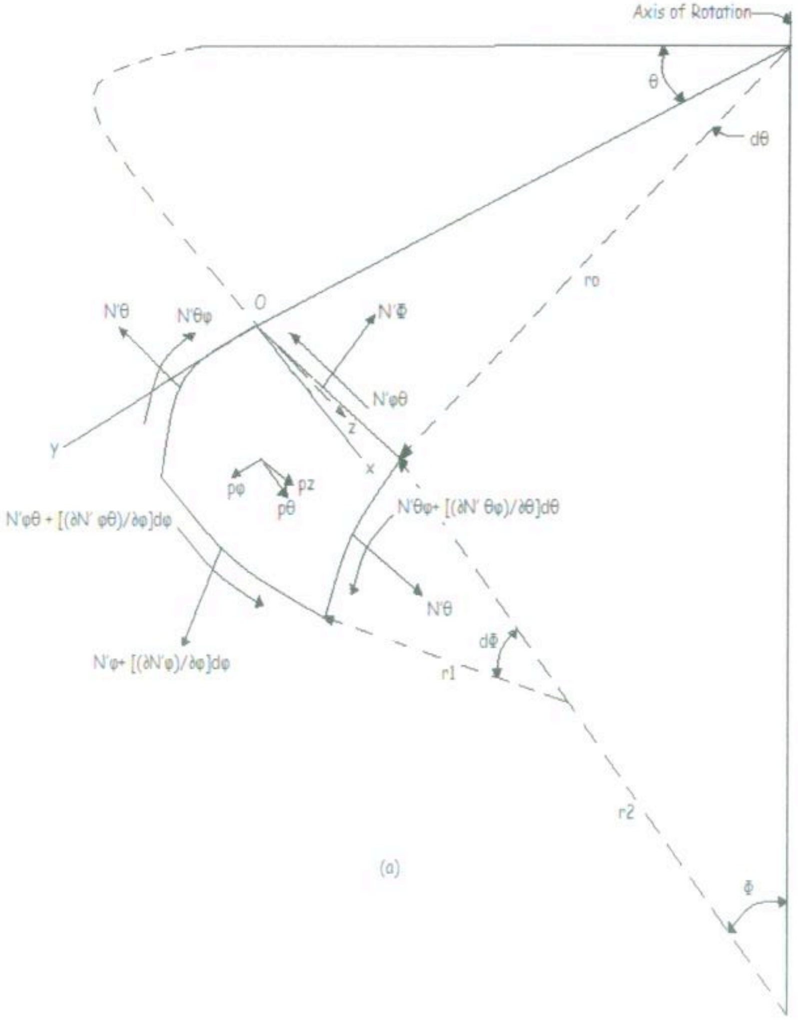

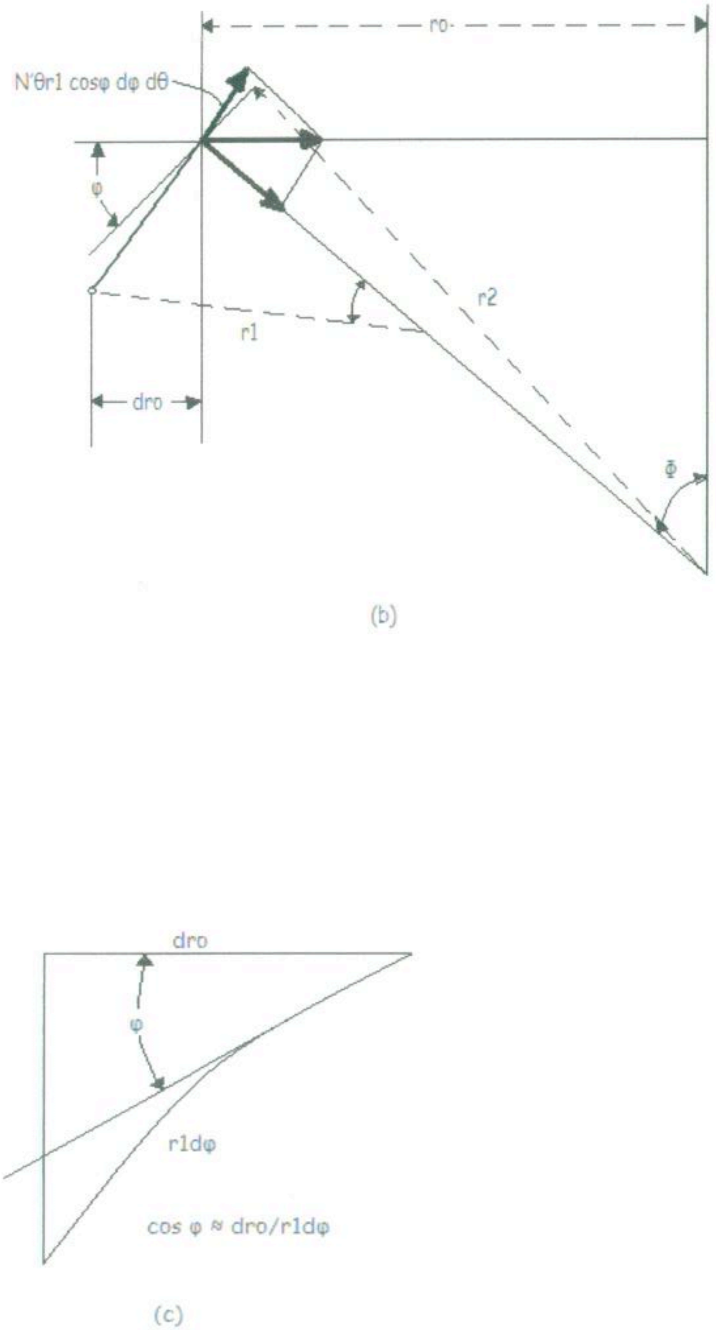

Figure 2-1—Definitions for domes from Billington (1).

Thus, the solution of the above equations for the force per length resultants N'_θ and $N'\varphi$ (referred to as stress resultants in Billington) is required for axisymmetrical domes under axisymmetrical loading. The first of the two equations can be written in another form which has a simpler solution. From Figure 2-2 a, observe:

$$\cos(\phi) \approx \frac{dr_o}{r_1 d\phi}$$

(For shallow curves), or

$$\frac{dr_o}{d\phi} = r_1 \cos(\phi)$$

Which can be substituted into the first of the two equations (2-2) to give:

$$\frac{d(N'_\phi r_o)}{d\phi} - N'_\theta r_1 \cos(\phi) + p_\phi r_o r_1 = 0$$

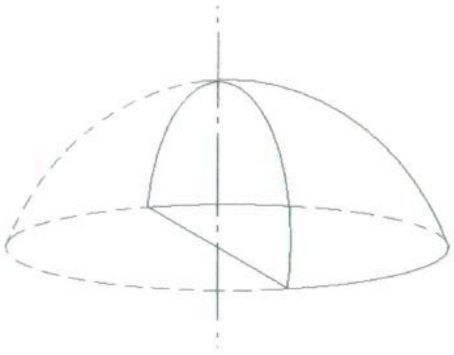

(a)

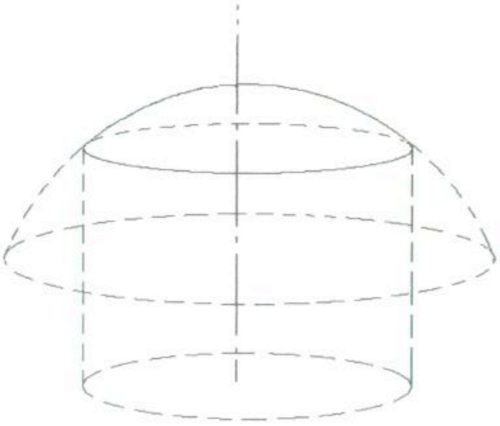

(b)

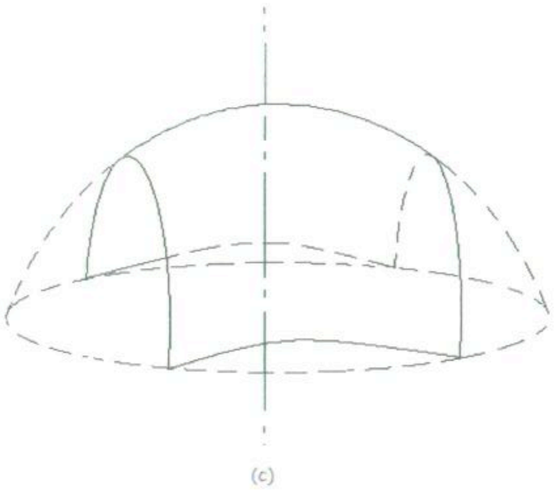

Figure 2-2—Dome Forms from Billington (1).

The effect of N'_θ in the meridian direction could have been directly obtained from Figure 2-2 b by noting that the meridian sides of the element form the angle $d\theta\cos(\varphi)$ with each other. Therefore, in the meridional direction there will be a component of the hoop stress resultant in the negative direction:

$$N'_\theta r_1 d\phi d\theta \cos(\phi)$$

The multipliers $d\varphi$ and $d\theta$ become constants throughout and therefore cancel. Thus, when they are dropped, the above reduces to:

$$N'_\theta r_1 \cos(\phi)$$

The second equation of (2-2) can be solved for N'_θ:

$$N'_\theta = -\frac{r_o}{\sin(\phi)}(\frac{N'_\phi}{r_1} + p_z)$$

because

$$r_2 = \frac{r_o}{\sin(\phi)}$$

Now, N'_θ is introduced into the first of (2-2) and each term is multiplied by sin(φ) to obtain:

$$\sin(\phi)\frac{d(N'_\phi r_o)}{d\phi} + \sin(\phi)\frac{r_o}{\sin(\phi)}(\frac{N'_\phi}{r_1} + p_z)r_1\cos(\phi) + \sin(\phi)p_\phi r_o r_1 = 0$$

The above is then multiplied by 2π and integrated with respect to φ, yielding:

$$\int_0^\phi \sin(\phi)\frac{d(N'_\phi r_o)}{d\phi}d\phi + \int_0^\phi N'_\phi r_o\cos(\phi)d\phi = -\frac{1}{2\pi}\int_0^\phi (p_\phi\sin(\phi) + p_z\cos(\phi))2\pi r_o r_1 d\phi$$

Using integration by parts:

$$\int u dv = uv - \int v du$$

where u = sinφ, du = cosφdφ, dv = $[d(N'\varphi r_o)/d\varphi]d\varphi$, and v = $N'\varphi r_o$. Thus, the left side of the equation becomes:

$$\sin(\phi)N'_\phi r_o - \int_0^\phi N'_\phi r_o\cos(\phi)d\phi + \int_0^\phi N'_\phi r_o\cos(\phi)d\phi$$

And thus, the integral reduces to:

$$N'_\phi = -\frac{1}{2\pi r_o\sin(\phi)}\int_0^\phi (p_\phi\sin(\phi) + p_z\cos(\phi))(2\pi r_o)r_1 d\phi$$

where $(p_\varphi\sin(\varphi) + p_z\cos(\varphi))$ gives the vertical component of the load. $2\pi r_o$ sums this vertical load over a complete parallel circle, and int(0, φ)$r_1 d\varphi$ integrates the vertical load along a meridian. Thus, the above equation represents the total vertical load (R in Fig. 2-3) above the paralled circle defined by φ. $N'\varphi 2\pi r_o \sin\varphi$ is the total vertical component of $N'\varphi$ at the parallel circle φ.

Thus, N´φ can be written as:

$$N'_{\phi} = -\frac{R}{2\pi r_o \sin(\phi)} \qquad \boxed{(2\text{-}3a)}$$

and,

$$N'_{\theta} = \frac{R}{2\pi r_1 \sin^2(\phi)} - p_z \frac{r_o}{\sin(\phi)} \qquad \boxed{(2\text{-}3b)}$$

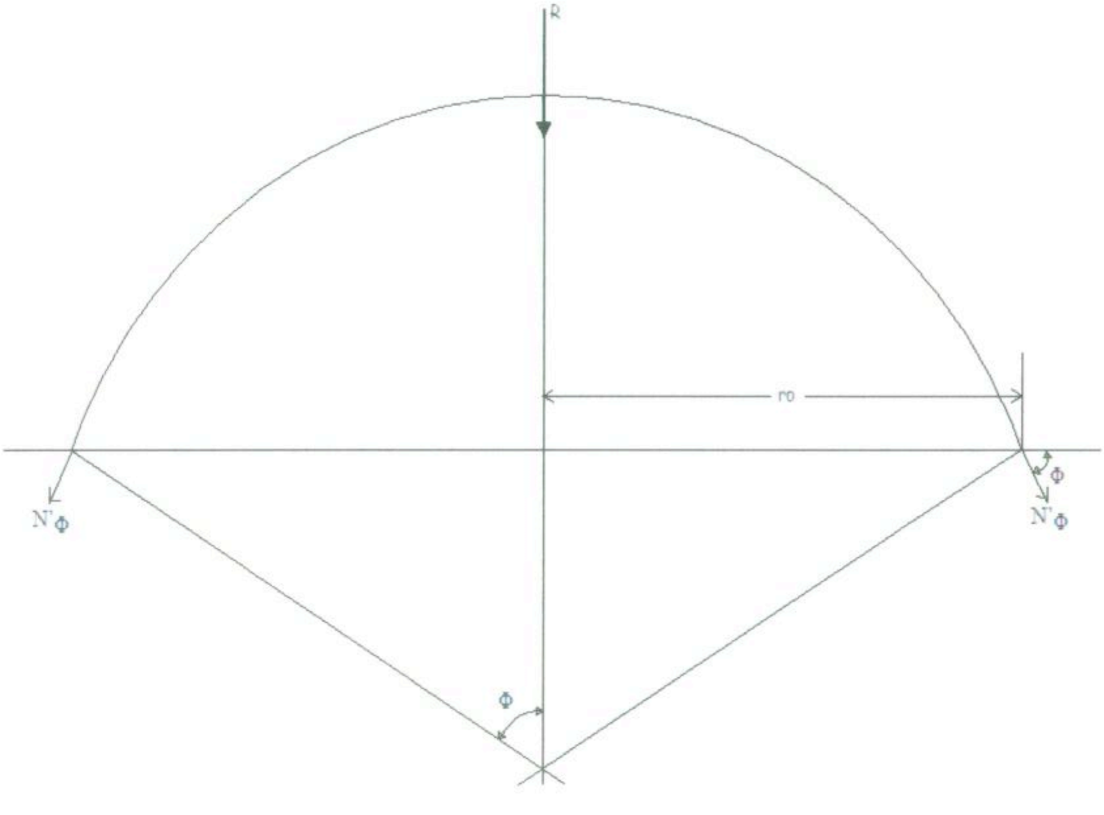

Figure 2-3—Dome Equilibrium from Billington (1).

Specifically of interest for verification of the validity of Finite Element Analysis of stress is a uniform load over the dome surface of a spherical dome. Billington gives the case of the spherical dome of uniform thickness under dead load, $r_1 = r_2 = a$, $p_{\varphi} =$

qsinφ, and p_Z = qcosφ, where q is the dead weight of the shell in terms of force/(length)^2, and

$$R = 2\pi a^2 q \int_0^{\varphi} \sin(\phi) d\phi$$
$$= 2\pi a^2 q (1 - \cos(\phi))$$

and (2-3) become

$$N'_\phi = -aq \frac{1}{1 + \cos(\phi)} \qquad \boxed{(2\text{-}4)}$$

$$N'_\theta = aq\left(\frac{1}{1 + \cos(\phi)} - \cos(\phi)\right) \qquad \boxed{(2\text{-}5)}$$

Equations (2-4) and (2-5) are the two membrane resultants. If evaluated over a hemisphere, the meridional values, (2-4), are compressive and increase from the crown to the edge. The hoop values, (2-5), decrease from a maximum compression at the crown to zero where cos φ = (1/(1 + cos φ), or about φ =51°50'; then they become tension and increase to a maximum at the edge.

Equations (2-4) and (2-5) are used throughout the course of the finite element analysis for results comparisons and accuracy verification. The Finite Element model is regarded as valid only after basic stress comparisons are made between the model and theory.

The current design practice utilizes theory. However, there is an increase in the use of Finite Element Analysis in design for more complicated models--for example, domes with skylights, cutouts or various complicated loadings. The agreement between shell theory and FEA will increase confidence in the Finite Element model and results.

Chapter 3

AN INTRODUCTION TO FINITE ELEMENT ANALYSIS AND NE/NASTRAN

Daryl L. Logan describes the Finite Element Method as "a numerical method for solving problems of engineering and mathematical physics." Some typical problems that are solvable by use of Finite Element methods include structural analysis, heat transfer, fluid flow, mass transport, and electromagnetic potential (20).

It is very difficult to obtain closed-form solutions for complicated geometries, loadings, and material properties. Analytical solutions generally require the solution of ordinary or partial differential equations, which are not usually obtainable for complex problems. Hence, numerical methods are relied upon, such as the Finite Element method, for acceptable solutions. Numerical methods yield approximate values of the unknowns at discrete points. The process of modeling a body by dividing it into an equivalent system of smaller units (finite elements) interconnected at points common to two or more elements (nodal points or nodes) and/or boundary lines and/or surfaces is called discretization. In the finite element method, equations are formulated for each finite element and then combined to obtain the solution of the entire model (20).

For structural problems, the solution generally refers to determining the displacements and stresses at each node and within each element that makes up the structure when it is subjected to applied loads. When analyzing nonstructural problems, the unknown nodal values may be temperatures or fluid pressures, etc. (20).

The general steps of the finite element method for the structural stress-analysis problem are described in Logan's text as follows.

- Step 1: *Discretize and Select the Element Types.* Dividing the body into an equivalent system of finite elements with associated nodes and choosing the most appropriate element type to model most closely the actual physical behavior. The elements must be small enough to give usable results and large enough to reduce computational effort. Thus, some engineering judgment must be used. Small elements are generally desirable where the results are changing rapidly, such as where changes in geometry occur; large elements can be used where results are relatively constant.

  Element choice depends on the physical makeup of the body under actual loading conditions. Judgment must be used in choosing one-, two-, or three-dimensional idealizations. Elements that are commonly employed are shown in Figure 3-1.

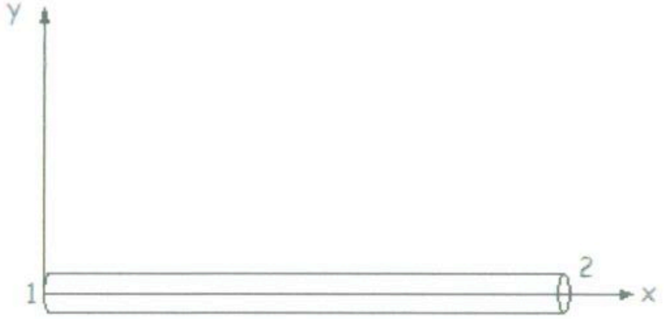

(a) Simple line element typically used to represent a bar or beam element

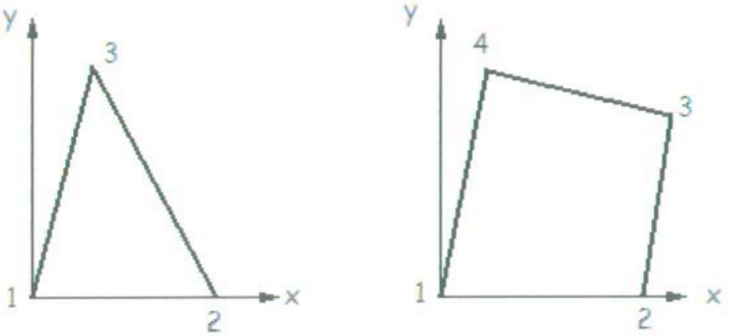

(b) Simple two-dmensional elements typically used to represent plane stress/strain

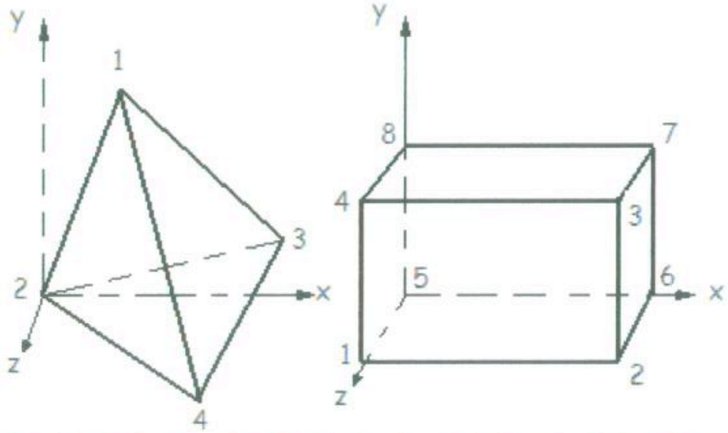

(c) Simple 3-dim. elements used to represent 3-dim. stress

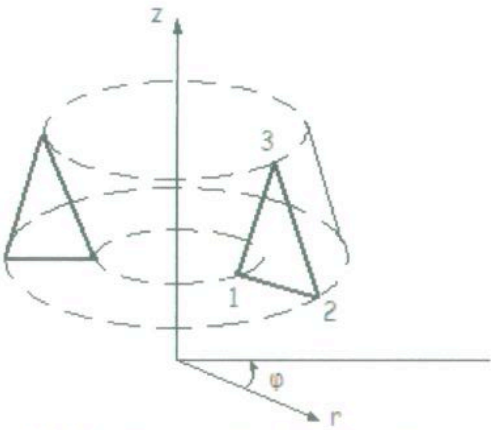

(d) Simple axisymmetric element

Figure 3-1—Various Types of Finite Elements from Logan (20).

The primary line elements (Figure 3-1a) consist of bar (or truss) and beam elements. They have a cross-sectional area but are usually line elements. The simplest line element, called a linear link or spar element, has two nodes, one at each end. Higher order elements having three nodes or more, called quadratic, cubic, etc., also exist.

The basic two-dimensional, plane, elements (Figure 3-1b) are loaded by forces in their own plane. They are triangular or quadrilateral elements. The simplest two-dimensional plate elements have corner nodes with straight sides or boundaries, called simplex elements. There are also serendipity higher-order, quadratic, elements with midside nodes and curved sides. These elements can have variable or constant thicknesses.

The most common three-dimensional elements (Figure 3-1c) are tetrahedral and hexahedral, brick, elements. They are used for three-dimensional stress analysis. The basic three-dimensional elements have corner nodes only and straight sides. Higher-order elements, Lagrange elements, have midedge nodes (and possible midface nodes) and have curved surfaces for their faces.

The axisymmetric element (Figure 3-1d) is developed by rotating a triangle or quadrilateral through 360° about a fixed axis located in the plane of the element. This element can be used when the geometry and loading are axisymmetric.

- Step 2: *Select a Displacement Function.* The displacement function is defined within the element using the nodal values of the element. Frequently used functions are linear, quadratic, and cubic polynomials because they are simple to work with in finite element formulation. Trigonometric series can also be used. The displacement function of a two-dimensional element is a function of the coordinates in its plane. The functions are expressed in terms of the nodal unknowns. The same general displacement function can be used repeatedly for each element.

- Step 3: *Define the Strain/Displacement and Stress/Strain Relationships.* Strain/displacement and stress/strain relationships are necessary for deriving the equations for each finite element. For example, in the case of one-dimensional deformation, say, in the x direction, strain ε_X is related to the displacement u by $\varepsilon_X = du/dx$ for small strains. Stresses must be related to strains through the stress/strain relation called Hooke's Law. Being able to define the material's behavior accurately is most important in obtaining acceptable results. Hooke's law, $\sigma_X = E\varepsilon_X$, is used in stress analysis, where σ_X = stress in the x direction and E = modulus of elasticity.

- Step 4: *Derive the Element Stiffness Matrix and Equations.*
  1. Direct Equilibrium Method: The stiffness and element equations relating nodal forces to nodal displacements are obtained using force equilibrium conditions for a basic element, along with force/deformation relationships. This method is most easily adaptable to line or one-dimensional elements.

  2. Work or Energy Methods: This method is easier for two- and three-dimensional elements. The principle of virtual work (using virtual

displacements), the principle of minimum potential energy, and Castigliano's theorem are methods frequently used.

3. Methods of Weighted Residuals: These methods are useful for developing the element equations; particularly popular is Galerkin's method.

Any of the above methods will produce the equations to describe the behavior of an element. These equations written in compact matrix form are:

$$\{f\} = [k]\{d\}$$

where {f} is the vector of elemental nodal forces, [k] is the element stiffness matrix, and {d} is the vector of unknown element nodal degrees of freedom or generalized displacements, n. These may include actual displacements, slopes, or even curvatures.

- Step 5: *Assemble the Element Equations to Obtain the Global or Total Equations and Introduce Boundary Conditions.* The individual element equations generated in step 4 can now be added together using a method of superposition (called the direct stiffness method)—whose basis is nodal force equilibrium—to obtain the global equations for the whole structure. There must be consistency in the deformation of the structure, that is, elements sharing a node will have the same displacements at that node.

  The final assembled or global equation written in matrix form is

$$\{F\} = [K]\{d\}$$

where {F} is the vector of global nodal forces, [K] is the structure global or total stiffness matrix, and {d} is the vector of known and unknown structure nodal degrees of freedom or generalized displacements. The global stiffness matrix [K] is a singular matrix. Thus, certain boundary conditions must be invoked (from constraints or supports) so that the structure remains in place. The applied loads have been accounted for in the global force matrix {F}.

- Step 6: *Solve for the Unknown Degrees of Freedom (or Generalized Displacements).* The equation {F} = [K]{d} is a set of simultaneous algebraic equations that can be written in expanded matrix form as

$$\begin{Bmatrix} F1 \\ F2 \\ . \\ . \\ . \\ Fn \end{Bmatrix} = \begin{bmatrix} K11 \;\; K12 \ldots\ldots K1n \\ K21 \;\; K22 \ldots\ldots K2n \\ . \\ . \\ . \\ Kn1 \;\; Kn2 \ldots\ldots Knn \end{bmatrix} \begin{Bmatrix} d1 \\ d2 \\ . \\ . \\ . \\ dn \end{Bmatrix}$$

  where n is the total number of unknown nodal degrees of freedom.

  These equations can be solved for the d's by using an elimination method such as Gauss's Method. The d's are called the primary unknowns, because they are the first quantities to be determined in using the finite element method.

- Step 7: *Solve for the Element Strains and Stresses.* Important secondary quantities of strain and stress (or moment and shear force) can be obtained because they can be directly expressed in terms of the displacements determined in step 6. The equations given in step 3 can be used.

- Step 8: *Interpret the Results.* The final goal is to interpret and analyze the results for use in the design/ analysis process. The determination of locations in the structure where large deformations and stresses occur is important in making design/analysis decisions.

These steps, as described in Logan's text, are the basis for the finite element modeling software available. The software used in this dome analysis was NE/Nastran version 8.3, from Noran Engineering.

As described in the NE/Nastran User Guide, NE/Nastran is a finite element modeling and post-processing software. NE/Nastran provides the capability to develop sophisticated analyses of stress, temperature, and dynamic performance directly on the desktop. NE/Nastran can be used to create geometry, or CAD geometry can be imported. NE/Nastran provides powerful tools for meshing geometry, as well as applying loads and boundary conditions. Once results are obtained, a wide variety of tools are available for visualizing and reporting (21).

Geometry

Geometry can be created directly in NE/Nastran using wireframe and solid modeling tools. NE/Nastran includes solid modeling directly in the program with two similar, popular geometry engines (Parasolid and ACIS). Solid models can be built in either engine, and then a model can be exported (21).

Finite Element Modeling

Regardless of the origin of the geometry, NE/Nastran can be used to create a complete finite element model. Meshes can be created by many methods ranging from manual creation, to mapped meshing between keypoints, to fully automatic meshing of curves, surfaces and solids. NE/Nastran can even work with existing analysis models.

Appropriate materials and section properties can be created or assigned from libraries. Many types of constraint and loading conditions can be applied to represent the design environment. Loads/constraints can be applied directly on finite element entities (nodes and elements), or can be applied to the geometry. NE/Nastran will automatically convert geometric conditions to nodal/elemental values upon translation to the solver program (21).

Checking The Model

NE/Nastran for Windows contains a multi-level undo and redo capability. It also provides extensive tools for checking the model before it is analyzed. NE/Nastran also provides a comprehensive set of tools to evaluate the finite element model and identify errors that are often not obvious. For example, it can check for coincident geometry, find improper connections, estimate mass and inertia, evaluate constraint conditions, and sum loading conditions. Each of these methods can be used to identify and eliminate potential errors (21).

Analyzing The Model

When the model is complete, the NE/Nastran solver is used. The NE/Nastran for Windows solver is a general finite element analysis program for structural and thermal analysis that is integrated with NE/Nastran for Windows (21).

Post-processing

After the analysis, NE/Nastran provides both powerful visualization tools, and numerical tools to search, report, and perform further calculations using these results.

Deformation

plots, contour plots, animations, and XY plots are just some of the post-processing tools available (21).

Documenting Results

Documentation is also a very important factor with any analysis. NE/Nastran provides direct, high quality printing and plotting of both graphics and text. Frequently, however, graphics or text must be incorporated into a larger report or presentation. NE/Nastran can export both graphics and text to non-engineering programs with a simple Windows Cut command. Pictures can be easily exported to Microsoft Word, Microsoft PowerPoint, and Adobe Framemaker. Spreadsheets, databases, word processors, desktop publishing software, and paint and illustration programs can be exported (21).

NE/Nastran for Windows

NE/Nastran for Windows currently supports:

- statics analysis solves for linear, static stress, and deflection results when thermo-mechanical loads are present.

- dynamic (normal modes) solves for natural frequencies and mode shapes of either restrained or free-free structures.
- advanced dynamics capabilities such as transient response, frequency response, response spectrum analysis, random response.
- nonlinear static and transient analysis.
- both steady-state and transient heat transfer analysis solves for temperatures due to convection, conduction, heat generation and radiation.
- linear buckling analysis.
- design optimization helps find more efficient design solutions (21).

Chapter 4

A COMPARISON BETWEEN SHELL THEORY AND FEA FOR A HEMISPHERICAL DOME

A comparison of a hemispherical dome was made between the NASTRAN Finite Element Analysis results and the shell theory equations using an example found on page 207 of "Stresses in Plates and Shells," by A.C. Ugural. A simply supported covered market dome of radius, *a*, and thickness, *t*, carrying only its own weight, *p*, per unit area was considered. The hemispherical dome was to be constructed of 70-mm-thick concrete of unit weight 23 KN/m^3 and span 2*a* = 56m. The modulus of elasticity was given as 20GPa.

The membrane stresses were calculated using the following equations from Ugural which are equivalent to those derived previously but used in a slightly different form:

Meridional Stress: $\sigma_\varphi = - ap/(t*(1+\cos\varphi))$ $\boxed{(4\text{–}1)}$

Hoop Stress: $\sigma_\theta = - (ap/t)*[\cos\varphi - 1/(1 + \cos\varphi)]$ $\boxed{(4\text{-}2)}$

In the hemispherical case, $\varphi = 90°$. From the given information, a = 28m, t = .03m, and p = (23 KN/m^3 * t). Therefore, Equation (4-1) yields -644 KPa at the bottom edge of the dome, which is the maximum compressive stress. Equation (4-2) yields +644 KPa also located at the bottom edge of the dome, which is the maximum tensile stress.

In NASTRAN, the geometry for a 28m radius hemispherical dome was generated using the parasolid modeling engine within NE/Nastran. Material properties were entered as t = .03m, E = 20 x 10^6 KPa, $\nu = 0.15$, and mass density = (23 KN/m^3) / (9.81 m/s^2) = 0.002345. To include the self-weight of the dome and the gravitational acceleration, 9.81 m/s^2,was entered.

A four-node quadrilateral plate element was used in meshing the dome. A rough mesh was applied for initial comparison and then refined until the stresses converged to the values found using the Ugural stress equations. The bottom edge of the dome was constrained in the z-direction (vertically), and one node on the edge was constrained in the x, y, and z directions to provide stability during analysis.

The first iteration of analysis was with the roughly-meshed model shown in Figure 4-1. The maximum hoop stress was found to be +755.5 KPa (figure 2), and the maximum meridional stress was -712 KPa (Figure 3).

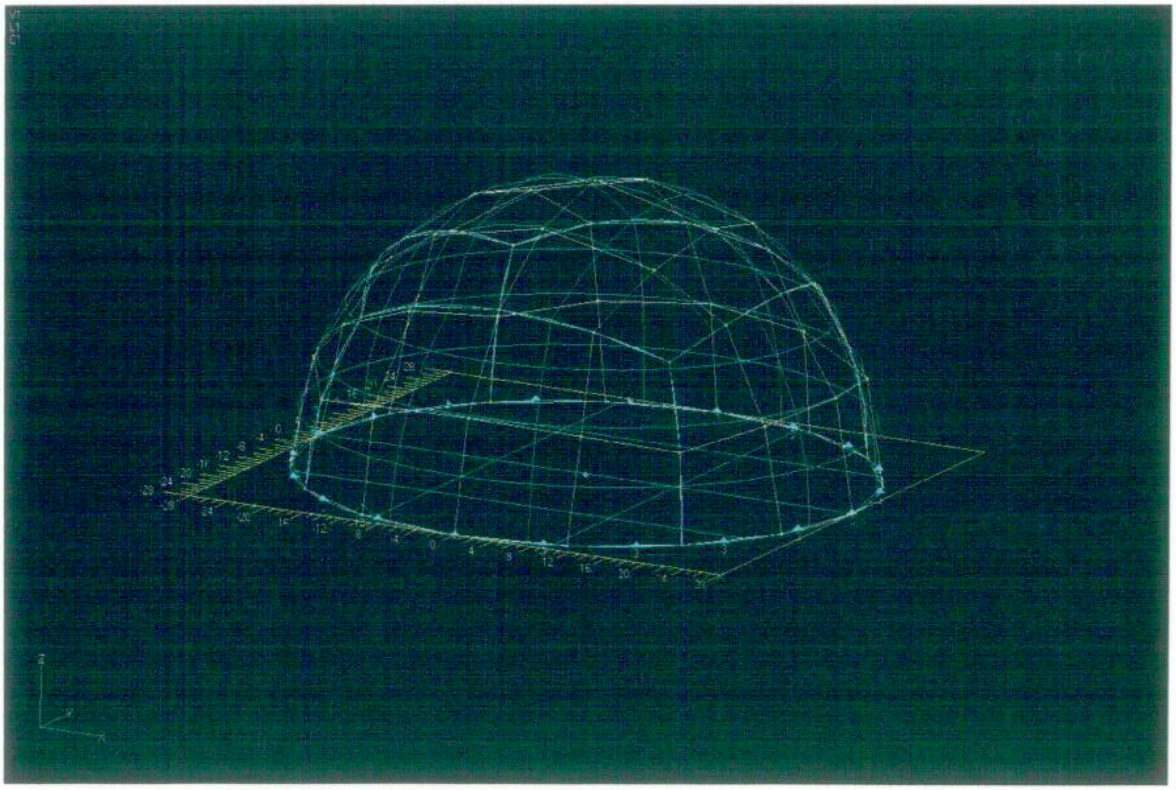

Figure 4-1 – Rough Mesh of 56m Span Hemispherical Dome in NASTRAN.

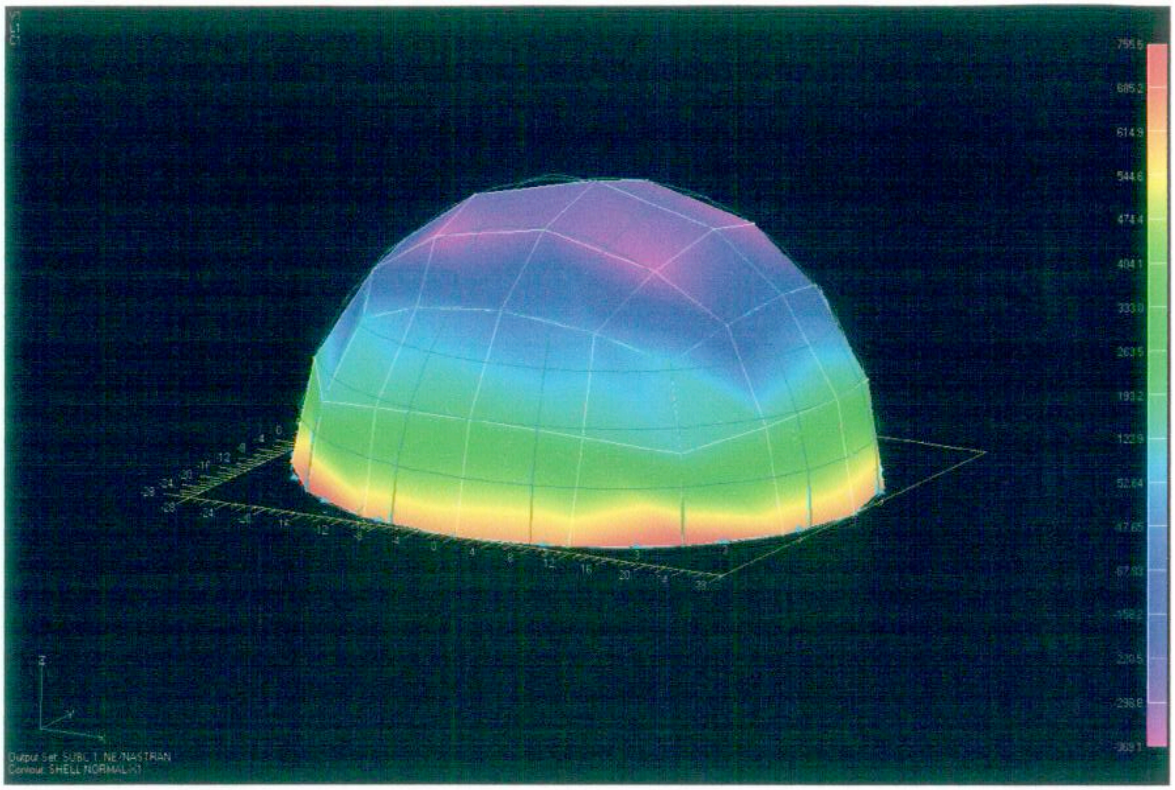

Figure 4-2 – Distribution of Hoop Stresses for Roughly Meshed 56m Span Dome.

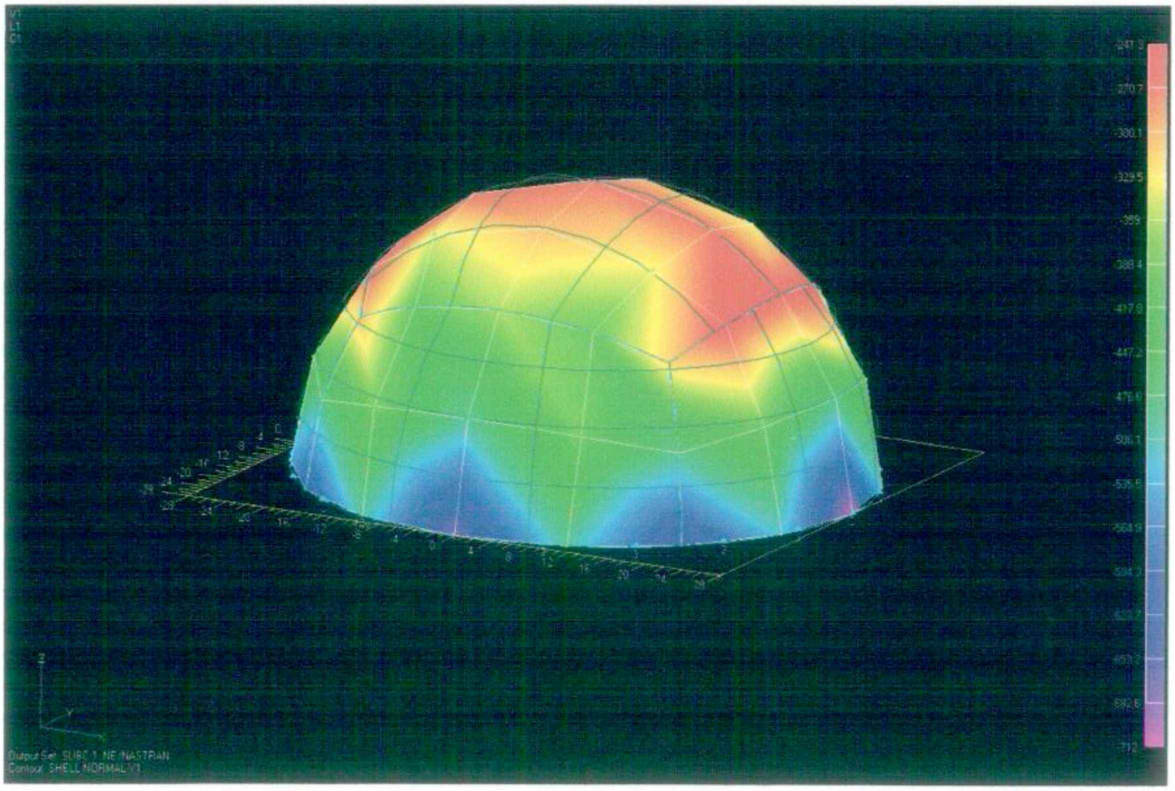

Figure 4-3 – Distribution of Meridional Stresses for Roughly Meshed 56m Span Dome.

After a few more iterations, a fairly fine mesh was used to analyze the stresses as shown in Figure 4-4. The maximum hoop stress was found to be +651.8 KPa (Figure 4-5), and the maximum meridional stress was -631.0 KPa (Figure 4-6).

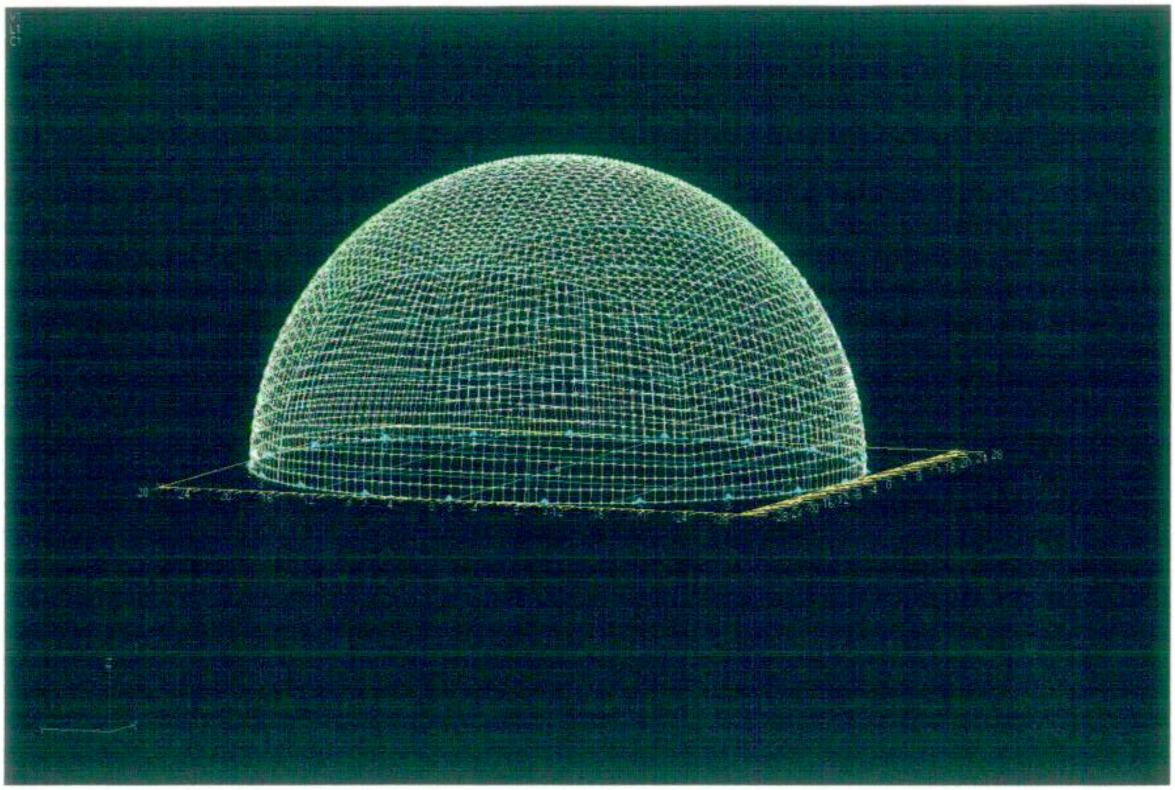

Figure 4-4 - Medium Mesh of 56m Span Hemispherical Dome in NASTRAN.

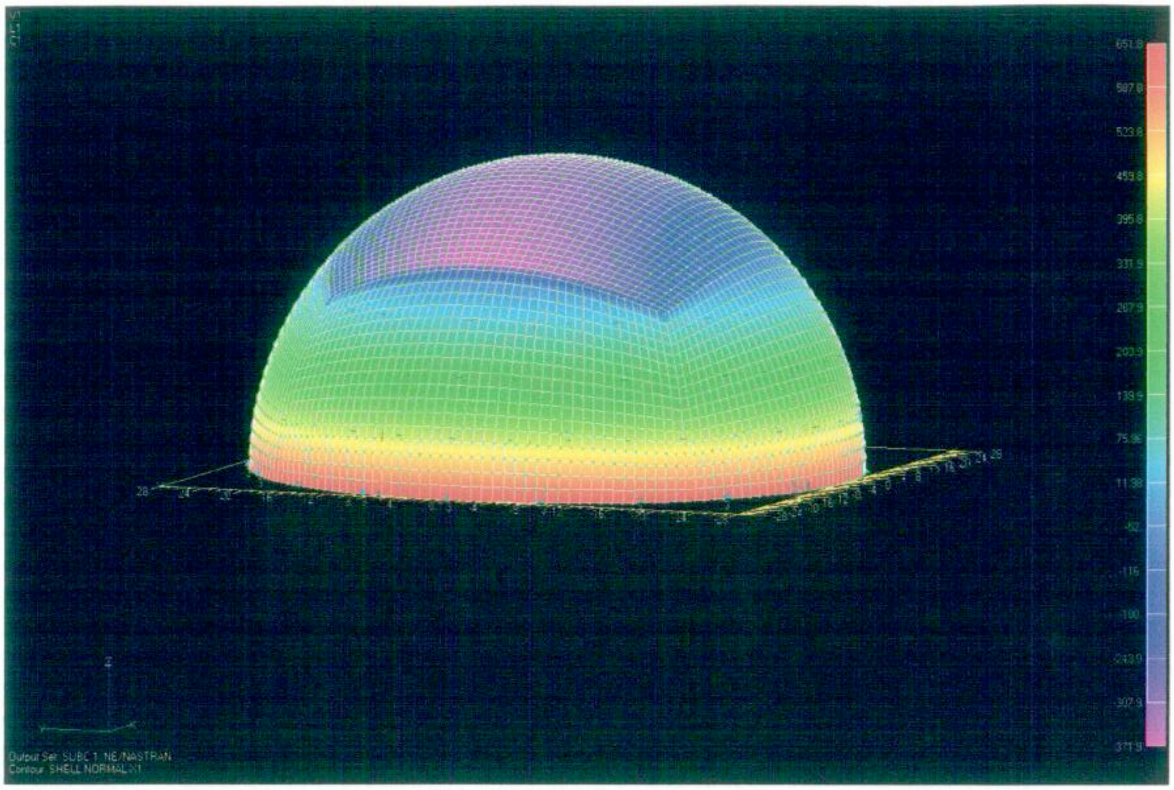

Figure 4-5 – Distribution of Hoop Stresses for Medium Mesh of 56m Span Dome.

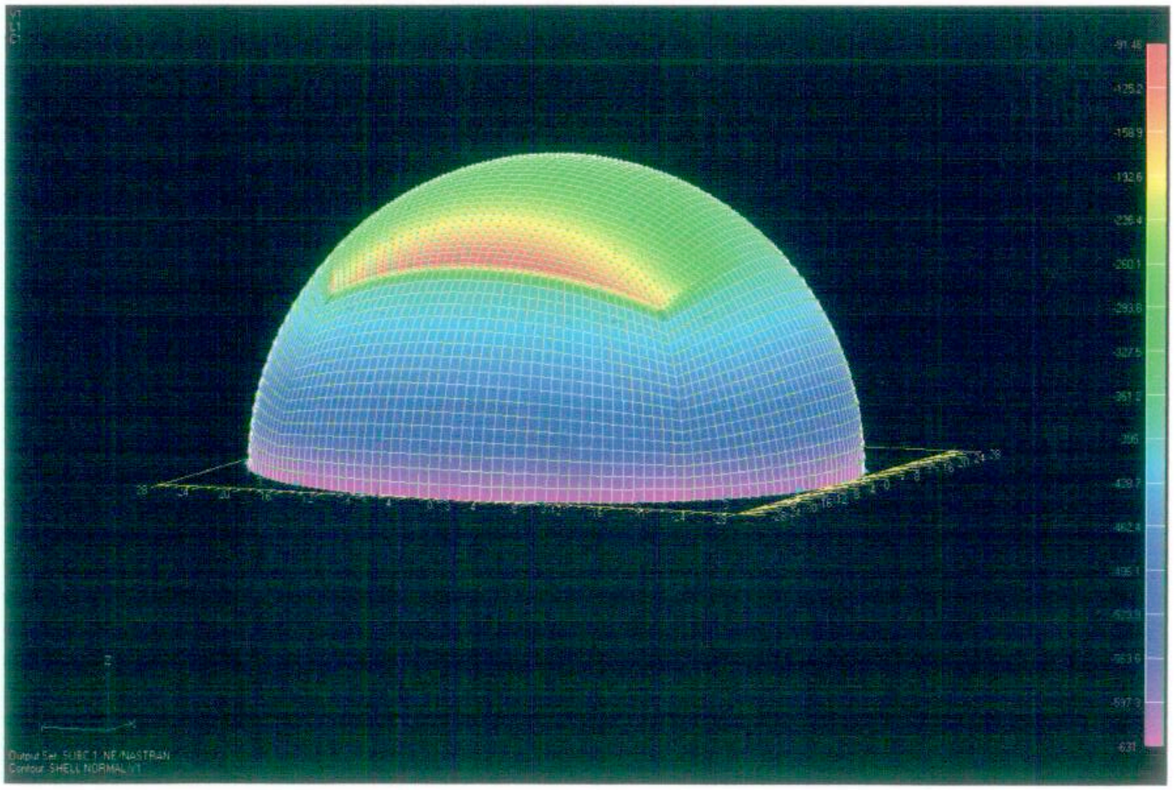

Figure 4-6 – Distribution of Meridional Stresses for Medium Mesh of 56m Span Dome.

A very fine mesh was used in the final analysis of the stresses as shown in Figure 4-7. The maximum hoop stress was found to be +647.5 KPa (Figure 4-8), and the maximum meridional stress was -638.1 KPa (Figure 4-9). With each refinement at this point, the stress values were converging. Comparing the calculations using shell theory with the NASTRAN results, the stresses were found to be approximately equal; see Table 4-1.

Table 4-1 – Shell Theory vs. FEA Stress Results for 56m Span Hemispherical Dome.

Method	Maximum Hoop Stress, KPa	Maximum Meridional Stress, KPa
Shell Theory	+644	-644
NASTRAN, FEA	+647.5	-638.1

Thus, the finite element model is valid.

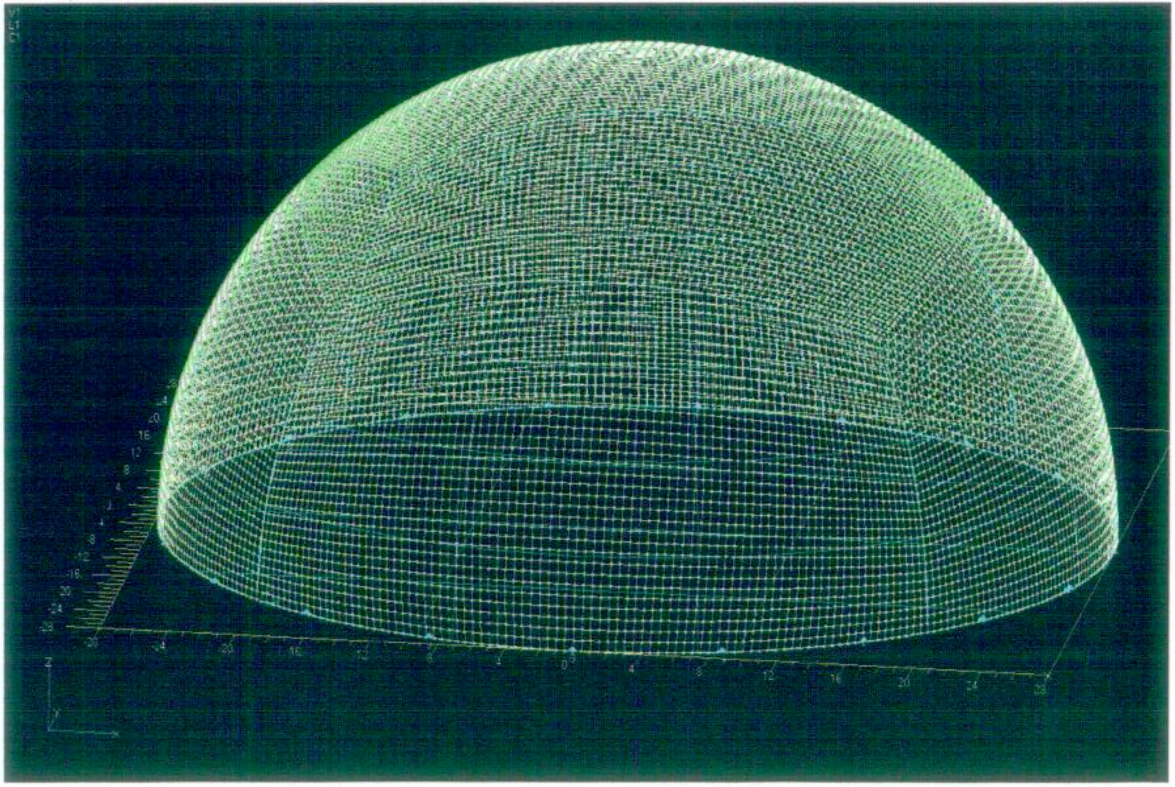

Figure 4-7 – Fine Mesh of 56m Span Hemispherical Dome in NASTRAN.

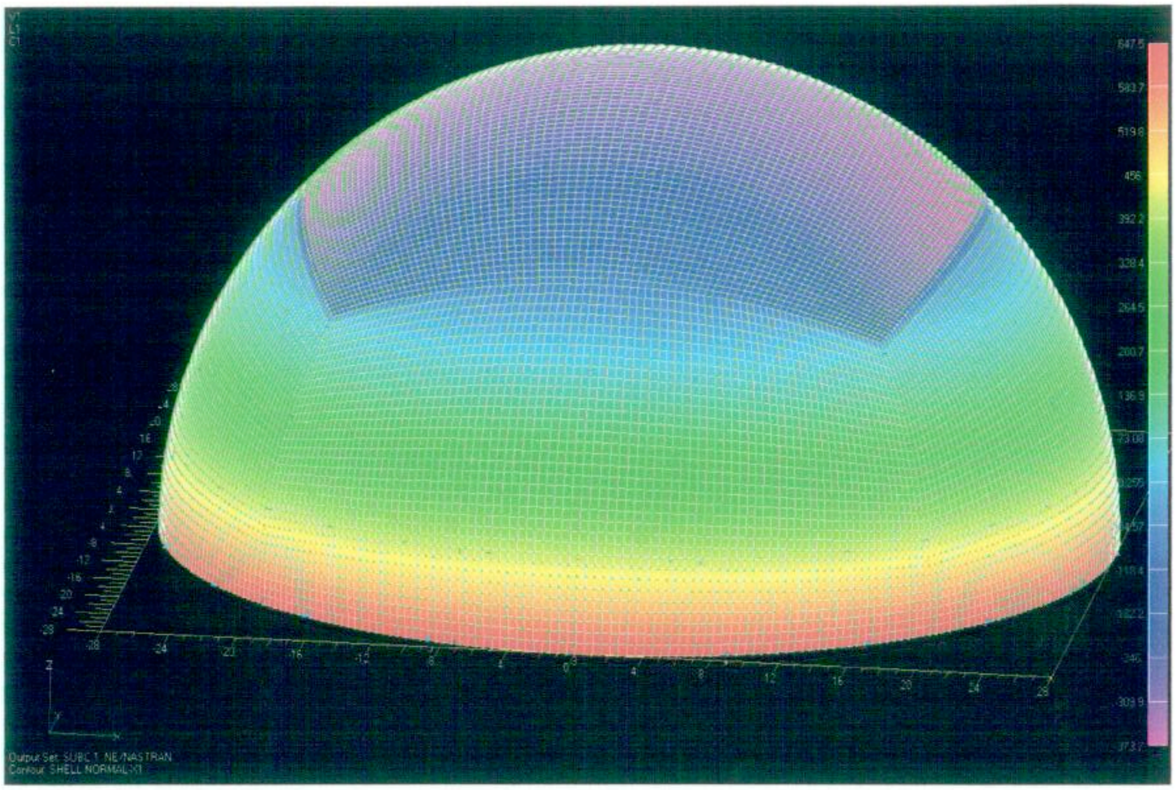

Figure 4-8 – Distribution of Hoop Stresses for Fine Mesh of 56m Span Dome.

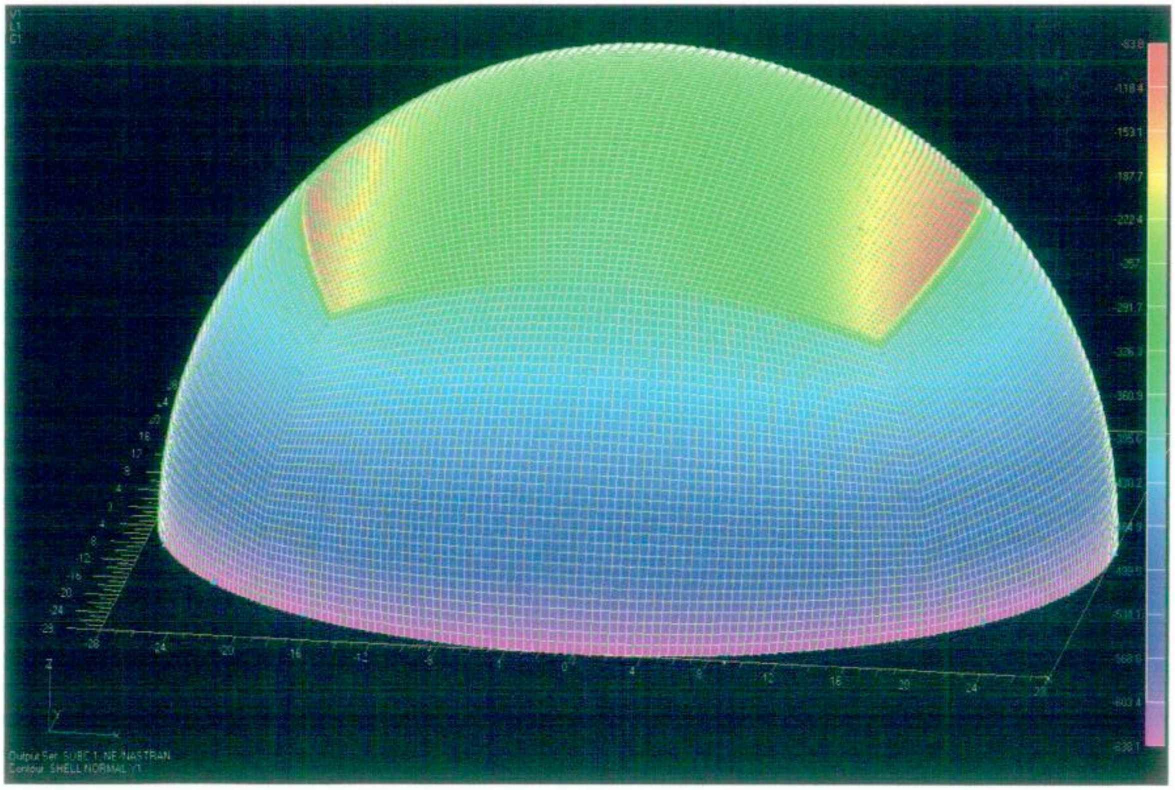

Figure 4-9 – Distribution of Meridional Stresses for Fine Mesh of 56m Span Dome.

A vertical row of 77 elements beginning at the bottom edge of the dome and ranging to the top of the dome were analyzed in greater detail. Table 4-2 lists the element number, the vertical distance to the center of each element, and the forces and moments that were calculated by NASTRAN at the center of each element.

Table 4-2 – Elements, Forces, and Moments from Bottom Edge to Apex of 56m Span Dome.

Element	Height, m	Fx, KN	Fy, KN	Fxy, KN	Mx, KN-m	My, KN-m	Mxy, KN-m
45	0.32	44.117	-44.555	0.177	-2.57E-04	4.39E-04	-4.24E-05
133	0.97	42.022	-43.559	0.175	-2.28E-04	1.01E-03	1.52E-05
221	1.62	40.004	-42.609	0.176	-2.28E-05	1.12E-03	7.98E-05
309	2.26	38.059	-41.702	0.175	6.28E-05	-2.52E-05	6.20E-05
397	2.90	36.157	-40.834	0.173	1.64E-04	-1.97E-04	-2.06E-06
485	3.55	34.289	-40.003	0.172	2.78E-04	7.13E-04	-4.99E-05
573	4.19	32.465	-39.206	0.171	7.84E-05	-6.15E-05	-1.46E-05
661	4.83	30.674	-38.443	0.171	1.04E-04	1.12E-04	8.91E-06
749	5.46	28.918	-37.714	0.168	2.36E-04	6.68E-04	-1.19E-05
837	6.09	27.204	-37.015	0.166	2.24E-04	3.11E-04	1.66E-05
925	6.72	25.524	-36.344	0.164	2.30E-04	2.03E-04	-8.22E-06
1013	7.35	23.874	-35.701	0.162	2.62E-04	3.69E-04	-9.89E-06
1101	7.97	22.253	-35.084	0.161	2.89E-04	4.09E-04	-3.38E-06
1189	8.59	20.664	-34.492	0.159	3.83E-04	5.45E-04	2.22E-05
1277	9.20	19.107	-33.925	0.156	4.46E-04	3.87E-04	1.08E-05
1365	9.81	17.578	-33.381	0.153	5.46E-04	5.92E-04	1.93E-04
1453	10.41	16.081	-32.857	0.149	6.78E-04	1.09E-03	6.85E-06
1541	11.01	14.624	-32.354	0.147	6.32E-04	7.43E-04	-5.86E-06
1629	11.40	13.199	-31.870	0.144	5.65E-04	2.37E-04	-1.04E-05
1717	11.99	11.791	-31.405	0.140	6.26E-04	4.42E-04	-1.45E-05
1805	12.77	10.406	-30.958	0.137	6.95E-04	1.00E-03	-1.37E-05
1893	13.34	9.054	-30.530	0.135	7.12E-04	8.76E-04	3.91E-05
1981	13.90	7.735	-30.120	0.131	8.27E-04	7.34E-04	2.03E-05
2069	14.46	6.442	-29.726	0.127	8.99E-04	7.99E-04	-1.55E-05
2157	15.01	5.175	-29.347	0.123	9.38E-04	8.95E-04	1.95E-05
2245	15.55	3.935	-28.983	0.120	1.05E-03	1.10E-03	2.25E-05
2333	16.09	2.727	-28.631	0.116	9.97E-04	1.03E-03	-6.05E-05
2421	16.61	1.548	-28.292	0.112	9.17E-04	1.07E-03	-1.58E-05
2509	17.13	0.401	-27.968	0.108	9.22E-04	9.83E-04	1.21E-05
2597	17.64	-0.720	-27.658	0.104	9.41E-04	6.47E-04	2.39E-05
2685	18.14	-1.823	-27.361	0.101	1.07E-03	8.79E-04	2.48E-05
2773	18.62	-2.905	-27.076	0.097	1.16E-03	1.25E-03	-2.57E-07
2861	19.10	-3.959	-26.801	0.092	1.17E-03	1.04E-03	1.52E-05
2949	19.57	-4.986	-26.538	0.087	1.27E-03	1.35E-03	-6.38E-05
6029	19.96	-5.847	-26.317	0.261	1.32E-03	1.79E-03	-4.40E-05
6117	20.28	-6.529	-26.143	0.278	1.27E-03	1.53E-03	5.87E-05

6205	20.59	-7.192	-25.973	0.294	1.14E-03	1.21E-03	-1.98E-05
6293	20.90	-7.847	-25.807	0.306	1.04E-03	7.89E-04	-1.61E-05
6381	21.20	-8.494	-25.647	0.313	1.28E-03	1.22E-03	-2.19E-05
6469	21.50	-9.131	-25.492	0.319	1.45E-03	1.21E-03	-6.11E-05
6557	21.80	-9.760	-25.339	0.324	1.44E-03	1.21E-03	4.06E-05
6645	22.09	-10.379	-25.191	0.328	1.42E-03	1.48E-03	1.42E-04
6733	22.38	-10.985	-25.046	0.327	1.30E-03	1.39E-03	7.46E-05
6821	22.66	-11.578	-24.904	0.323	1.21E-03	1.35E-03	8.45E-06
6909	22.94	-12.156	-24.768	0.319	1.22E-03	1.23E-03	-8.61E-05
6997	23.21	-12.725	-24.636	0.312	1.17E-03	1.13E-03	-1.04E-04
7085	23.47	-13.283	-24.508	0.306	1.28E-03	1.69E-03	1.41E-05
7173	23.73	-13.822	-24.385	0.298	1.34E-03	1.51E-03	6.27E-06
7261	23.99	-14.348	-24.266	0.288	1.30E-03	8.82E-04	-8.37E-05
7349	24.23	-14.866	-24.151	0.279	1.43E-03	1.19E-03	-8.60E-05
7437	24.47	-15.373	-24.042	0.271	1.63E-03	1.74E-03	7.07E-05
7525	24.71	-15.864	-23.935	0.260	1.77E-03	1.98E-03	6.19E-05
7613	24.94	-16.332	-23.831	0.249	1.68E-03	1.68E-03	6.21E-06
7701	25.16	-16.783	-23.730	0.238	1.49E-03	1.19E-03	1.24E-05
7789	25.38	-17.224	-23.634	0.227	1.55E-03	1.30E-03	3.16E-05
7877	25.58	-17.651	-23.543	0.216	1.66E-03	1.62E-03	1.01E-04
7965	25.78	-18.062	-23.455	0.203	1.53E-03	1.56E-03	5.54E-05
8053	25.98	-18.457	-23.373	0.190	1.51E-03	1.51E-03	-7.45E-05
8141	26.16	-18.833	-23.294	0.178	1.77E-03	1.72E-03	-7.05E-05
8229	26.34	-19.192	-23.219	0.167	1.94E-03	1.81E-03	-3.77E-05
8317	26.51	-19.532	-23.146	0.157	1.70E-03	1.27E-03	1.11E-04
8405	26.67	-19.859	-23.077	0.146	1.58E-03	1.46E-03	8.31E-05
8493	26.82	-20.171	-23.013	0.133	1.58E-03	1.73E-03	-7.56E-05
8581	26.96	-20.462	-22.954	0.122	1.55E-03	1.51E-03	-3.94E-05
8669	27.10	-20.736	-22.900	0.112	1.60E-03	1.69E-03	-1.88E-05
8757	27.22	-20.990	-22.849	0.103	1.61E-03	1.83E-03	9.01E-05
8845	27.34	-21.222	-22.801	0.093	1.59E-03	1.60E-03	9.07E-05
8933	27.45	-21.437	-22.755	0.081	1.50E-03	1.34E-03	-1.48E-04
9021	27.55	-21.637	-22.715	0.072	1.48E-03	1.39E-03	-1.12E-04
9109	27.63	-21.821	-22.680	0.065	1.82E-03	1.90E-03	4.19E-05
9197	27.71	-21.982	-22.649	0.059	1.95E-03	2.07E-03	8.10E-05
9285	27.78	-22.118	-22.619	0.051	1.67E-03	1.61E-03	1.17E-04
9373	27.84	-22.234	-22.594	0.041	1.55E-03	1.45E-03	-3.59E-05
9461	27.89	-22.334	-22.572	0.032	1.58E-03	1.77E-03	-1.24E-04
9549	27.93	-22.412	-22.554	0.025	1.52E-03	1.55E-03	4.99E-06
9637	27.96	-22.472	-22.540	0.017	1.53E-03	1.46E-03	3.22E-05
9725	27.98	-22.515	-22.531	0.009	1.52E-03	1.69E-03	-6.79E-05

Plots of height vs. forces in the x and y direction are shown in Figures 4-10 and 4-11 below. Fx corresponds to the hoop forces and Fy corresponds to the meridional forces. Fxy = 0.

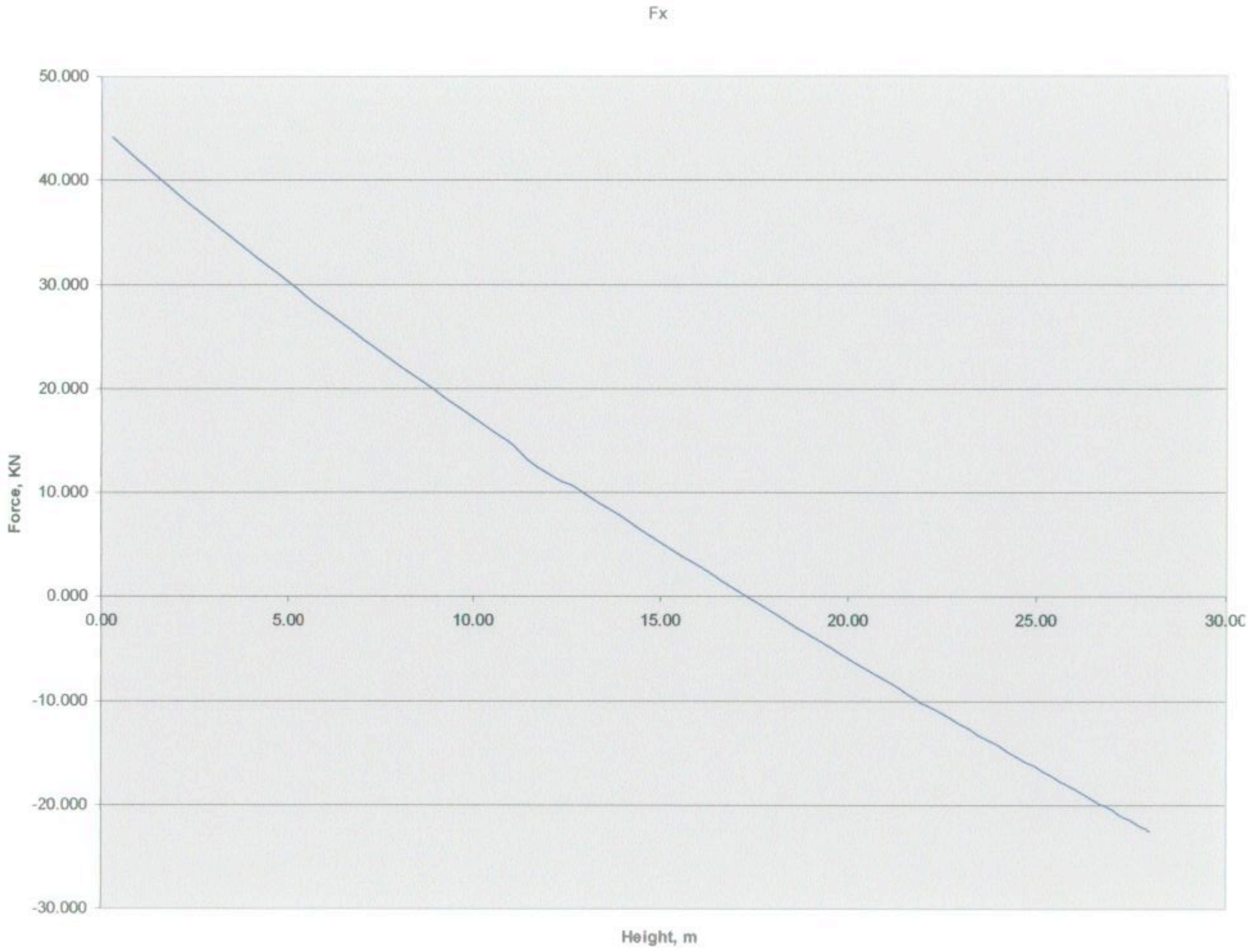

Figure 4-10 – Height vs. Fx for 56m Span Hemispherical Dome.

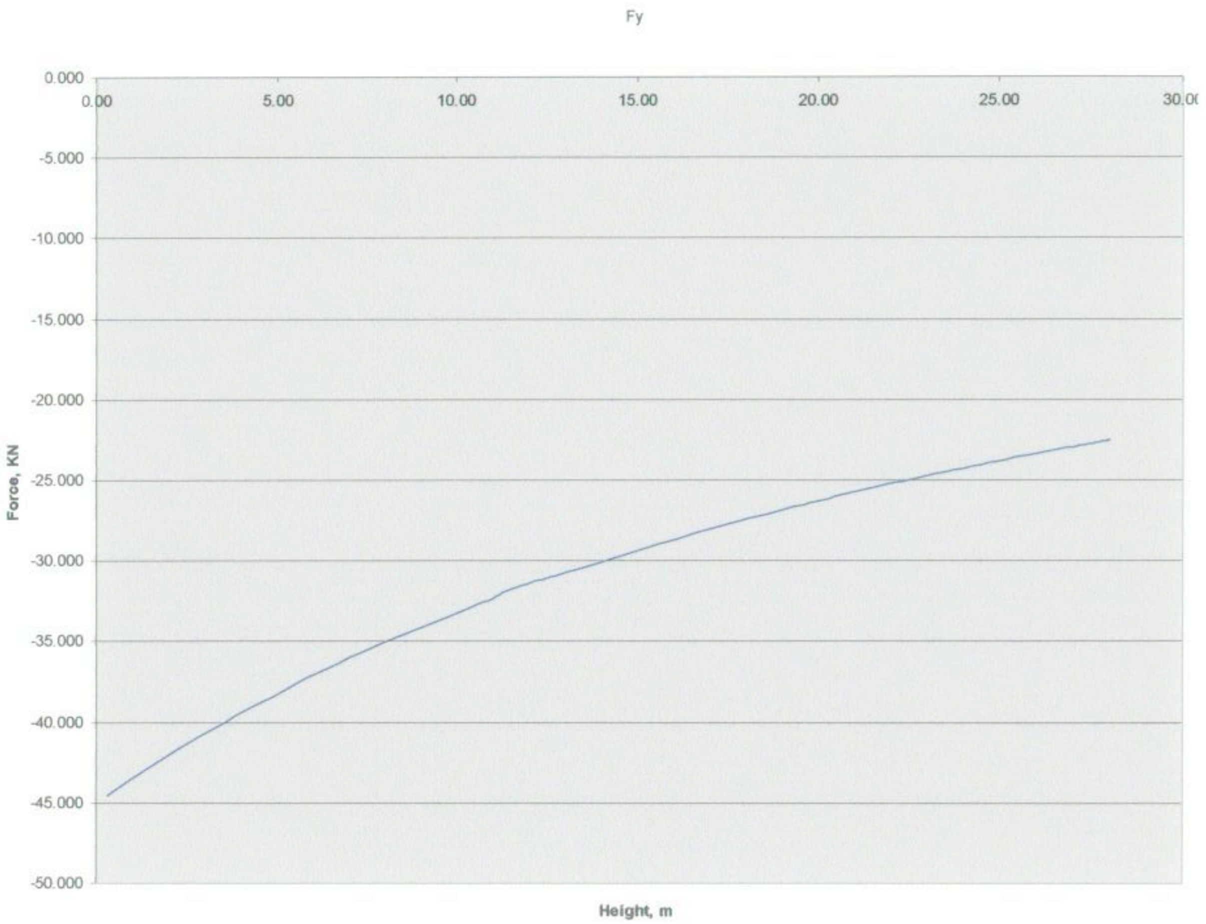

Figure 4-11 – Height vs. Fy for 56m Span Hemispherical Dome.

A plot of height vs. moments in the x and y directions are shown in Figures 4-12 and 4-13 below. Mx and My show a general increasing trend with increase in height.

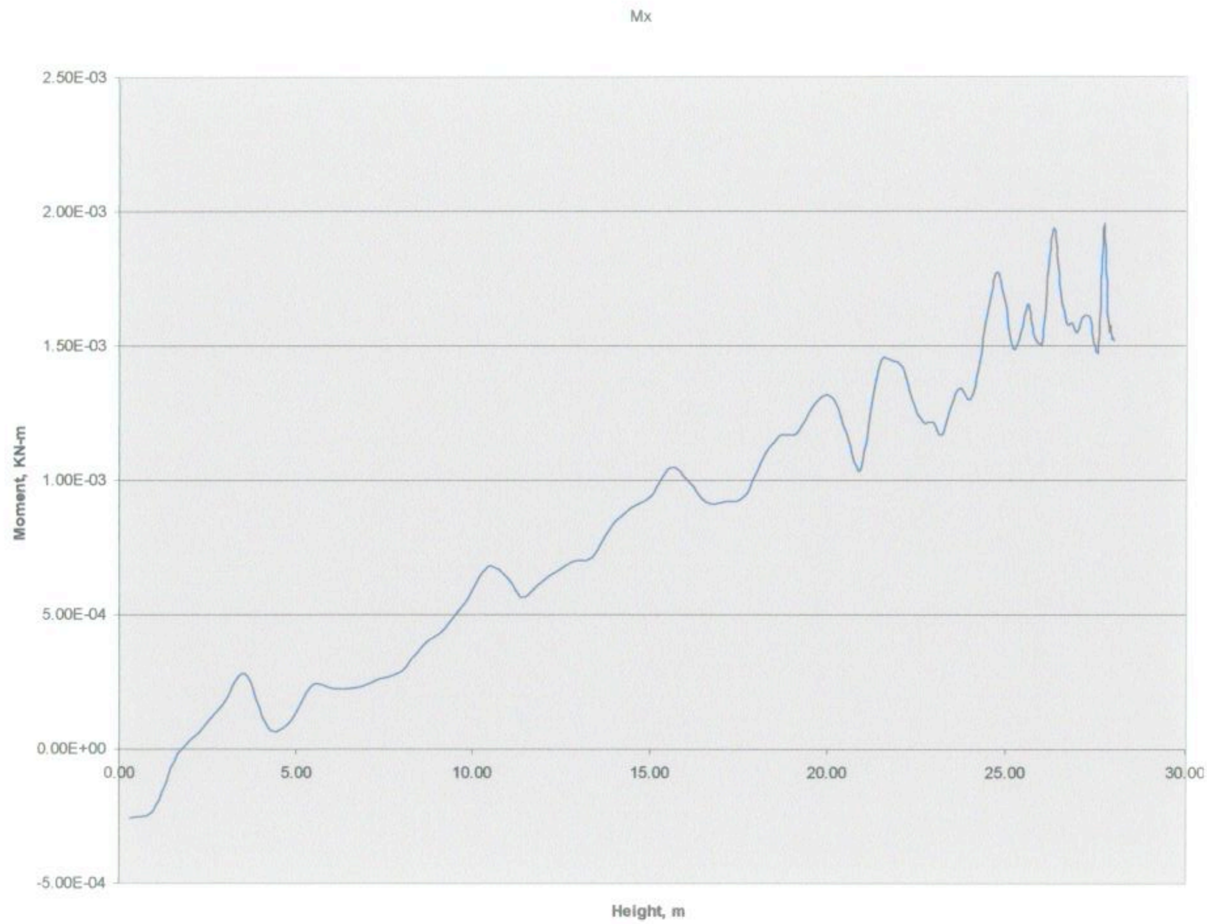

Figure 4-12 – Height vs. X-Moments for 56m Span Hemispherical Dome.

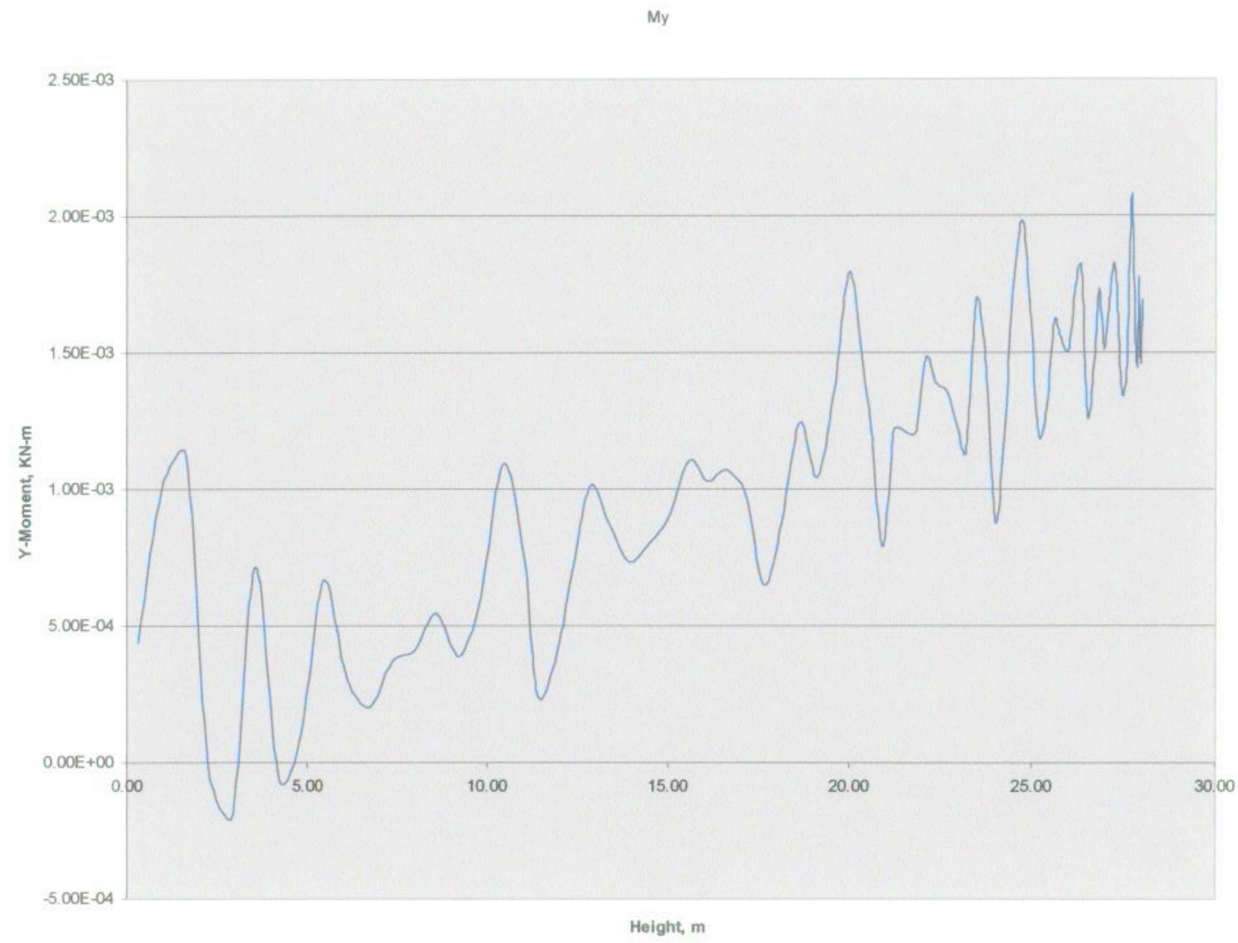

Figure 4-13 – Height vs. Y-Moments for 56m Span Hemispherical Dome.

For the same vertical row, the meridional and hoop stresses were analyzed at the center of each element. Table 4-3 lists the element number, the vertical distance to the center of each element, the hoop, and meridional stresses that were calculated by NASTRAN, and the hoop and meridional stresses calculated using shell theory.

Table 4-3—Comparison of Stresses Between FEA and Theory from Bottom Edge to Apex of 56m Span Dome.

Element	Height, m	Φ, degrees	σ_θ, KPa, FEA	σ_θ, KPa, Theory	σ_φ , KPa, FEA	σ_φ , KPa, Theory
45	0.32	89.35	629.92	629.3632	-635.96	-636.723
133	0.97	88.01	600.03	600.127	-621.03	-622.437
221	1.62	86.68	571.46	571.5179	-607.32	-608.778
309	2.26	85.37	543.78	543.9222	-595.77	-595.902

397	2.90	84.06	516.73	516.8599	-583.59	-583.56
485	3.55	82.72	490.18	489.8872	-570.59	-571.537
573	4.19	81.39	463.88	463.804	-560.16	-560.174
661	4.83	80.07	438.33	438.1637	-549.06	-549.254
749	5.46	78.76	413.40	413.3321	-537.95	-538.912
837	6.09	77.44	388.90	388.8828	-528.40	-528.953
925	6.72	76.11	364.91	364.7948	-518.95	-519.355
1013	7.35	74.78	341.37	341.049	-509.56	-510.099
1101	7.97	73.46	318.25	317.9966	-500.70	-501.307
1189	8.59	72.13	295.67	295.2422	-492.08	-492.812
1277	9.20	70.82	273.51	273.1312	-484.17	-484.731
1365	9.81	69.49	251.78	251.2809	-476.14	-476.911
1453	10.41	68.17	230.56	230.0311	-468.05	-469.461
1541	11.01	66.85	209.69	209.0105	-461.29	-462.24
1629	11.40	65.97	189.24	195.465	-454.99	-457.665
1717	11.99	64.65	169.21	175.1427	-448.10	-450.913
1805	12.77	62.87	149.50	148.576	-441.03	-442.286
1893	13.34	61.55	130.21	129.3677	-435.07	-436.188
1981	13.90	60.24	111.51	110.658	-429.39	-430.358
2069	14.46	58.91	93.14	92.10205	-423.68	-424.682
2157	15.01	57.58	75.08	74.02134	-418.15	-419.251
2245	15.55	56.26	57.50	56.40281	-412.69	-414.053
2333	16.09	54.93	40.17	38.91163	-407.75	-408.982
2421	16.61	53.61	23.24	22.1843	-402.87	-404.214
2509	17.13	52.28	6.86	5.566836	-398.34	-399.557
2597	17.64	50.95	-9.14	-10.628	-394.33	-395.092
2685	18.14	49.62	-24.73	-26.4094	-389.80	-390.811
2773	18.62	48.32	-40.08	-41.4732	-385.27	-386.787
2861	19.10	46.99	-55.12	-56.455	-381.60	-382.845
2949	19.57	45.66	-69.68	-71.0476	-377.46	-379.062
6029	19.96	44.53	-81.92	-83.1	-373.77	-375.98
6117	20.28	43.59	-91.72	-92.952	-371.59	-373.488
6205	20.59	42.66	-101.35	-102.465	-369.56	-371.105
6293	20.90	41.72	-110.82	-111.947	-367.70	-368.753
6381	21.20	40.79	-119.78	-121.096	-364.89	-366.504
6469	21.50	39.84	-128.67	-130.217	-362.68	-364.283
6557	21.80	38.87	-137.67	-139.312	-360.52	-362.088
6645	22.09	37.91	-146.53	-148.078	-358.06	-359.992
6733	22.38	36.94	-155.33	-156.82	-356.10	-357.92
6821	22.66	35.97	-163.92	-165.238	-354.11	-355.942
6909	22.94	34.99	-172.17	-173.635	-352.32	-353.985
6997	23.21	34.01	-180.35	-181.711	-350.55	-352.119
7085	23.47	33.05	-188.19	-189.47	-348.03	-350.34
7173	23.73	32.06	-195.82	-197.211	-346.50	-348.579
7261	23.99	31.04	-203.38	-204.934	-345.57	-346.836
7349	24.23	30.08	-210.62	-212.048	-343.56	-345.242
7437	24.47	29.08	-217.62	-219.147	-341.33	-343.663
7525	24.71	28.05	-224.46	-226.232	-339.51	-342.098
7613	24.94	27.04	-231.26	-233.008	-338.39	-340.612
7701	25.16	26.03	-237.93	-239.478	-337.55	-339.202
7789	25.38	24.98	-244.16	-245.936	-336.04	-337.804
7877	25.58	24.00	-250.13	-251.797	-334.35	-336.543
7965	25.78	22.97	-256.15	-257.648	-333.17	-335.292

8053	25.98	21.90	-261.82	-263.49	-332.05	-334.05
8141	26.16	20.89	-266.87	-268.741	-330.68	-332.939
8229	26.34	19.83	-271.79	-273.983	-329.48	-331.837
8317	26.51	18.78	-276.95	-278.928	-329.10	-330.802
8405	26.67	17.73	-281.77	-283.576	-327.88	-329.834
8493	26.82	16.69	-286.21	-287.929	-326.64	-328.931
8581	26.96	15.66	-290.42	-291.987	-326.07	-328.093
8669	27.10	14.57	-294.27	-296.04	-325.07	-327.26
8757	27.22	13.56	-297.88	-299.512	-324.17	-326.548
8845	27.34	12.46	-301.22	-302.98	-323.77	-325.84
8933	27.45	11.38	-304.41	-306.156	-323.43	-325.194
9021	27.55	10.29	-307.30	-309.042	-322.80	-324.608
9109	27.63	9.32	-309.50	-311.348	-321.68	-324.142
9197	27.71	8.25	-311.64	-313.654	-321.01	-323.676
9285	27.78	7.19	-313.92	-315.67	-321.17	-323.27
9373	27.84	6.13	-315.73	-317.397	-321.00	-322.923
9461	27.89	5.08	-317.12	-318.836	-320.29	-322.634
9549	27.93	4.05	-318.31	-319.987	-320.30	-322.403
9637	27.96	3.06	-319.17	-320.85	-320.21	-322.23
9725	27.98	2.17	-319.78	-321.425	-319.80	-322.115

A plot of height vs. hoop stress was generated for both the finite element analysis results and the shell theory results. The comparison is shown below in Figure 4-14.

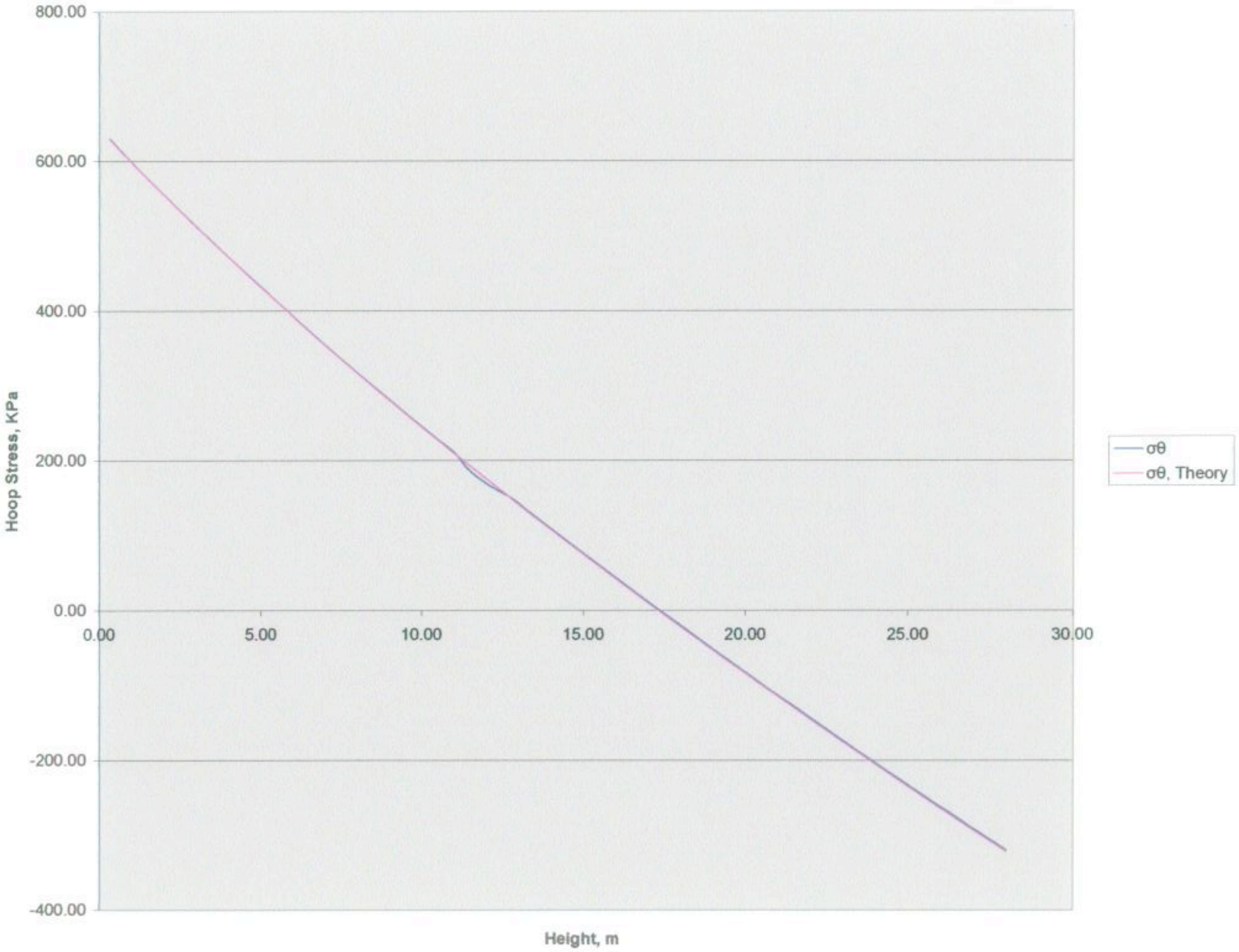

Figure 4-14 – Comparison of FEA and Shell Theory with Height vs. Hoop Stress for 56m Span Hemispherical Dome.

A plot of height vs. meridional stress for shell theory and FEA was also generated and is shown in figure 4-15.

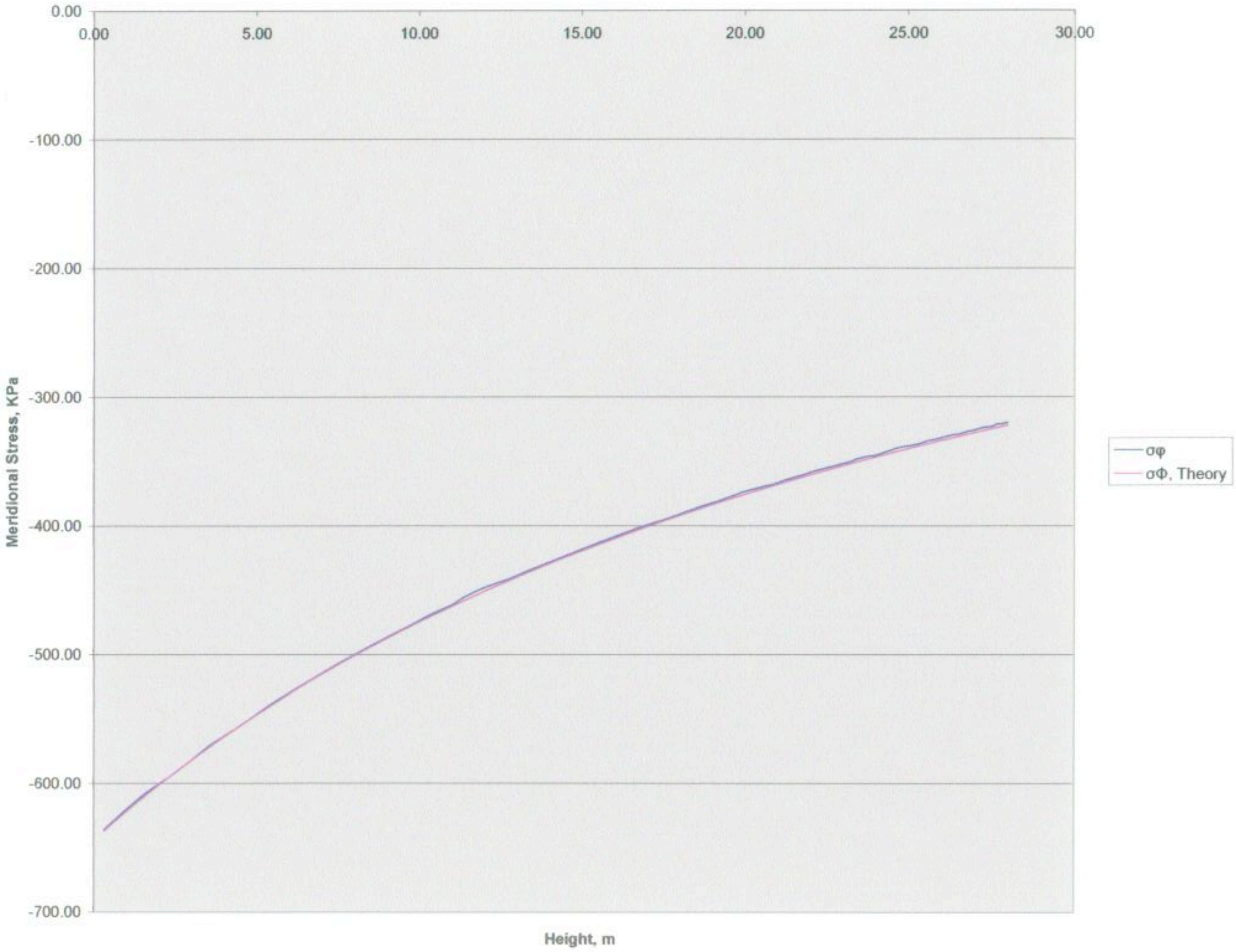

Figure 4-15—Comparison of FEA and Shell Theory with Height vs. Meridional Stress for 56m Span Hemispherical Dome.

The finite element results and shell theory results are virtually equal. However, caution must be exercised when building the finite element model. A small error in any of the steps of model creation can produce results that are drastically different than the results from shell theory. Therefore, it is imperative that a comparison is made between FEA and theory for the basic model as presented in this chapter. After positive comparison, the finite element model of the hemispherical dome is found to be valid and more complicated examples can be explored.

Chapter 5

A COMPARISON BETWEEN SHELL THEORY AND FEA FOR A TRUNCATED DOME

The stresses on a truncated hemispherical dome as calculated by the NASTRAN Finite Element Analysis results and the shell theory equations were compared using an example found on page 207 of "Stresses in Plates and Shells," by A.C. Ugural (22). A simply supported covered market dome of radius, *a*, and thickness, *t*, carrying only its own weight, *p*, per unit area was considered. The hemispherical dome was to be constructed of 70-mm-thick concrete of unit weight 23 KN/m^3 and span $2a = 56m$. The modulus of elasticity was given as 20GPa.

The membrane stresses at the bottom edge of the dome were calculated using the following equations from Ugural:

Meridional Stress:

$$\sigma_\varphi = -\,ap/t \,*\, [(\cos\varphi_o - \cos\varphi)/\sin^2\varphi] - P/t \,*\, (\sin\varphi_o/\sin^2\varphi) \qquad \boxed{(5\text{-}1)}$$

Hoop Stress:

$$\sigma_\theta = ap/t \,*\{\, [(\cos\varphi_o - \cos\varphi)/\sin^2\varphi] - \cos\varphi\} + P/t \,*\, (\sin\varphi_o/\sin^2\varphi) \qquad \boxed{(5\text{-}2)}$$

Where p = vertical load per unit length acting on the reinforcement ring, in this case $p = 0$. $2\varphi_o$ = the angle corresponding to the opening. In this case $\varphi_o = 10.2865°$ and the span of the reinforcement ring is 10m.

In the hemispherical case, $\varphi = 90°$. From the given information, $a = 28m$, $t = .03m$, and $p = (23\ KN/m^3 * t)$. Some domes are not closed at the upper portion and have a lantern, a small tower for lighting, and ventilation. In the case in Ugural, a reinforcing ring is used to support the upper structure.

Therefore, Equation (5-1) for meridional stress yields -633.65 KPa at the bottom edge of the dome. Equation (5-2) for hoop stress yields +633.65 KPa located at the top of the dome.

In NASTRAN, the geometry for *a* = 28m radius hemispherical dome was generated using the parasolid modeling engine. The area of the lantern was subtracted from the top of the dome. For the NASTRAN analysis, the upper structure is not supported and therefore the stresses around the ring can be read and reinforcing designed around the opening. Material properties were entered as *t* = .03m, E = 20 x 10^6 KPa, ν = 0.15, and mass density = (23 KN/m^3) / (9.81 m/s^2) = 0.002345. To include the self-weight of the dome the gravitational acceleration, 9.81 m/s^2, was entered.

A four-noded quadrilateral plane element was used in meshing the dome. A rough mesh was applied for initial comparison and then refined until the stresses converged to the values found using the Ugural stress equations. The bottom edge of the dome was constrained in the z-direction (vertically), and one node on the edge was constrained in the x, y, and z directions to provide stability during analysis.

A fine mesh was used in the analysis of the stresses as shown in Figure 5-1. The hoop stress at the bottom edge of the dome was found to be +647.5 KPa (Figure 5-2), and the meridional stress at the bottom edge of the dome was -638.1 KPa (Figure 5-3). Comparing the calculations using shell theory with the NASTRAN results, the stresses at the bottom edge of the dome were found to be approximately equal; see Table 5-1.

Table 5-1 – Shell Theory vs. FEA Stress Results for 56m Span Hemispherical Truncated Dome.

Method	Maximum Hoop Stress, KPa	Maximum Meridional Stress, KPa
Shell Theory	+633.65	-633.65
NASTRAN, FEA	+637.1	-627.8

Thus, the finite element model is valid and the stresses around the opening may be investigated further.

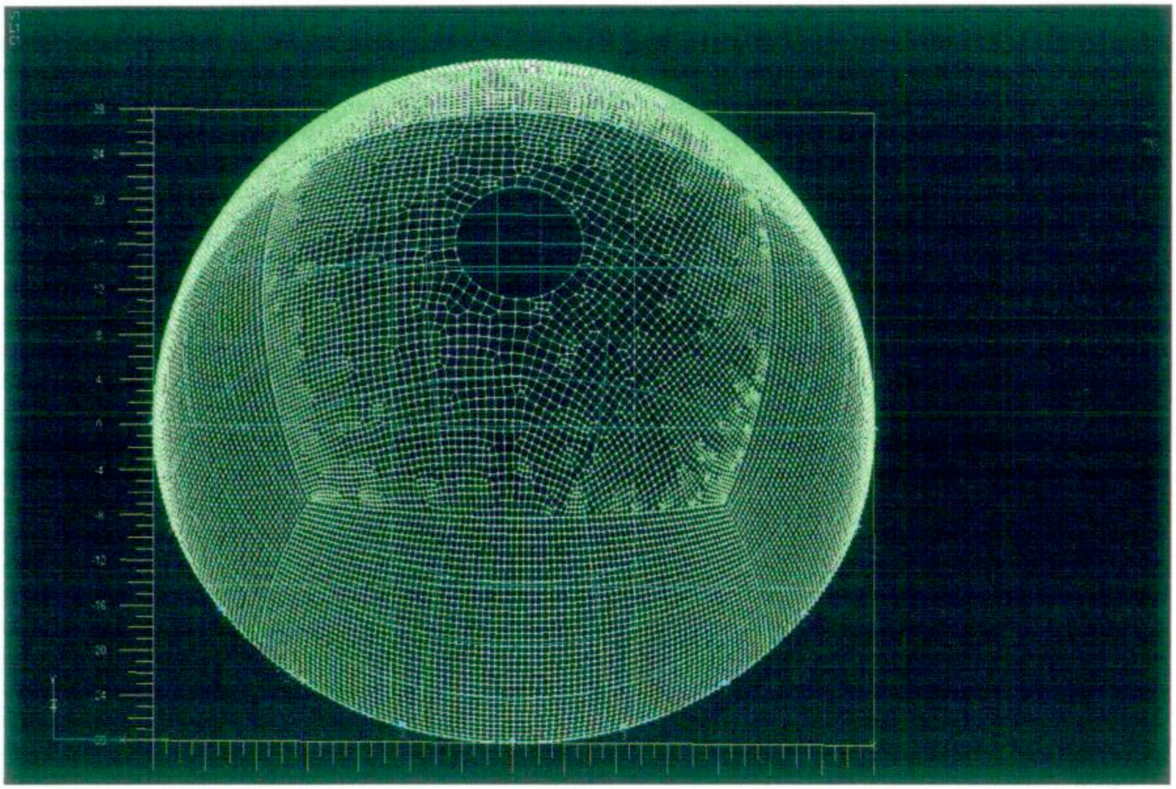

Figure 5-1 – Fine Mesh of 56m Span Truncated Hemispherical Dome in NASTRAN.

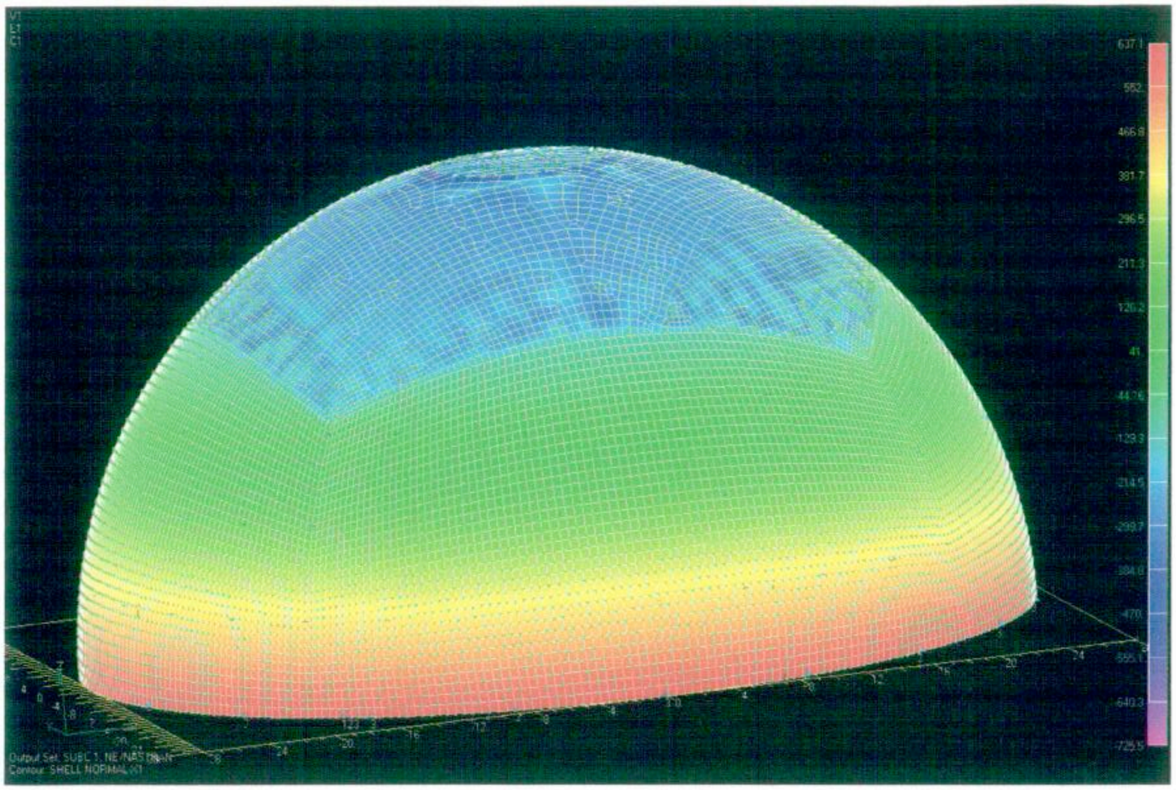

Figure 5-2 – Distribution of Hoop Stresses for Truncated 56m Span Dome.

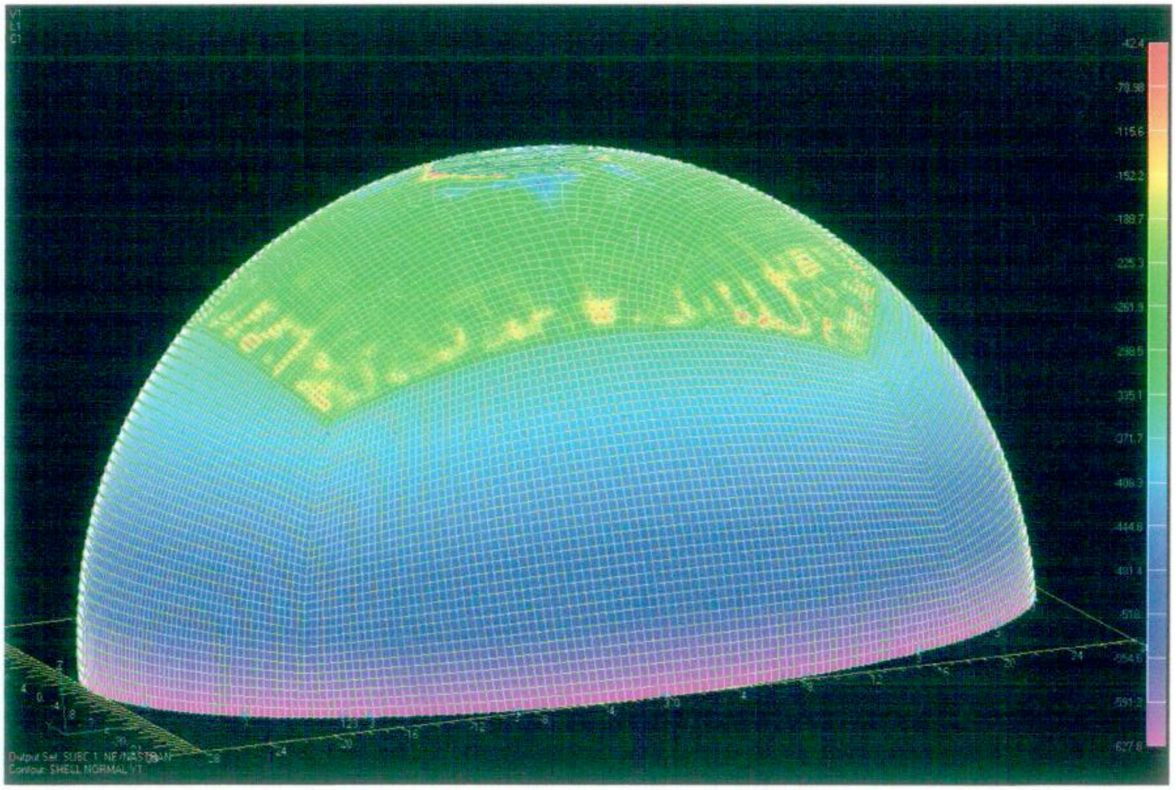

Figure 5-3 – Distribution of Meridional Stresses for Truncated of 56m Span Dome.

The maximum meridional stress around the opening was found to be -725.5 KPa using NASTRAN (Figure 5-4).

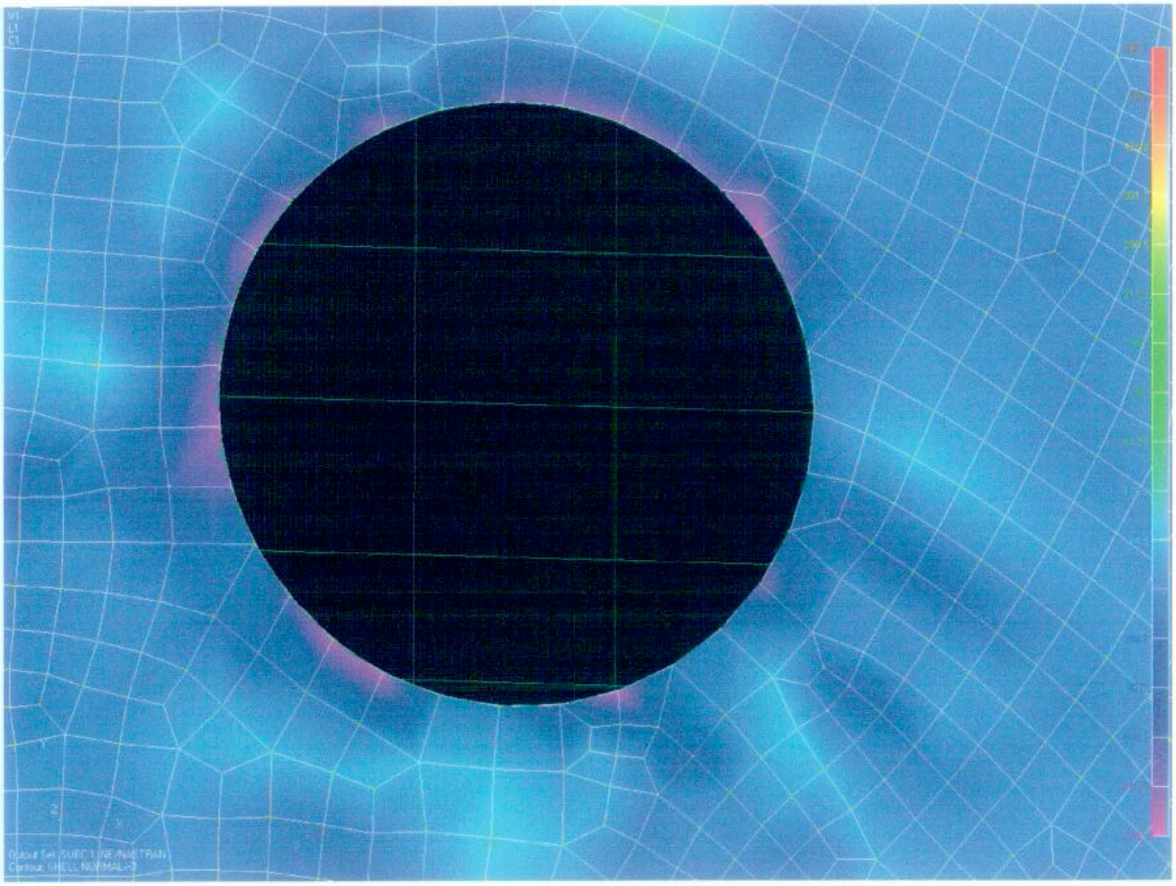

Figure 5-4 – Meridional Stress Distribution around opening.

The maximum hoop stress around the opening was significantly less than the meridional stress (approximately 300 KPa), see Figure 5-5.

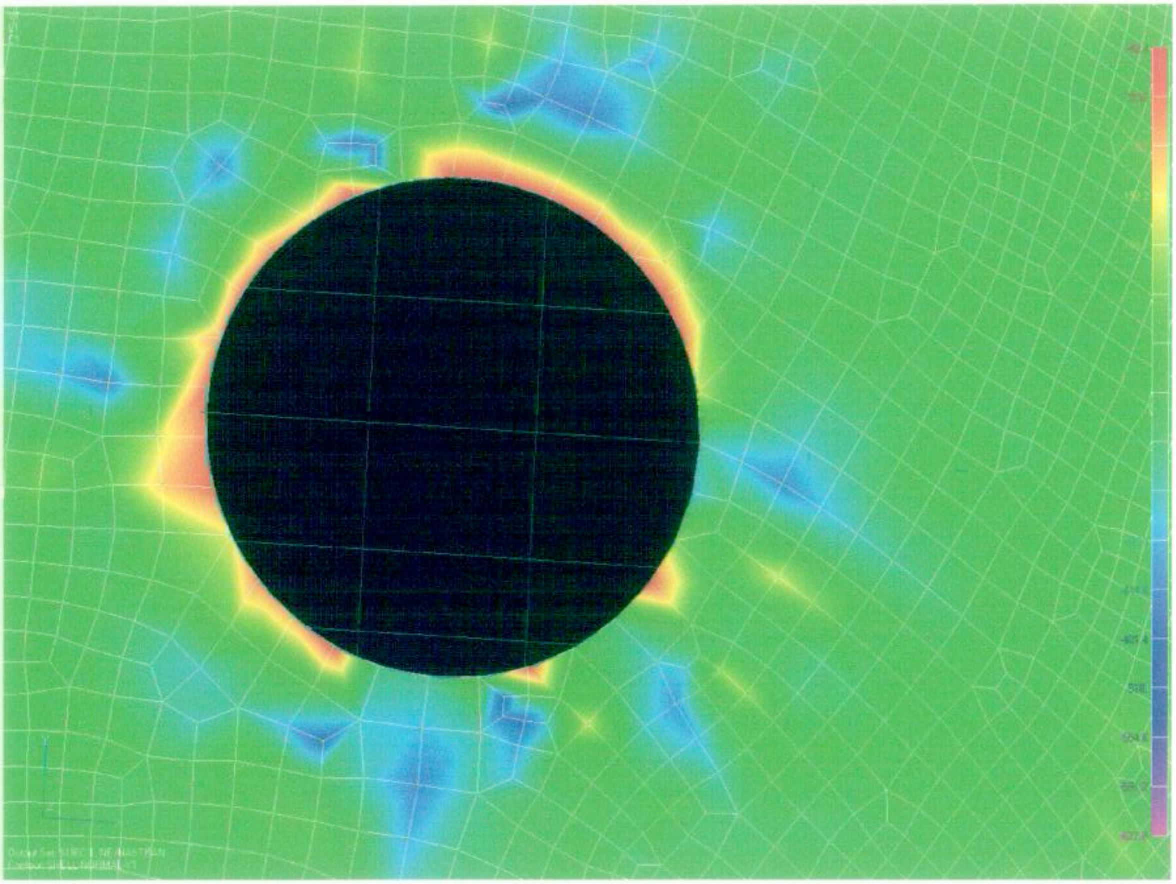

Figure 5-5 – Hoop Stress Distribution around opening.

The truncated dome example illustrates the process of building the finite element model, verifying the validity of the model by comparing the analysis with the shell theory equations, and then exploring the model further.

Chapter 6

A COMPARISON BETWEEN SHELL THEORY AND FEA FOR A NON-HEMISPHERICAL DOME

A comparison of a non-hemispherical dome was made between the NASTRAN Finite Element Analysis results and shell theory equations using an example found on page 129 of "Thin Shell Concrete Structures," by David P. Billington (1). The rigidly supported spherical dome of Figure 6-1 is analyzed for uniform gravity load over the dome surface. The parameters of the problem are: $a = 94.5$ ft, $h = 4$ in. (constant shell thickness), $\alpha = 28°$, $ro = a(\sin(\alpha)) = 44.25$ ft. (parallel circle radius at springing), $\nu = 1/6 = 0.167$ (Poisson's ratio), $q = 50$ psf (Dead Load) + 40 psf (Live Load) = 90 psf, E = 57,000*sqrt(4000 psi) = 519120 ksf, Mass Density = .0083851 for 90 psf total load.

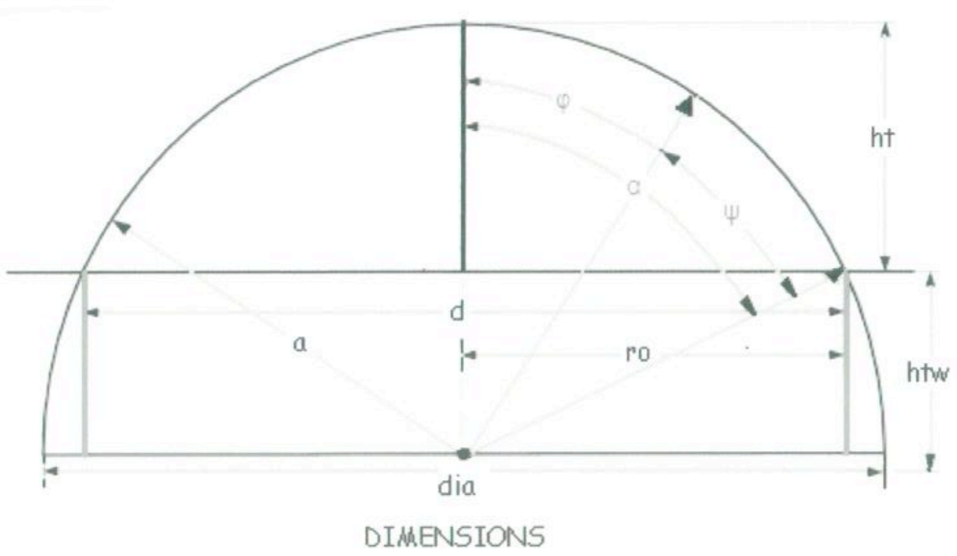

Figure 6-1: Fixed Dome for Comparison Between FEA and Billington Example.

The forces were computed on the basis of the membrane theory where

$N'_{\varphi} = -a*q*[1/(1+\cos(\varphi))]$ = meridional force,

And

$N'_\theta = a*q*[[1/(1+\cos(\varphi))]-\cos(\varphi)]$ = hoop force,

and M_φ = meridional moment, as listed in Table 6-1.

Table 6-1 – Forces in a Spherical Dome on Fixed Supports.

Ψ------------------------------	0° (edge)	28° (apex)
N_φ (q = 90 psf)	-4.29 k/ft	-4.25 k/ft
N_θ (q = 90 psf)	-0.78 k/ft	-4.25 k/ft
M_φ (q = 90 psf)	-0.26 k-ft/ft	0 k-ft/ft

In NASTRAN, the geometry for the dome was generated using the parasolid modeling engine. Material properties were entered as t = .3333 ft., E = 519120 ksf, ν = 0.167, and mass density = .0083851. To include the self-weight of the dome, an acceleration downward, due to gravity, of 32.2 ft/s^2 was entered.

A four-noded quadrilateral plate element was used in meshing the dome. A rough mesh was applied for initial comparison and then refined until the stresses converged to the values found using Billington's example. The bottom edge of the dome was completely constrained.

The FEA analysis for meridional forces is shown in Figure 6-2. The irregularity of force distribution is caused by the element shapes being slightly irregular due to the shallowness of the dome. The meridional force at the edge was found to be -4.435 k/ft and at the apex -4.22 k/ft. which are very close to the values obtained using shell theory.

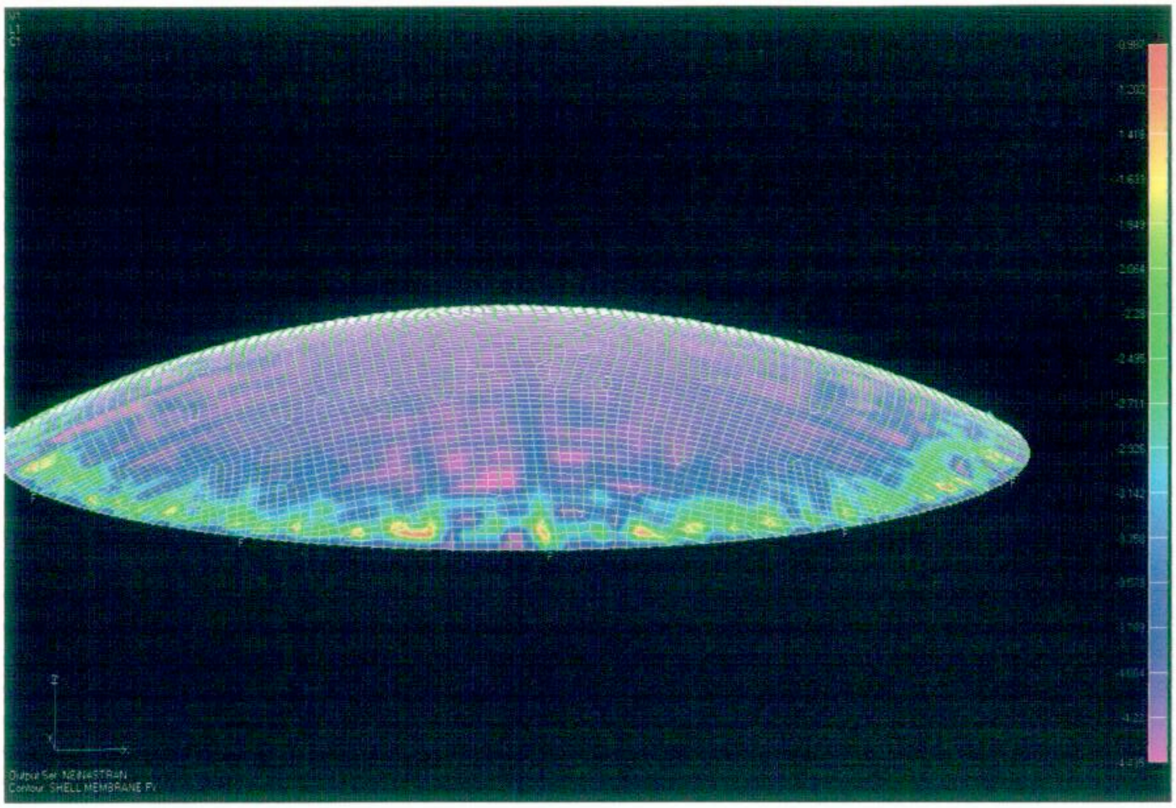

Figure 6-2—Meridional Force Distribution in Dome.

Figure 6-3 shows the force distribution (slightly irregular) for the hoop forces according to the FEA. The hoop force at the edge was found to be -0.72 k/ft and at the apex -4.205 k/ft.

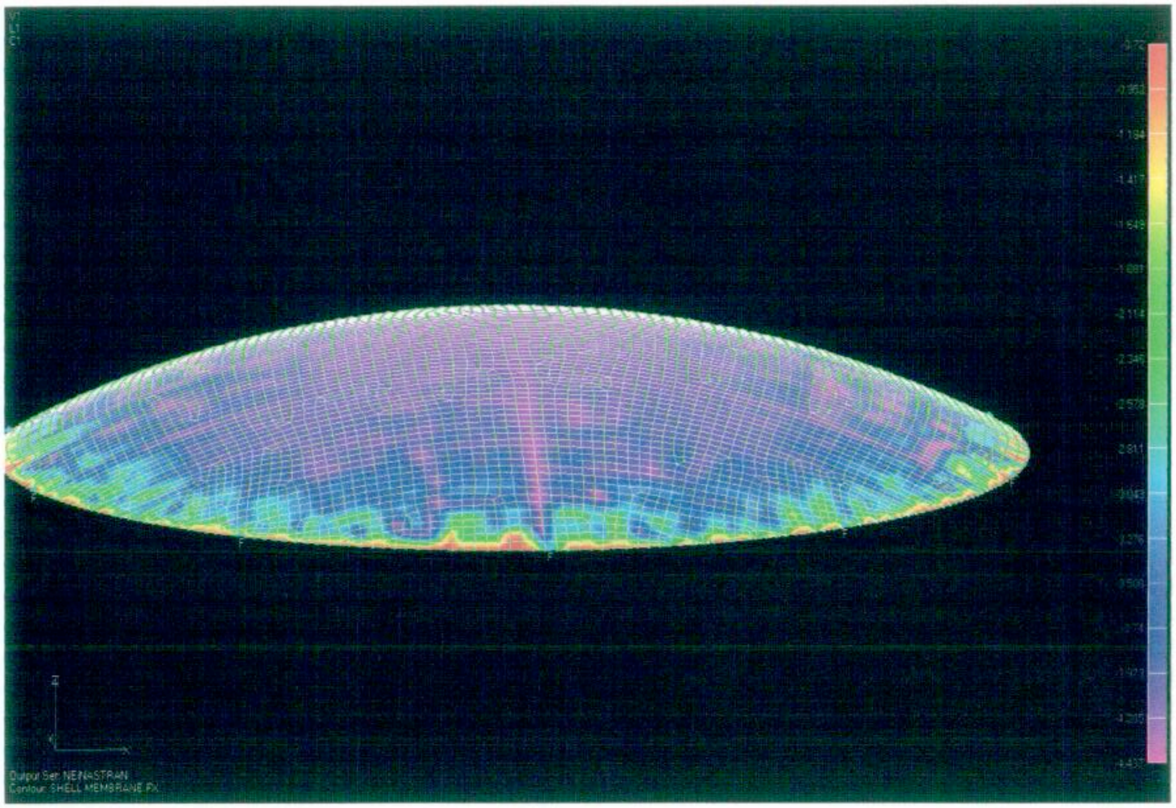

Figure 6-3—Hoop Force Distribution in Dome.

The moment distribution is shown in Figure 6-4. At the edge, the moment was found to be -0.258 k-ft/ft, and at the apex, the moment was found to be -0.00541 k-ft/ft, which is approximately zero.

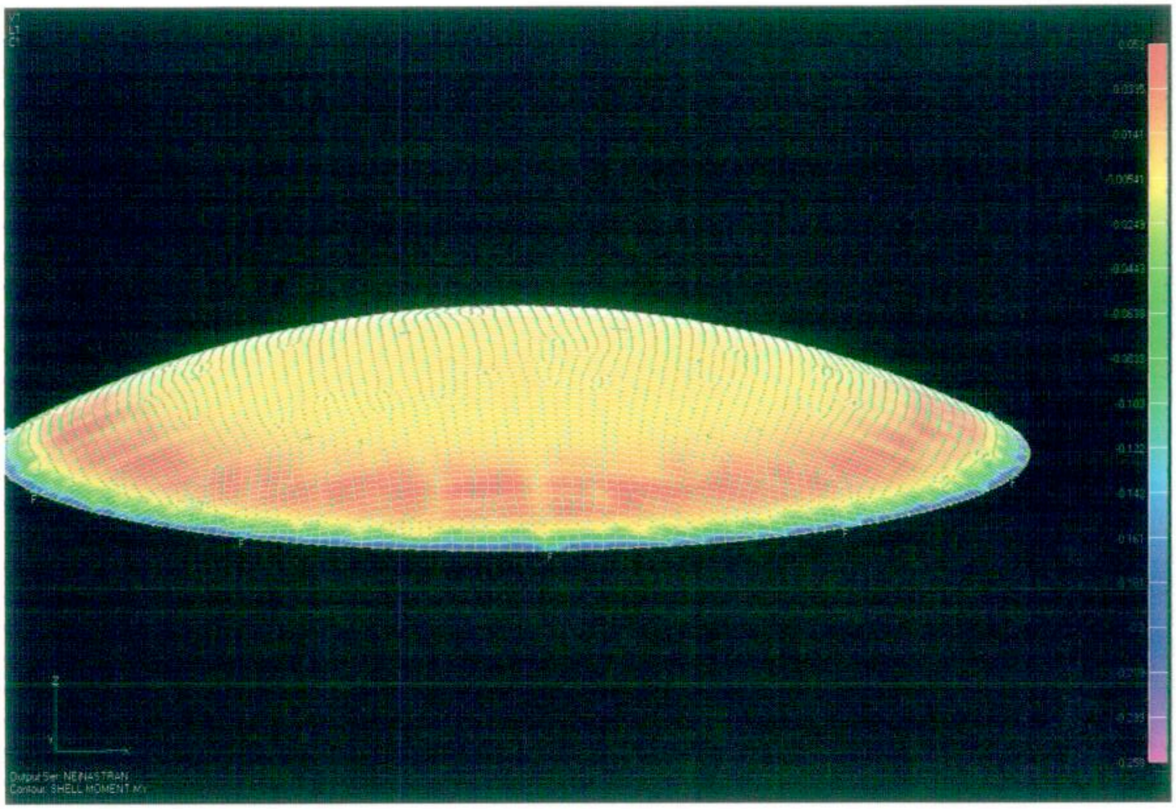

Figure 6-4—Moment Distribution in Dome.

Thus, for easy comparison, the shell theory results and the FEA results are presented side-by-side in Table 6-2.

Table 6-2—Shell Theory Results vs. Finite Element Analysis Results.

Ψ----------------	0° (edge) Shell Theory	0° (edge) FEA	28° (apex) Shell Theory	28° (apex) FEA
N_φ (q = 90 psf)	-4.29 k/ft	-4.435 k/ft	-4.25 k/ft	-4.22 k/ft
N_θ (q = 90 psf)	-0.78 k/ft	-0.72 k/ft	-4.25 k/ft	-4.205 k/ft
M_φ (q = 90 psf)	-0.26 k-ft/ft	-0.258 k-ft/ft	0 k-ft/ft	-0.00541 k-ft/ft

It can be concluded that for non-hemispherical domes, the finite element model is valid.

Chapter 7

AN INTRODUCTION TO SHELL THEORY FOR DOMES, RINGS, AND WALL INTERACTIONS

In order to compare results between theory and FEA for domes on walls, more theory must be introduced. This chapter addresses the additional calculations associated with domes, rings, and wall interactions. According to Billington, it is usually not possible to supply support tangent to the meridian at the edge of the dome. The usual case of support is by vertical supports. Figure 7-1 shows the general structural problem brought about by this situation.

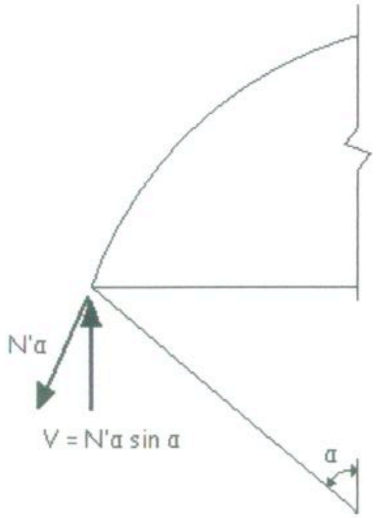

Figure 7-1—Dome Edge Reactions from Billington (1).

The membrane reaction N′α cannot be supplied by a vertical support. Thus, there exists a horizontal displacement at the dome edge. The resulting dome forces may be determined by combining the membrane values with those obtained from an analysis of the dome pulled outward by an edge force $H = - N'\alpha \cos \alpha$. It is usual practice for the designer to impose some type of lateral restraint. Billington discusses three types: an edge ring, a supporting cylindrical wall, and a combination of ring and wall. The ring support of Figure 7-2a is often realized in practice by an elastomeric ring pad placed on top of the cylindrical wall. Some shear force will be transferred through the pad depending upon the pad's stiffness (23).

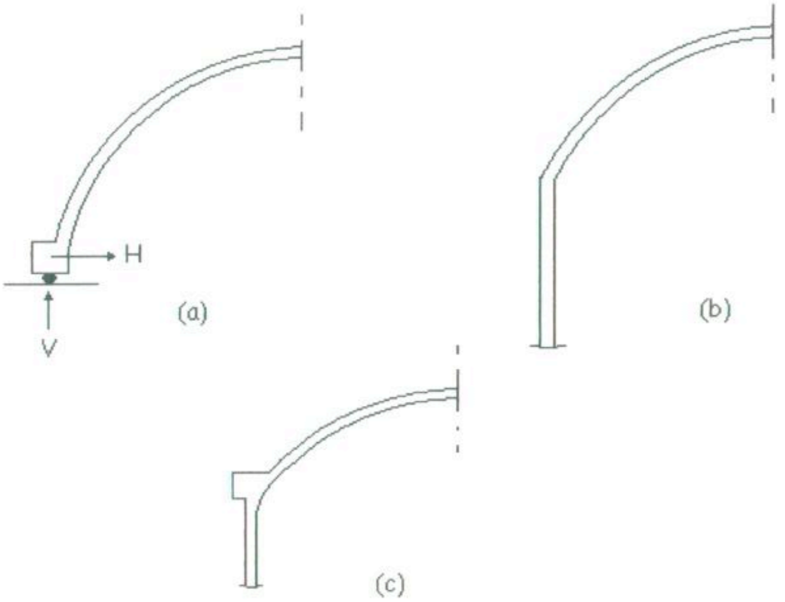

Figure 7-2—Dome Edge Constructions from Billington. (a) Dome-Ring Edge Construction, (b) Dome-Wall Edge Construction, (c) Dome-Ring-Wall Edge Construction.

Dome-Ring Analysis

In Billington's dome and ring example, illustrated in Figure 7-2a, the ring is assumed to be monolithic with the dome and to be free to slide and rotate on an immovable support.

The stress resultants in the dome are computed using membrane theory previously discussed. The horizontal component of $N'\alpha$ is held in equilibrium by the ring tension $T = N'\alpha \sin\alpha \cos\alpha$, where the dome radius $a = r/\sin\alpha$ (see Figure 7-3a) (23).

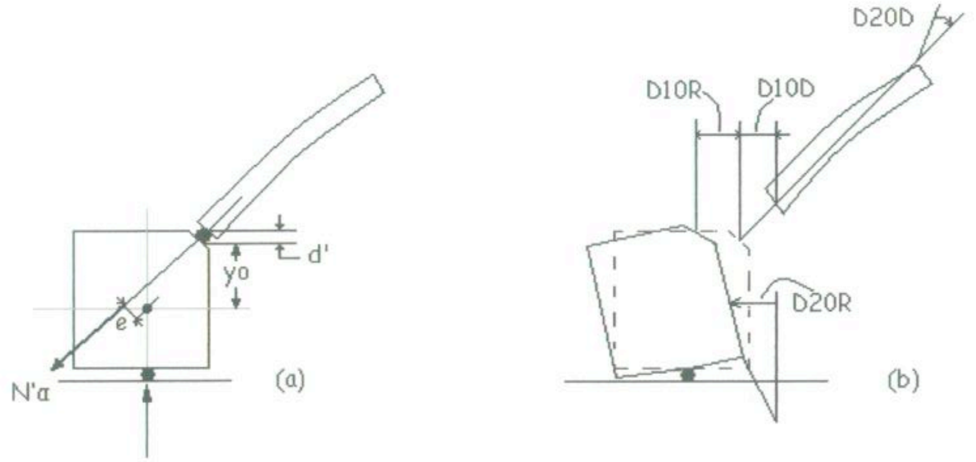

Figure 7-3—Dome-Ring Analysis from Billington (1).

Because of the displacements at the dome edge and the resulting dome stresses, there will be four errors* (see note at chapter end): horizontal translation and rotation of the dome edge (D10D and D20D) and of the ring (D10R and D20R); see Figure 7-3, (notation from Billington). The dead-load displacements at the edge of a constant-thickness spherical dome are:

$$D10D = (a^2q/Eh) * [((1+\nu)/(1+\cos\alpha)) - \cos\alpha] \sin\alpha$$

$$D20D = -(aq/Eh) * (2+\nu)\sin\alpha$$

And the ring errors are:

$$D10R = (\cos\alpha + (12*yo*e/d^2))*(r^2* N'\alpha/E*b*d)$$

$$D20R = -(12*r^2*e* N'\alpha)/(E*b*d^3)$$

Where d is the depth of the ring, b is the width of the ring, and r is the radius of the ring. N′α is taken as negative and e as positive in the direction shown on Figure 7-3a. The variables d′ and yo are defined below:

$$d' = hd/2 * \cos\alpha$$

$$yo = d/2 - d'$$

Where hd is the dome-edge thickness and d′ is generally small compared to d (see Figure 7-3a) (23).

The errors are combined to yield:

D10 = D10D + D10R

D20 = D20D + D20R

There are two correction forces needed*, designated X_1 and X_2. The dome displacements due to X_1 and X_2 (D11D, D12D, D21D, D22D), are as follows (23):

$$D11D = [(2*\beta*a^2*\sin^2 \alpha)/(E*h)]*H$$

$$D12D = [(2*\beta*a^2* \sin \alpha)/E*h] * M\alpha$$

$$D21D = [(2*\beta^2*a^2* \sin \alpha)/E*h] * H$$

$$D22D = [(4* \beta^3*a^2)/E*h] * M\alpha$$

Where

$$B^4 = [3 * (1 - \nu^2)]/(a^2*h^2)$$

H and Mα are edge forces and moments.

The ring displacements (D11R, D12R, D21R, and D22R), are as follows (23):

$$D11R =\{1 + [(12 * y_o^2)/d^2]\}*[r^2/(E*b*d]$$

$$D12R = D21R = - (12*r^2*yo)/(E*b*d^3)$$

$$D22R = (12*r^2)/(E*b*d^3)$$

These values are now combined directly with the corresponding dome displacements so that (23):

$$D11 = D11D + D11R$$

$$D12 = D21 = D12D + D12R$$

$$D22 = D22D + D22R$$

Compatibility equations are written and solved for X_1 and X_2 (23):

$$X_1 D11 + X_2 D12 + D10 = 0$$

$$X_1 D21 + X_2 D22 + D20 = 0$$

Note that the ring is in tension and the dome is usually entirely in compression. The membrane ring tension, $T = N'\alpha * r * \cos\alpha$, forces the ring outward. Compatibility requires that the dome follow this movement. The ring will not move as far as theory predicts because of the restraint of the dome. Thus, the ring force is reduced by X_1 (23).

Dome-Wall Analysis

According to Billington, it is possible to resist the horizontal component of the membrane meridional thrust by building the dome into a cylindrical wall. Figure 7-4 illustrates the system in which the dome is considered supported fully by the wall. The wall has a continuous edge force N'α under the dome load. It can be resolved into two components (23):

$$H = N'\alpha \cos\alpha$$

$$V = N'\alpha \sin\alpha$$

Chapter 8

DOME-RING-WALL EXAMPLE AND COMPARISON

It has become common practice to construct domes on stem walls, as shown in Figure 8-1. Thus, a comparison between a dome-ring-wall solution from shell theory and a finite element analysis (FEA) is practical. For this purpose, FEA results using Nastran are compared to an example found on page 153 of David P. Billington's text, "Thin Shell Concrete Structures"

Figure 8-1-- Texhoma, Oklahoma-- Texhoma School District educates approximately 426 students in grades five through twelve. Architectural walls enhance the dome's appearance while giving the ac/heating units a place to hide.

The horizontal force, $N'_\alpha \cos\alpha$, causes the wall to move outward and rotate*. Thus (23):

$D11W = 1/(2*\beta^3*D)$

$D21W = -1/(2*\beta^2*D)$

$D22W = 1/(\beta^*D)$

Where $D = (E*Hw^3)/(12*(1-v^2))$, and Hw = the height of the wall.

For the edge load $N'_\alpha \cos\alpha$, these values become (23):

$D10W = (N'_\alpha \cos\alpha)/(2*\beta^3*D)$

$D20W = -(N'_\alpha \cos\alpha)/(2*\beta^2*D)$

Displacements due to correction force $X_1 = 1$ and correction moment $X_2 = 1$ are now determined by adding the values already shown for the dome and wall* (23):

$D11 = D11D + D11W$

$D12 = D12D + D12W = D21$

$D22 = D22D + D22W$

The two compatibility equations are written in the same form as before and the values of X_1 and X_2 are determined (23).

Dome-Ring-Wall Analysis

When a wall replaces the ring, high tensile stresses develop in the edge region of the cylinder. This high tension often requires heavy reinforcement and an increase in wall thickness. Billington points out that in liquid-retaining structures it is not desirable to have large regions of high ring tension because of the possibility that cracks and leaks may develop (23).

It is then more desirable to collect the tension forces back up into a ring. Figure 7-4 illustrates the dome-ring-wall action.

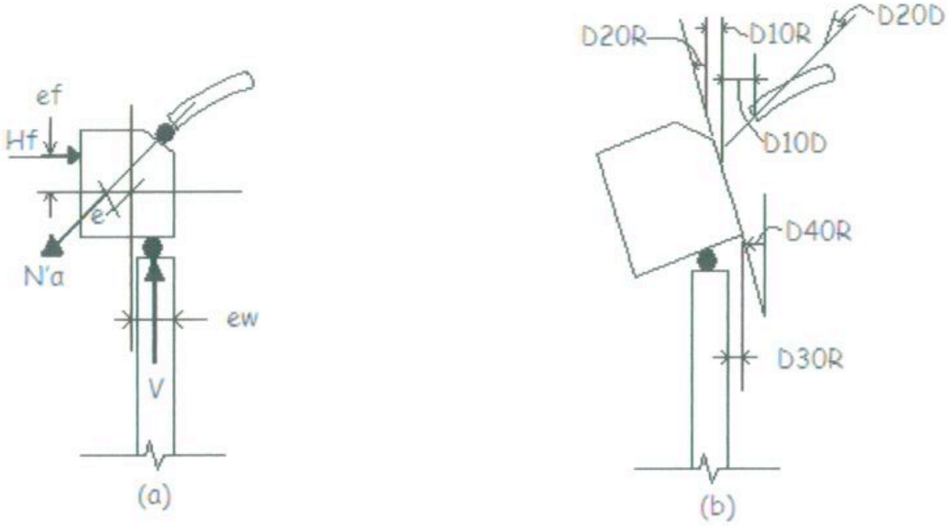

Figure 7-4—Dome-Ring-Wall Analysis from Billington (1).

Figure 7-4a illustrates the system in which all stress resultants for the dome and the wall are determined by the membrane theory (23).

There are eight errors* (see Table 7-1) associated with the dome-ring-wall analysis; namely, translation and rotation of the dome, the top of the ring, the bottom of the ring, and the wall (D10D, D20D, D10R, D20R, D30R, D40R, D30W, and D40W, respectively) (see Figure 7-4) (23).

Table 7-1—Displacements for Dome-Ring-Wall Analysis (Errors)

(Rectangular ring cross section).

LOAD	LOAD ON DOME
D10D (Dome)	$(a^2q/Eh) * [((1+\nu)/(1+\cos\alpha)) - \cos\alpha] \sin\alpha$
D20D (Dome)	$-(aq/Eh) * (2+\nu)\sin\alpha$
D10R (Ring Top)	$(\cos\alpha + (12*yo*et/d^2))*(r^2* N'\alpha/E*b*d)$
D20R (Ring Top)	$-(12*r^2*et* N'\alpha)/(E*b*d^3)$
D30R (Ring Bottom)	$(-\cos\alpha + (6*et/d))*(r^2* N'\alpha/E*b*d)$
D40R (Ring Bottom)	$+(12*r^2*et* N'\alpha)/(E*b*d^3)$
D30W (Wall)	0
D40W (Wall)	0

There are four corrections* associated with the dome-ring-wall analysis: a force X_1 and a moment X_2, which correspond to the required dome-ring values; and a force X_3 and a moment X_4, which correspond to a ring-wall analysis.

Due to the force X_1, obtained as before:

$$D11 = D11D + D11R$$

From the force X_2 again:

$$D12 = D12D + D12R$$

From the ring-wall forces X_3 and X_4 come the displacements:

$$D13 = D13R = -[(1/bd) - (12*yo*(d/2)/(b*d^3))*(r^2/E)$$

And

$$D14 = D14R = (12*yo*r^2)/(b*d^3)$$

The rotation of the ring at the junction due to X_3 is:

$$D23 = -(12*r^2*(d/2))/(E*b*d^3)$$

And the rotation due to X_4 is:

$D24 = -(12*r^2)/(E*b*d^3)$

The displacements at the ring-wall junction are:

$D31 = D13 = - [(1/bd) – (12*yo*(d/2)/(b*d^3))*(r^2/E)$

$D32 = D23 = -(12*r^2*(d/2))/(E*b*d^3)$

$D33 = D33R + D33W$

Where

$D33R = \{1 + [(12 * (-d/2)^2)/d^2]\}*[r^2/(E*b*d]$

$D34R = - (12*r^2*(-d/2))/(E*b*d^3)$

$D33W = 1/(2*\beta^3*D)$

$D34W = - 1/(2* \beta^2*D)$

Then,

$D34 = D34R + D34W$

$D41 = D14 = (12*yo*r^2)/(E*b*d^3)$

$D42 = D24 = -(12* r^2)/(E*b*d^3)$

$D43 = D34$

$D44 = D44R + D44W$

Where

$D44R = (12*r^2)/(E*b*d^3)$

$D44W = 1/ (\beta^*D)$

There are now four simultaneous compatibility equations to solve for the four corrections X_1, X_2, X_3, and X_4.

Now, the corrections combined with the basic shell theory equations can be used to analyze and compare domes on rings or walls.

*Derivations for errors and correction equations can be found in "Thin Shell Concrete Structures," Second Edition, David P. Billington, McGraw-Hill Publishing Company 1990.

Figure 8-2 gives the dimensions of a 1-million-gal water tank to be built above grade. This tank will serve the purpose of this example.

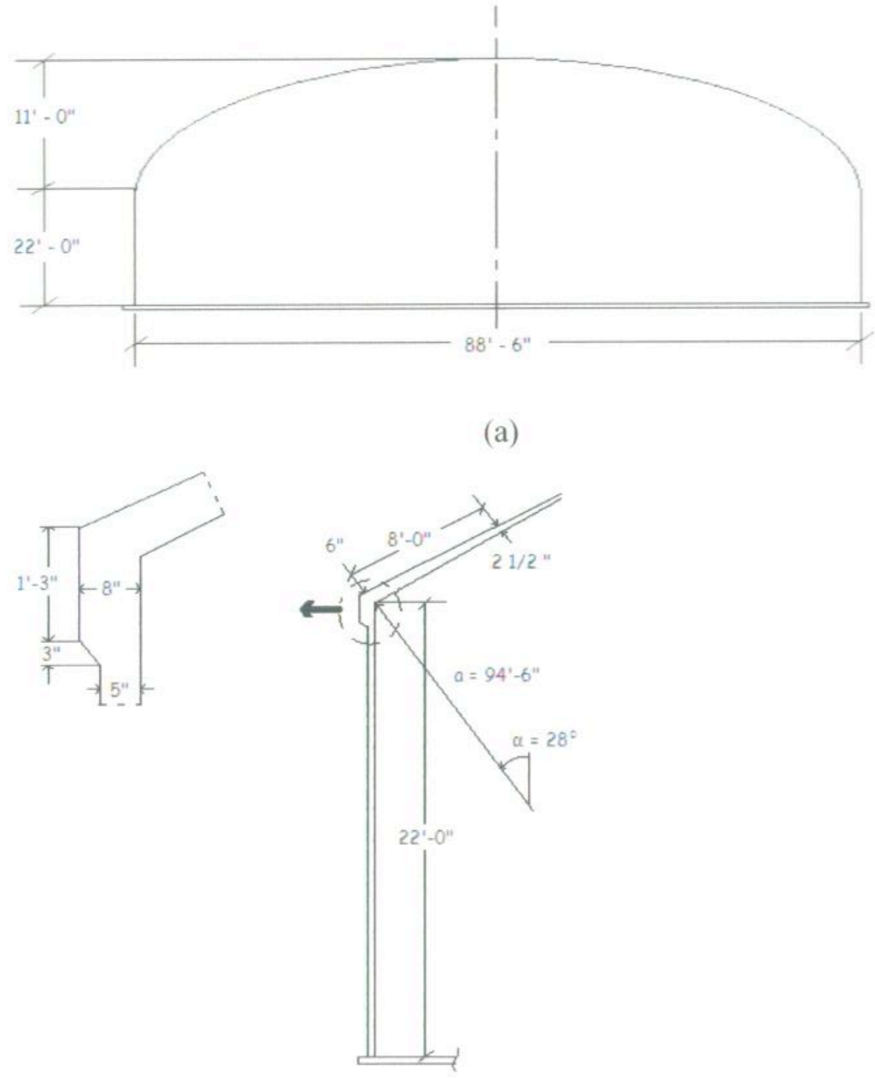

(a)

(b)

Figure 8-2—Domed Tank Dimensions from Billington (1).

For the purpose of the finite element analysis, the dome-ring-wall junction is modeled as shown in Figure 8-3.

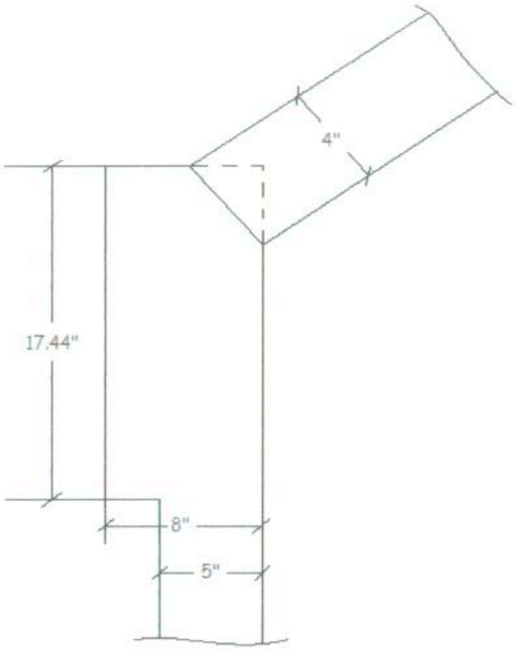

Figure 8-3—Idealization of Dome-Ring-Wall Junctions for FEA from Billington (1).

The simply-supported water tank is analyzed for uniform gravity load plus live load over the surface. In NASTRAN, the geometry for a 94'-6" radius hemispherical dome was generated using the parasolid modeling engine. It was then sliced at a circle defined 11'-0" from the apex of the dome. The dome thickness was idealized as 4 in. uniform. A 20.5467 ft. tall cylinder was generated with a radius of 44.25 ft. to represent the wall, and a 17.44 in. tall cylinder with the same radius was generated to represent the ring. The wall thickness was entered as 0.41667 ft. and the ring thickness was 0.6667 ft. Material properties were assumed to be: $\nu = 1/6 = 0.167$ (Poisson's ratio), $q = 50$ psf (Dead Load) + 40 psf (Live Load) = 90 psf, $E = 57{,}000*\text{sqrt}(4000 \text{ psi}) = 519120$ ksf, Mass Density = .0083851 for 90 psf total load.

The bottom edge of the wall was constrained in the z-direction (vertically), and one node on the edge was constrained in the x, y, and z directions to provide stability during analysis. To include the self-weight of the dome, the gravitational acceleration of 32.2 ft/s^2 was entered. A four-noded quadrilateral plate element was used in meshing the dome. A rough mesh was applied for initial comparison and then refined until the forces converged.

Figure 8-4 shows the FEA distribution of hoop force found in the water tank model. The mesh on the dome is slightly irregular causing some non-uniformity in the force distribution (due to the shallow dome height). The hoop force in the dome at the junction of the dome at the ring was found to be 25.2 k/ft. The hoop force at the junction of the ring and wall was 2.797 k/ft.

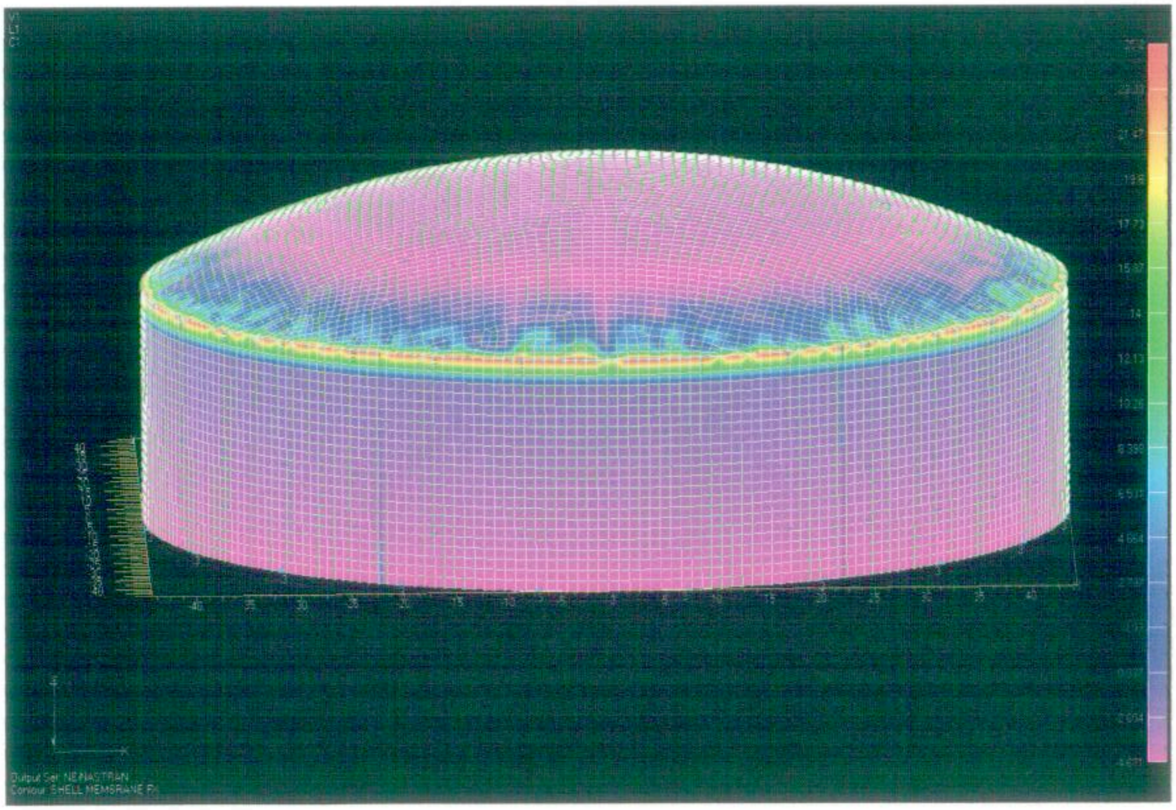

Figure 8-4—Hoop Force Distribution in Water Tank.

The meridional force distribution as found by the finite element analysis is shown in figure 5. The meridional force in the dome at the junction of the dome at the ring was found to be -2.147 k/ft. The meridional force at the junction of the ring and wall was 4.161 k/ft.

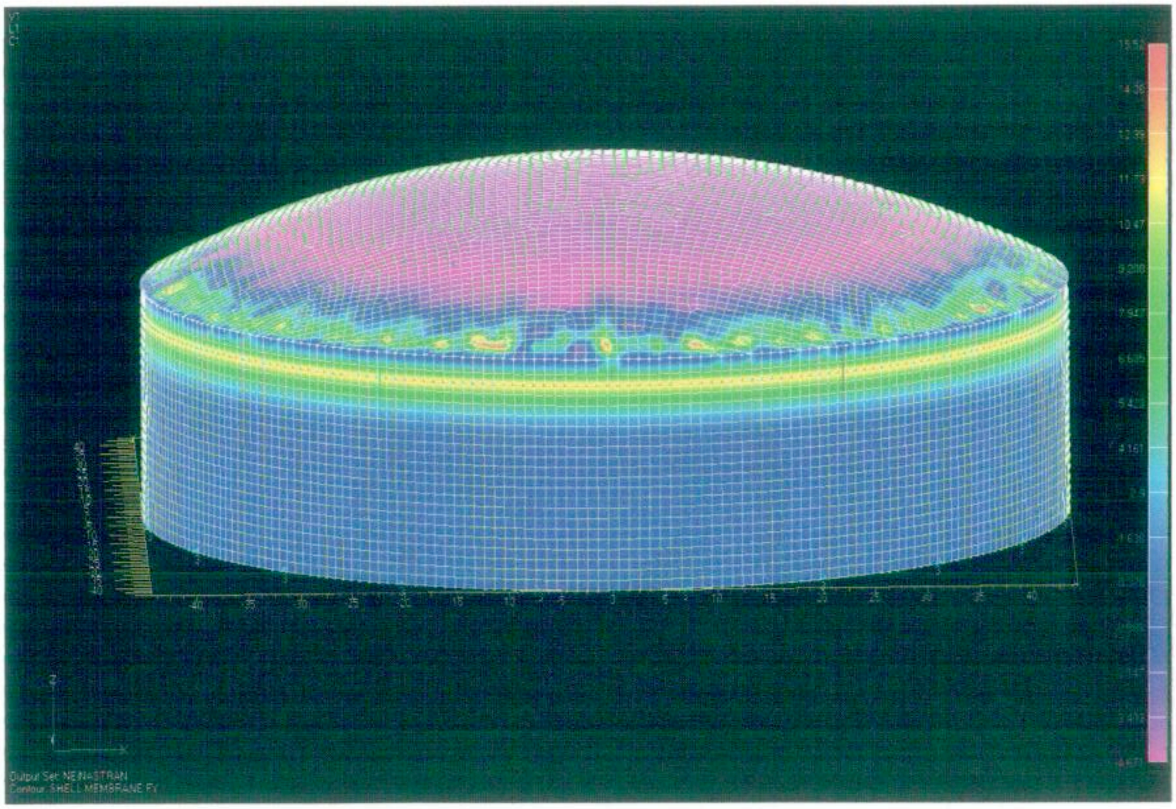

Figure 8-5—Meridional Force Distribution in Water Tank.

Figure 8-6 shows the FEA distribution of the moment in the water tank. The value of the moment in the dome at the junction of the dome at the ring was found to be -1.031 k-ft/ft. The moment at the junction of the ring and wall was -0.54 k-ft/ft.

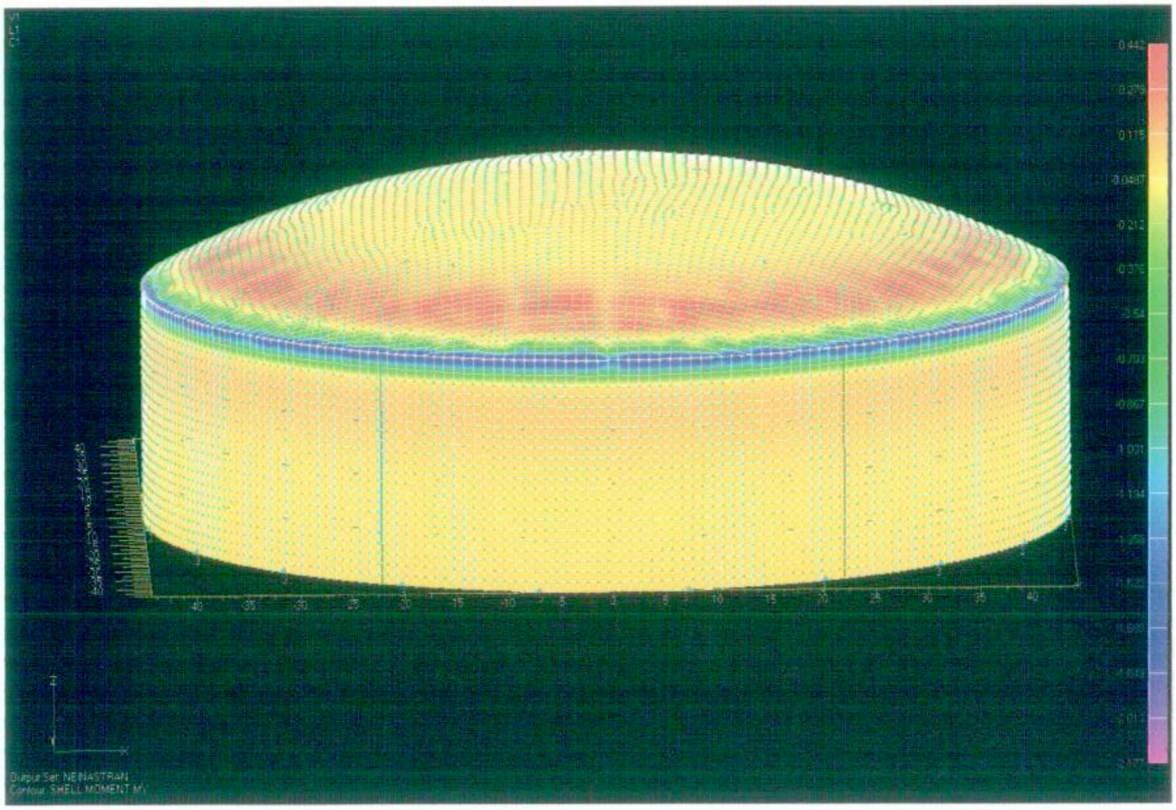

Figure 8-6—Distribution of Moment in Water Tank.

Table 8-1 shows the comparison of the FEA solution values and the dome-ring analysis values from Billington.

Table 8-1—Comparison of Forces and Moments Between Dome-Ring Solution and FEA.

	Dome-Ring Solution	Nastran FEA
Dome Hoop Force	26.81 k/ft	25.2 k/ft
Ring Hoop Force	3.00 k/ft	2.797 k/ft
Dome Meridional Force	-2.88 k/ft	-2.147 k/ft
Ring Meridional Force	4.50 k/ft	4.161 k/ft
Dome Moment	-0.78 k-ft/ft	-1.031 k-ft/ft
Ring Moment	-0.68 k-ft/ft	-0.54 k-ft/ft

Billington also compared this problem to a finite element analysis solution. He concluded on page 179,

> "The main conclusion from this study is that the approximate solution provides a reasonable basis for design even though the more rigorous solution does give somewhat different results. Where the finite-element program is readily available, it can be used as a basis for design, but it is always important to study such results carefully in the light of more approximate solutions."

Chapter 9

BUCKLING ANALYSIS OF TRUNCATED MONOLITHIC DOME USING FINITE ELEMENT ANALYSIS

A real-life example of considerably more complexity is considered next. Birmingham, Alabama is home to the largest diameter Monolithic Dome in the world (see Figure 9-1). Faith Chapel Christian Center measures 280-feet in diameter with a seating capacity of approximately 3,000. The dome encloses 61,575 square feet. Architect Rick Crandall designed the church. Dome Technology of Idaho Falls, Idaho built the dome shell.

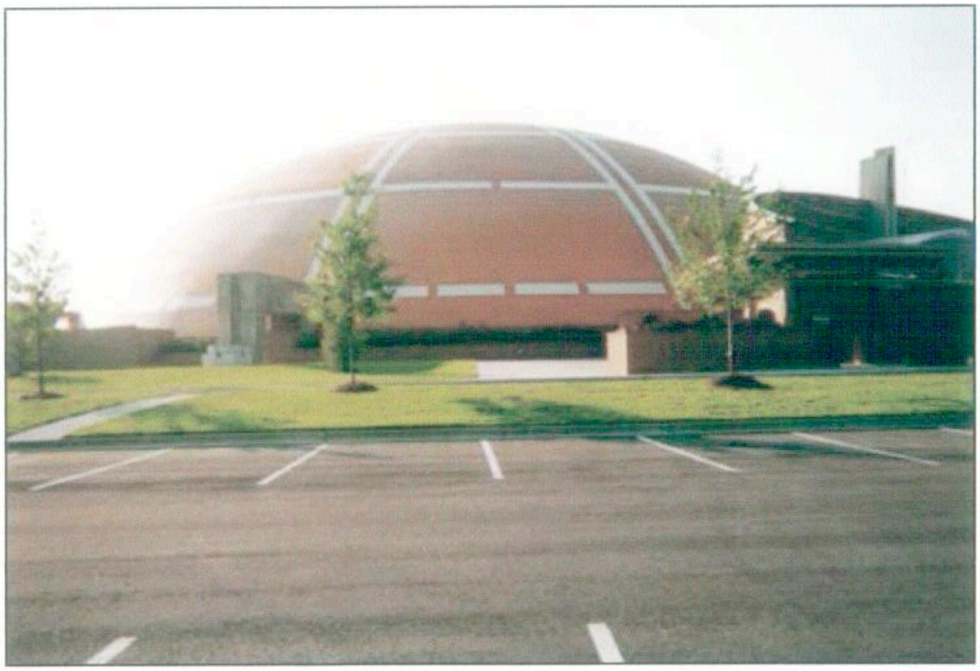

Figure 9-1—Faith Chapel Christian Center (24).

Jesse Harris and Lee Gray of LPDJ Arichitects, LLC. are working steadily on the expansion plans for Faith Chapel. The expansion will add on to the existing church and will cover 130,000 square feet on a 16 acre portion of the 140 acre site (see Figure 9-2).

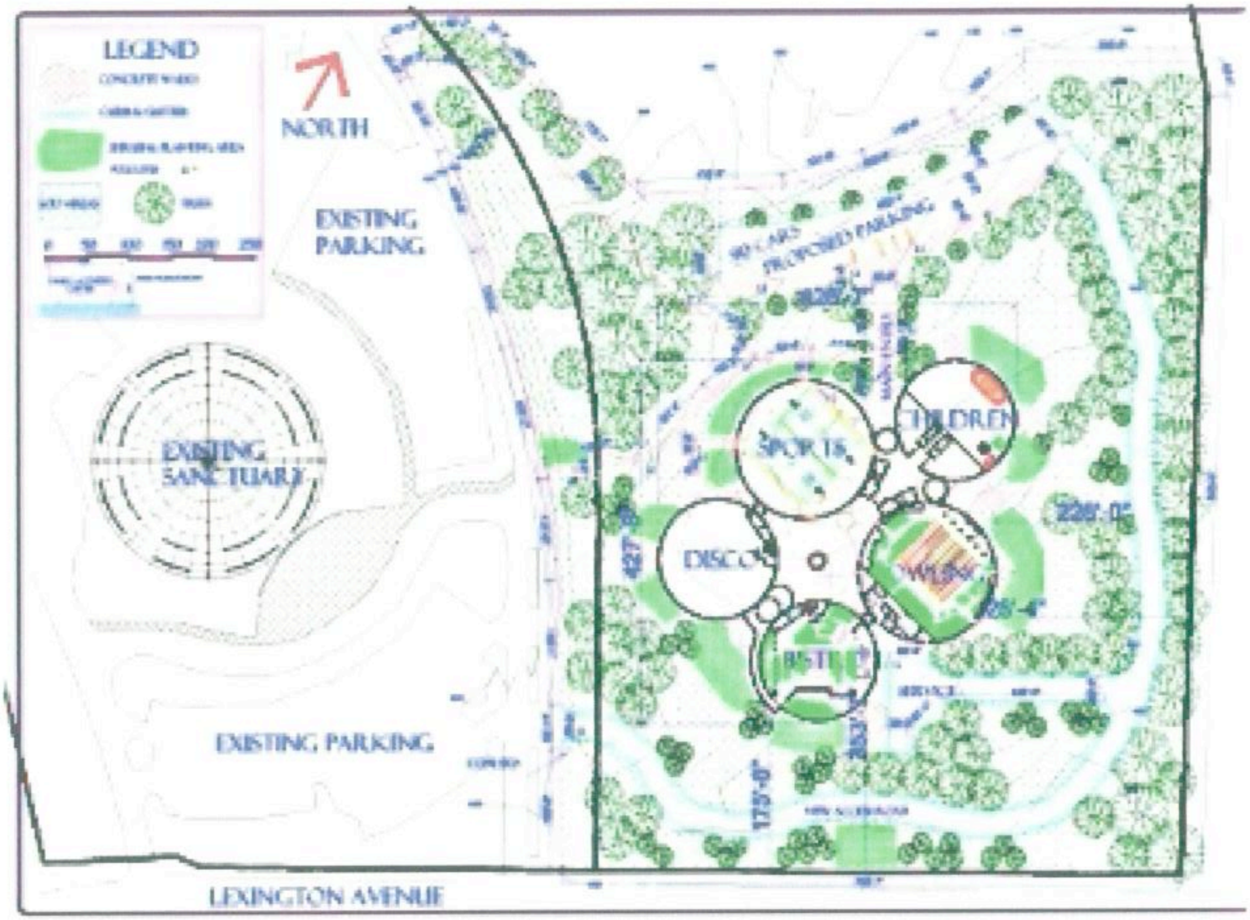

Figure 9-2—Layout of the Planned Expansion for Faith Chapel Showing Existing Structure on the Left (25).

Atop one of the domes in the planned expansion is a plexiglass tower over a 12 ft. diameter skylight (shown in Figure 9-3).

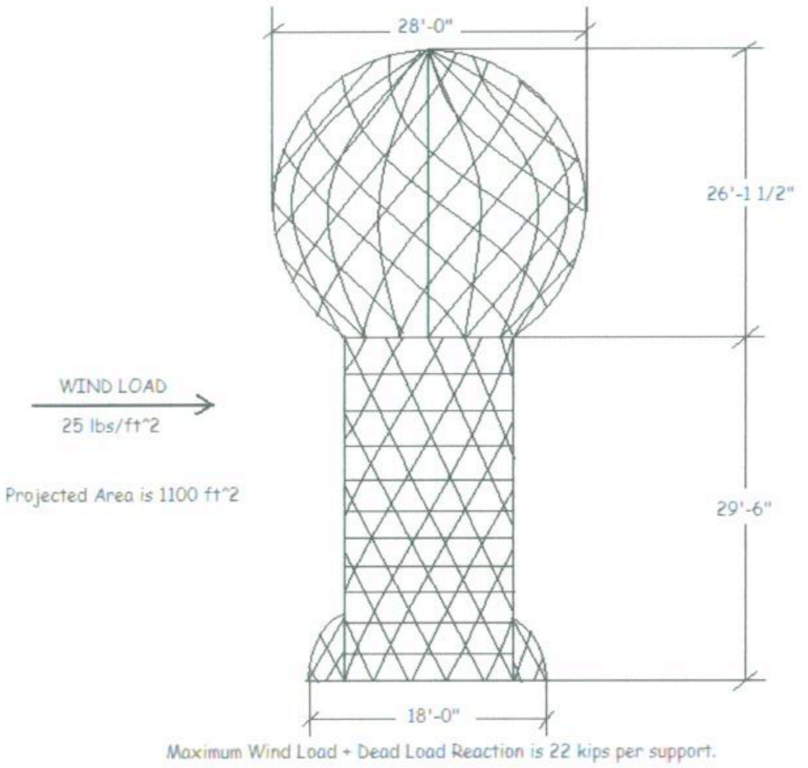

Figure 9-3—Plexiglass Tower Spanning 12 ft. Diameter Skylight at Apex of Dome.

A buckling analysis was performed to aid in the design of a thickened ring around the skylight to support the loads caused by the overturning moment. The design goal was to attain a factor of safety of at least 3, preferably higher, since the dome is in an area that can have hurricane force winds. The largest force given by the manufacturers of the tower due to the overturning moment would be at least 22 kips x 3.0 = 66 kips.

The approximate location of the centroid of the tower is:

$[(14')(29.5')(14.75') + (\pi)(14')^2(42.5')]/[(14')(29.5')+(\pi)(14')^2] = 31.35$ ft.

Using the given area of 1100 ft^2 and given loads the overturning moment can be found.

$M_{ot} = (25\ lb/ft^2)(1100\ ft^2)(31.35\ ft) = 862$ kips-ft.

The load is applied on an 18′-0" diameter circle at 30° increments. The moment of inertia for the circle and area are:

$$I = 0.049087[(18)^4-(17.5)^4] = 549.1332 \text{ ft}^4$$

$$A = \pi(9)^2 - \pi\,(8.75)^2 = 13.94 \text{ ft}^2$$

And,

$$A/12 = 1.1617 \text{ ft}^2$$

Taking 1100 ft^2 for the tower and multiplying it by 25 psf for the wind load, 27.5 kips is obtained. Multiply 27.5 kips and 31.35 ft to get a moment of 862.125 kips-ft. Then, solving for the reactions in terms of moments 862.125 kips-ft is divided by 46.57 to get 18.5 kips, which represents the axial load from the tower. Subtracting 18.5 kips from the given 22 kips it is found that the design axial load is 3.5 kips per location.

Using MC/I, the bending stress can be found at the location of each point of loading:

For c = 9 ft. $MC/I = [(862 \text{ k-ft})(9 \text{ ft})]/549.1332 \text{ ft}^4 = 14.1277$ ksf

For c = 7.714 ft. $MC/I = [(862 \text{ k-ft})(7.714 \text{ ft})]/549.1332 \text{ ft}^4 = 12.10$ ksf

For c = 4.5 ft. $MC/I = [(862 \text{ k-ft})(4.5 \text{ ft})]/549.1332 \text{ ft}^4 = 7.06$ ksf

Thus, for c = 9 ft: (14.1277 ksf)(1.1617 ft^2) = 16.41 kips; c = 7.714 ft: (12.10 ksf)(1.1617 ft^2) = 14.06 kips; c = 4.5 ft: (7.06 ksf)(1.1617 ft^2) = 8.2 kips.

The points of application of the forces are shown in Figure 9-4 below.

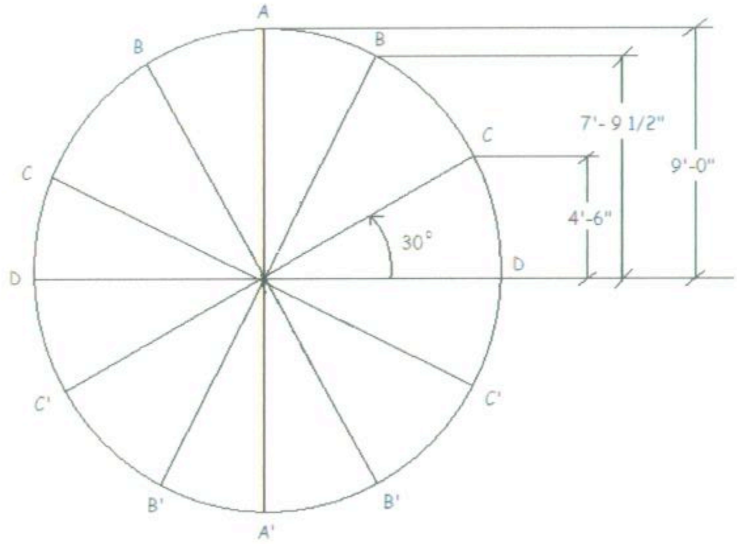

Figure 9-4—Load Application Points on 18 ft. Diameter Circle around 12 ft. Diameter Skylight.

The total point loads at each location are listed below:

At A: 3.5 kips + 16.41 kips = 19.91 kips

At B: 3.5 kips + 14.06 kips = 17.56 kips

At C: 3.5 kips + 8.2 kips= 11.7 kips

At D: 3.5 kips

At A′: 3.5 kips – 16.41 kips = -12.91 kips

At B′: 3.5 kips – 14.06 kips = -10.56 kips

At C′: 3.5 kips – 8.2 kips = -4.7 kips

For the buckling analysis in NE/Nastran, these point loads must be scaled to represent a unit load. After scaling the point loads at each location to a unit load equivalent by dividing each individual load by the sum of the loads, the resulting point loads are:

At A: 0.474kips

At B: 0.418 kips

At C: 0.279 kips

At D: 0.0833kips

At A′: -0.307 kips

At B′: -0.251 kips

At C′: -0.112 kips

The material properties used in this project are as follows: for f'c = 4,000 psi concrete, E = 519120 ksf; mass density = .00466 kips/ft^3; ν = 0.17; and thickness = 6 in. or 0.5 ft. The dome radius is 101.5 ft, with a skylight cut out at the apex with a diameter of 12 ft. The loads are applied on a circle of diameter 18 ft. A thickened ring with a 20 ft diameter is at the top of the dome to support the loads from the overturning moment. The ring is 14 in. thick.

In NASTRAN, the geometry for a 101.5 ft radius hemispherical dome was generated using the parasolid modeling engine. Material properties were entered as above. To include the self-weight of the dome acceleration downward, due to gravity, of 32.2 ft/s^2 was entered.

The shell element used in meshing the dome is called CQUADR, CTRIAR. This type of shell element is preferred for curved structures as it has a complete six degrees of freedom per node element. A rough mesh was applied for initial comparison and then refined. The bottom edge of the dome was fixed since the primary concern was the top of the dome.

The buckling analysis is well explained in the NE/Nastran and Modeler Tutorial. The goal of this analysis was to use NE/Nastran to predict the critical load that causes the top of the dome to buckle. In a typical buckling analysis, a unit load is applied to the model. Nastran then calculates the smallest eigenvalue, λ, that, when multiplied by the unit load, gives the critical load that causes the buckling. In this case the unit load is a series of point loads around the 18 ft. diameter circle. To accomplish this, Nastran calculates the resulting stresses from the application of these loads and then the eigenvalue and buckling mode shapes. This is the stress caused by a 1 kip load. The eigenvalue returned by NE/Nastran multiplied by the unit load gives the critical buckling load.

The lowest eigenvalue associated with buckling in the top of the dome was found to be 140.14960 as shown in Figure 9-5. The buckling modes previous to this value were not the concern of this study as they occurred at the edge of the dome.

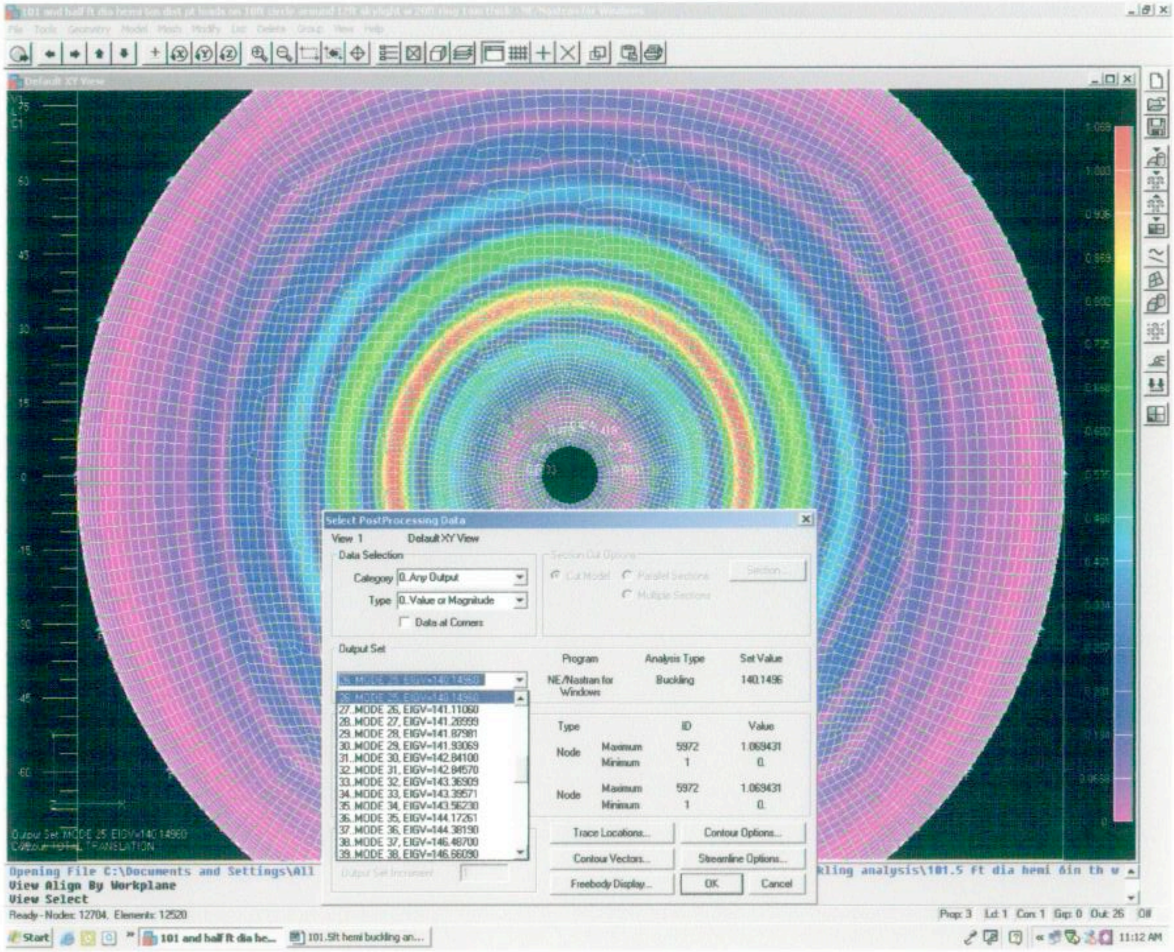
Select PostProcessing Data

View 1 Default XY View

Data Selection

Category 0..Any Output

Type 0..Value or Magnitude

☐ Data at Corners

Output Set

26..MODE 25, EIGV=140.14960

Program	Analysis Type	Set Value
NE/Nastran for Windows	Buckling	140.1496

27..MODE 26, EIGV=141.11060
28..MODE 27, EIGV=141.28999
29..MODE 28, EIGV=141.87981
30..MODE 29, EIGV=141.93069
31..MODE 30, EIGV=142.84100
32..MODE 31, EIGV=142.84570
33..MODE 32, EIGV=143.36909
34..MODE 33, EIGV=143.39571
35..MODE 34, EIGV=143.56230
36..MODE 35, EIGV=144.17261
37..MODE 36, EIGV=144.38190
38..MODE 37, EIGV=146.48700
39..MODE 38, EIGV=146.66090

Type		ID	Value
Node	Maximum	5972	1.069431
	Minimum	1	0.
Node	Maximum	5972	1.069431
	Minimum	1	0.

```
Opening File C:\Documents and Settings\All
View Align By Workplane
View Select
```

Ready - Nodes: 12704, Elements: 12520

Figure 9-5—Controlling Eigenvalue, λ = 140.14960, for Buckling Analysis.

A closer look at the controlling buckling mode shape is given in Figure 9-6.

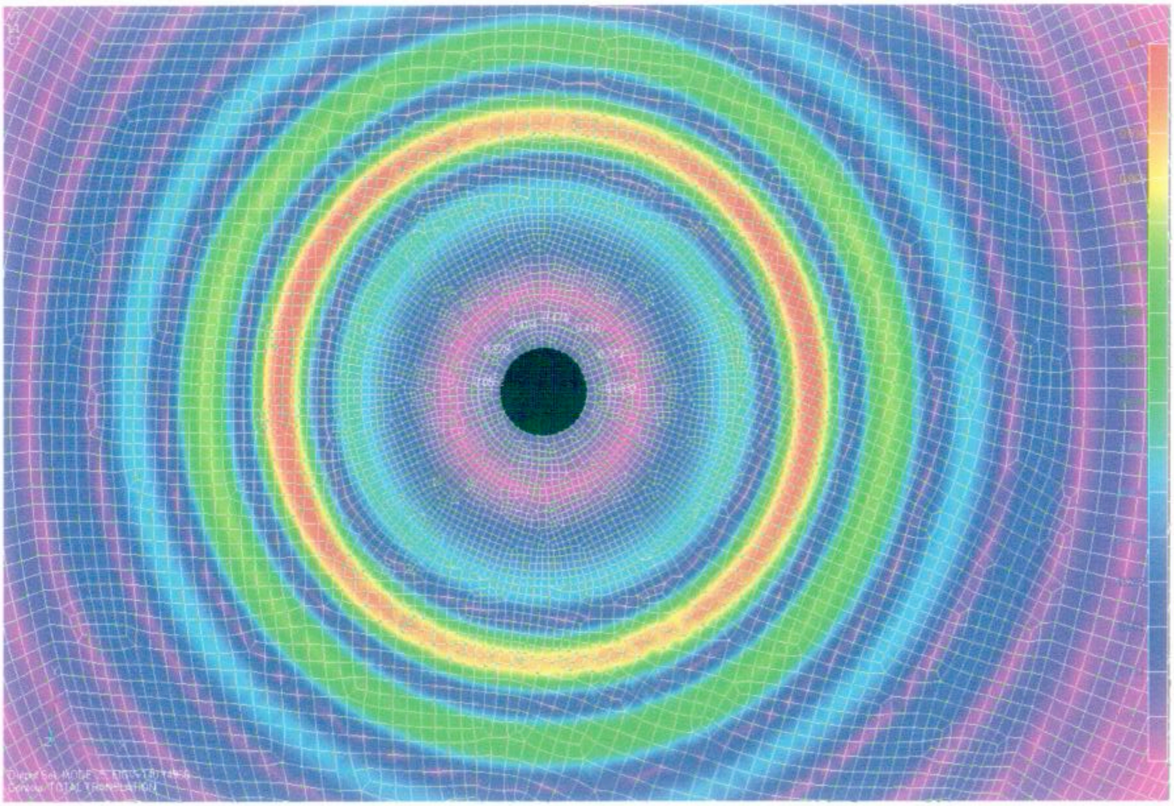

Figure 9-6—Controlling Buckling Mode Shape Associated with λ = 140.14960.

The critical buckling load is computed by multiplying the maximum applied load, 0.474kips, by the eigenvalue returned from Nastran. This indicates that the top of the dome buckles when the maximum point load applied is 66.431kips. Thus, the factor of safety is 66.421kips / 22kips = 3.02.

This model yielded the desired factor of safety, yet it was decided to try a ribbed model that was less thick at the top of the dome to reduce the weight. The dome radius is the same at 101.5 ft, with a skylight cut out at the apex with a diameter of 12 ft. The loads are applied again on a circle of diameter 18 ft. A thickened ring two feet in width and one foot in depth is at the top of the dome with the curve of loading located in the center of the beam. Radiating off of the ring beam at the top of the dome are 1′ x 1′ ribs that are 20 ft. long (see Figure 9-7).

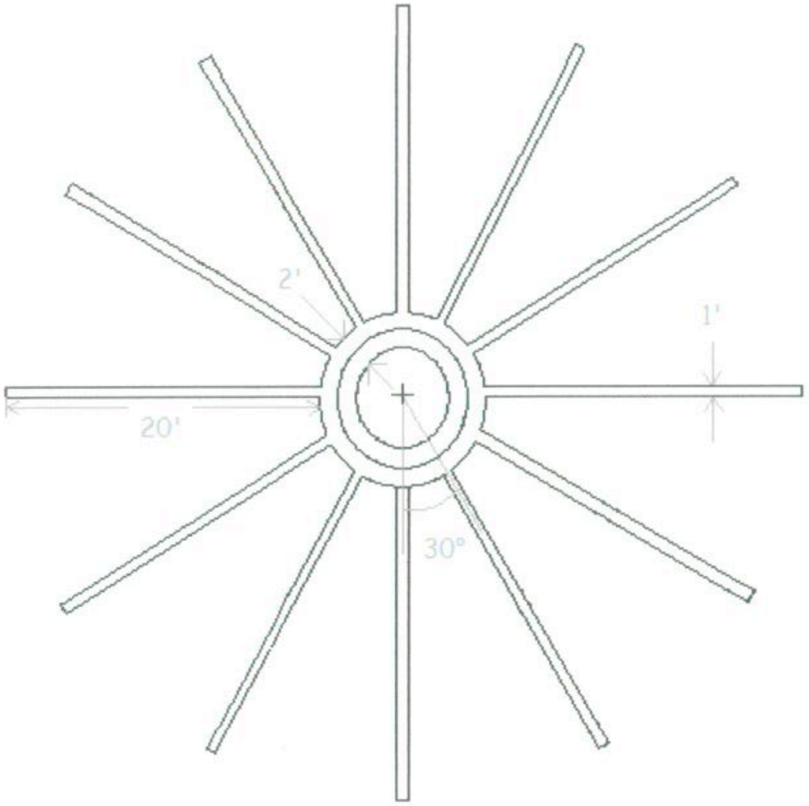

Figure 9-7--101.5 ft. diameter hemisphere with 1′ x 1′ ribs 20′ long at 30° off 2′ x 1′ ring at top of dome around 12′ diameter skylight.

The ribbed model built in Nastran had a shell thickness of 4 in. with material properties as before. Buckling mode 40 for 101.5 ft. diameter hemisphere was the controlling mode for the apex of the dome with a controlling eigenvalue of: λ_{40} = 97.916557 (see Figure 9-8). This indicates that the top of the dome buckles when the maximum point load applied is 46.41 kips. Thus, the factor of safety is 46.41 kips / 22 kips = 2.11.

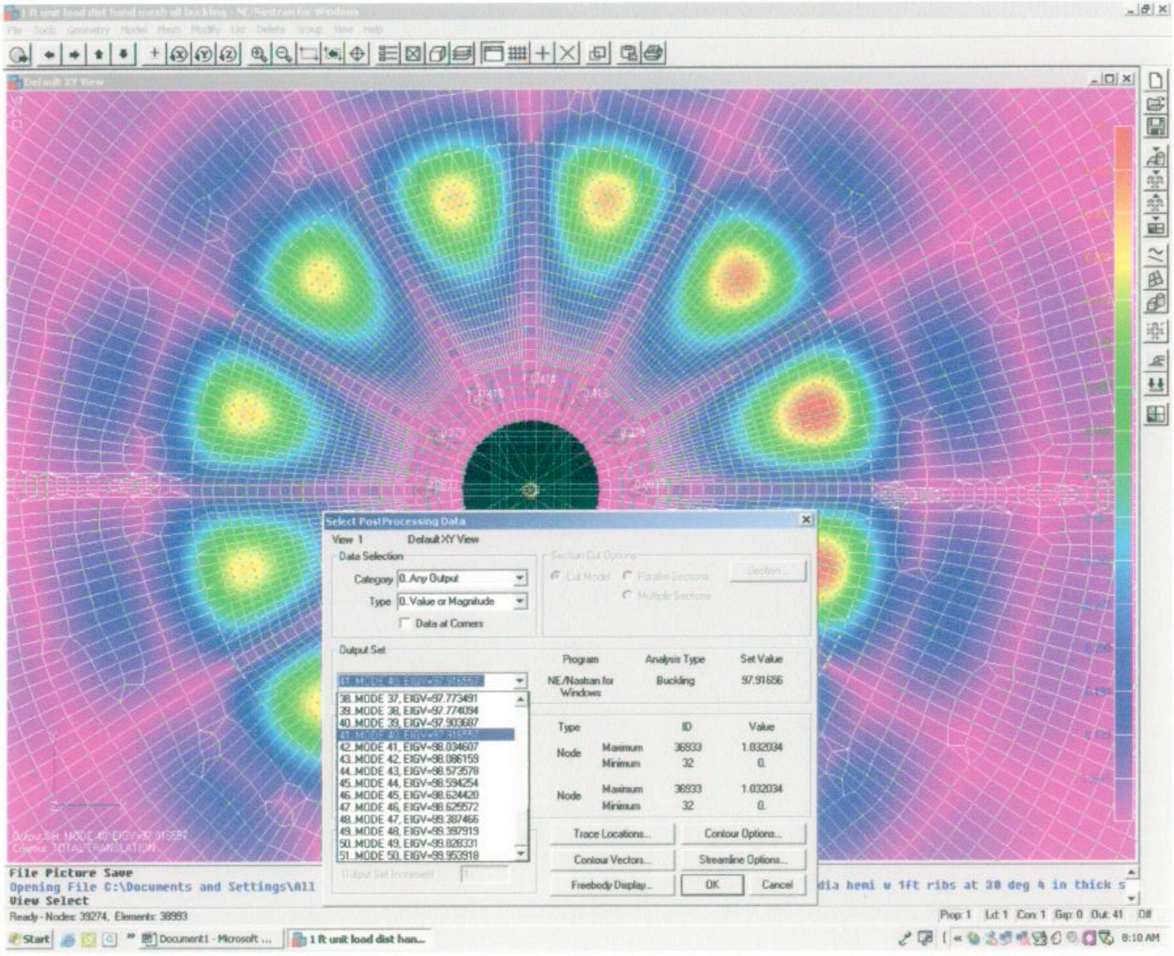

View 1 Default XY View

Data Selection

Category: 0..Any Output

Type: 0..Value or Magnitude

☐ Data at Corners

Output Set

Program	Analysis Type	Set Value
NE/Nastran for Windows	Buckling	97.91656

```
38..MODE 37, EIGV=97.773491
39..MODE 38, EIGV=97.774094
40..MODE 39, EIGV=97.903687
41..MODE 40, EIGV=97.916557
42..MODE 41, EIGV=98.034607
43..MODE 42, EIGV=98.086159
44..MODE 43, EIGV=98.573578
45..MODE 44, EIGV=98.594254
46..MODE 45, EIGV=98.624420
47..MODE 46, EIGV=98.625572
48..MODE 47, EIGV=99.387466
49..MODE 48, EIGV=99.387919
50..MODE 49, EIGV=99.828331
51..MODE 50, EIGV=99.953918
```

Type		ID	Value
Node	Maximum	36933	1.032034
	Minimum	32	0.
Node	Maximum	36933	1.032034
	Minimum	32	0.

```
File Picture Save
Opening File C:\Documents and Settings\All ... dia hemi w 1ft ribs at 30 deg 4 in thick s
View Select
```

Ready - Nodes: 39274, Elements: 38993

Prop: 1 Ld: 1 Con: 1 Grp: 0 Out: 41

Figure 9-8—Controlling Buckling Eigenvalue $\lambda_{40} = 97.916557$ for 101.5 ft. diameter hemisphere with 1′ x 1′ ribs 20′ long at 30° off 2′ x 1′ ring at top of dome around 12′ diameter skylight. Shell thickness = 4in.

A closer look at the controlling buckling mode shape is given in Figure 9-9.

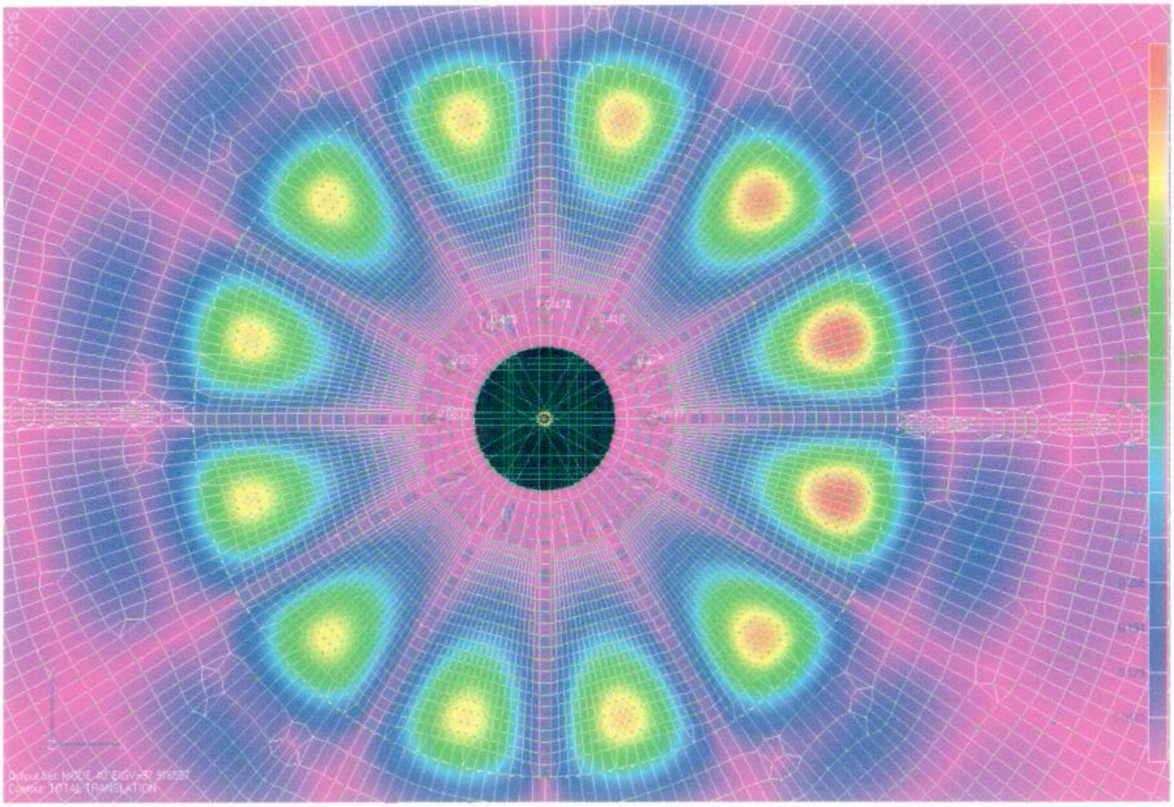

Figure 9-9—Controlling Buckling Mode Shape Associated with $\lambda_{40} = 97.916557$.

The factor of safety of 2.11 is not sufficient so a second model was analyzed with a shell thickness of 5 in. Buckling mode 49 for the apex of the 101.5 ft. diameter hemisphere was the controlling mode with a controlling eigenvalue of: $\lambda_{49} = 129$ (see Figure 9-10). This indicates that the top of the dome buckles when the maximum point load applied is 61.15 kips. Thus, the factor of safety is 61.15 kips / 22 kips = 2.78.

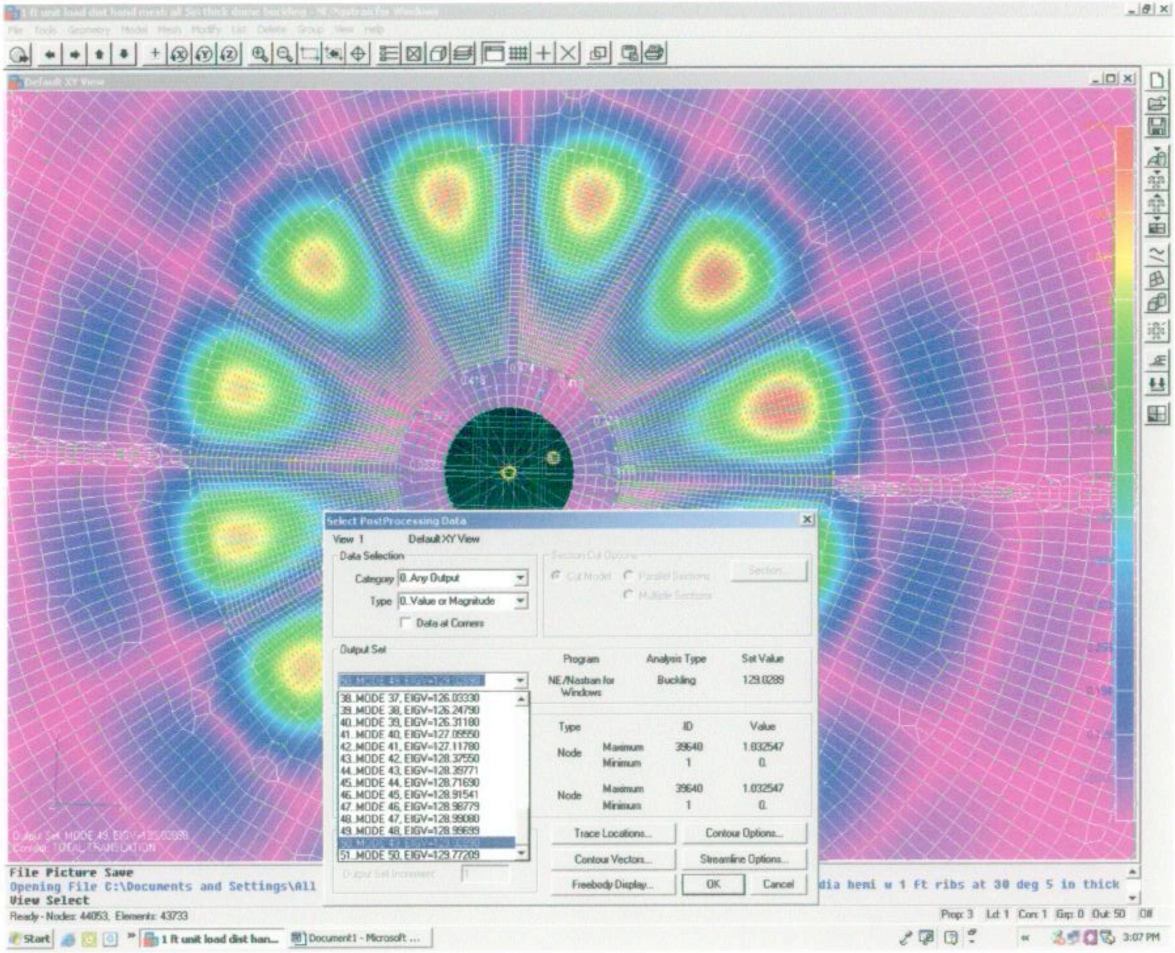

View 1 Default XY View

Data Selection

Category 0..Any Output

Type 0..Value or Magnitude

☐ Data at Corners

Output Set

```
38..MODE 37, EIGV=126.03330
39..MODE 38, EIGV=126.24790
40..MODE 39, EIGV=126.31180
41..MODE 40, EIGV=127.09550
42..MODE 41, EIGV=127.11780
43..MODE 42, EIGV=128.37550
44..MODE 43, EIGV=128.39771
45..MODE 44, EIGV=128.71690
46..MODE 45, EIGV=128.91541
47..MODE 46, EIGV=128.98779
48..MODE 47, EIGV=128.99080
49..MODE 48, EIGV=128.99699
51..MODE 50, EIGV=129.77209
```

Program	Analysis Type	Set Value
NE/Nastran for Windows	Buckling	129.0288

Type		ID	Value
Node	Maximum	39640	1.032547
	Minimum	1	0.
Node	Maximum	39640	1.032547
	Minimum	1	0.

```
File Picture Save
Opening File C:\Documents and Settings\All ... dia hemi w 1 ft ribs at 30 deg 5 in thick
View Select
```

Ready - Nodes: 44053, Elements: 43733

Prop: 3 Ld: 1 Con: 1 Grp: 0 Out: 50

Figure 9-10--Controlling Buckling Eigenvalue $\lambda_{49} = 129.$ for 101.5 ft. diameter hemisphere with 1′ x 1′ ribs 20′ long at 30° off 2′ x 1′ ring at top of dome around 12′ diameter skylight. Shell thickness = 5 in.

A closer look at the controlling buckling mode shape is given in Figure 9-11.

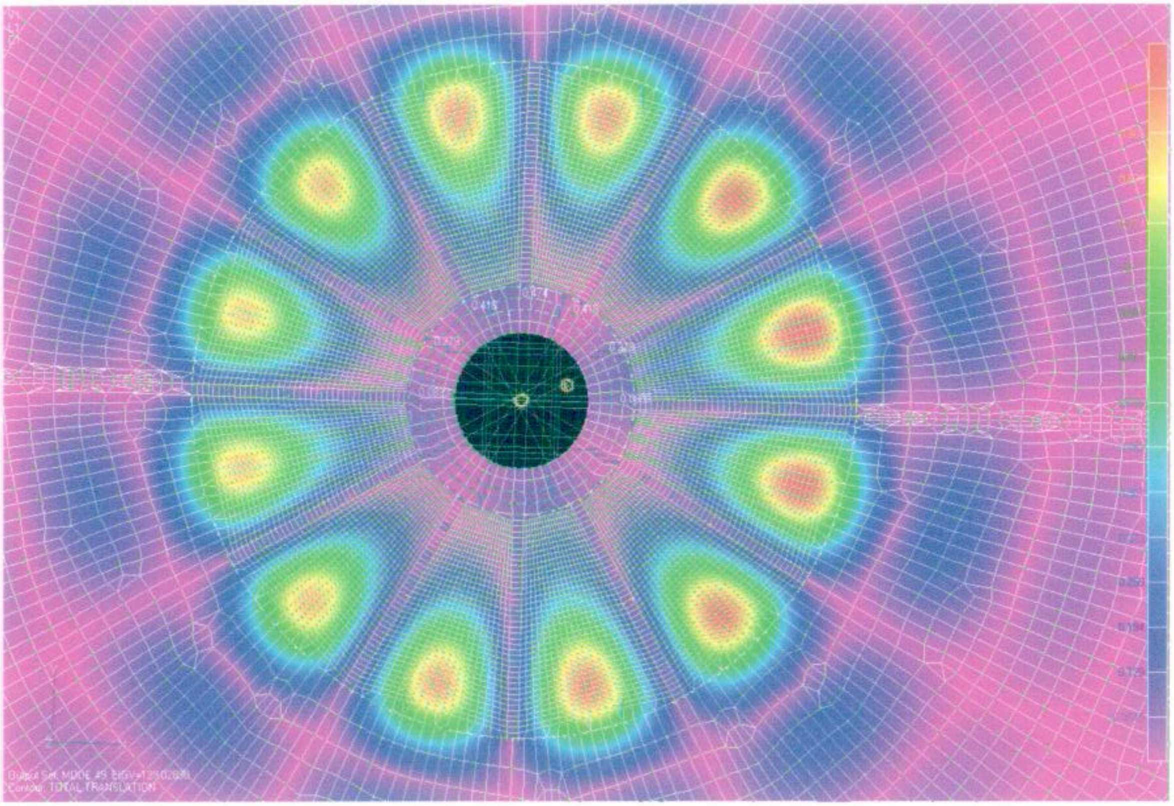

Figure 9-11—Controlling Buckling Mode Shape Associated with $\lambda_{49} = 129$.

The factor of safety of 2.78 is still too small. A modification of the same configuration at the top of the dome is analyzed to prevent increasing the shell thickness yet again. The dome radius is the same at 101.5 ft, with a skylight cut out at the apex with a diameter of 12 ft. The loads are applied again on a circle of diameter 18 ft. A thickened ring two feet in width and one foot in depth is at the top of the dome with the curve of loading located in the center of the beam. Radiating off of the ring beam at the top of the dome are the 1′ x 1′ ribs that are 20 ft. long. Added are two transverse 1′ x 1′ ribs that are located at 10 ft., and 20 ft., from the edge of the ring (see Figure 9-12).

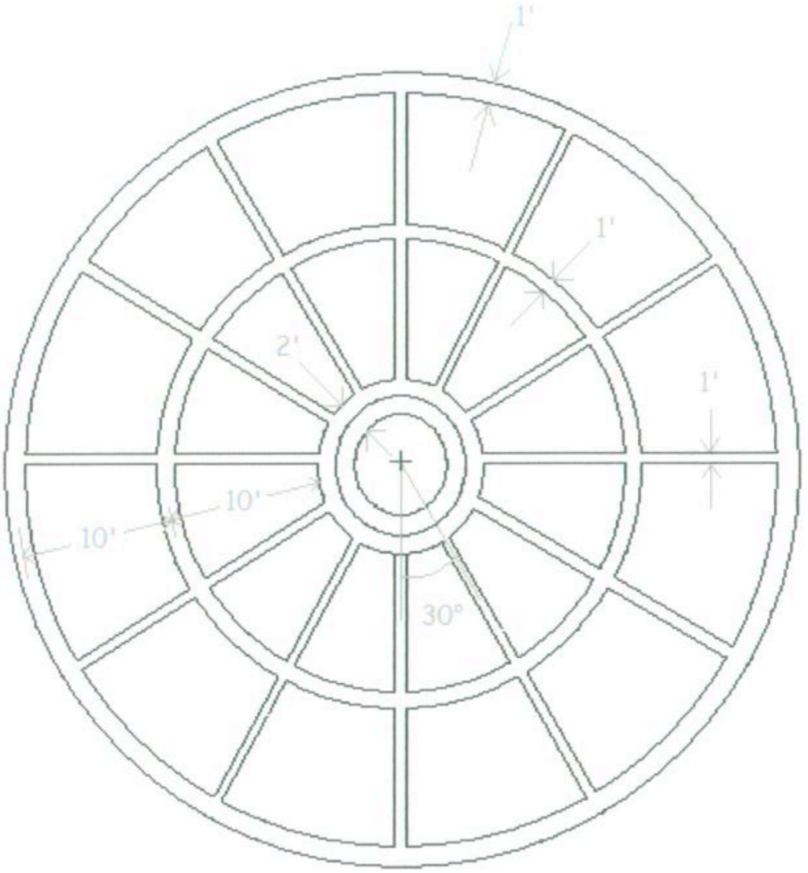

Figure 9-12—Ring Beam, Radial Ribs, and Transverse Ribs around Skylight Opening.

The ribbed model built in Nastran has a shell thickness of 5 in. with material properties as before. The controlling buckling mode yields an eigenvalue of: $\lambda = 141$ (see Figure 9-13). This indicates that the top of the dome buckles when the maximum point load applied is 66.834 kips. Thus, the factor of safety is 66.834 kips / 22 kips = 3.04.

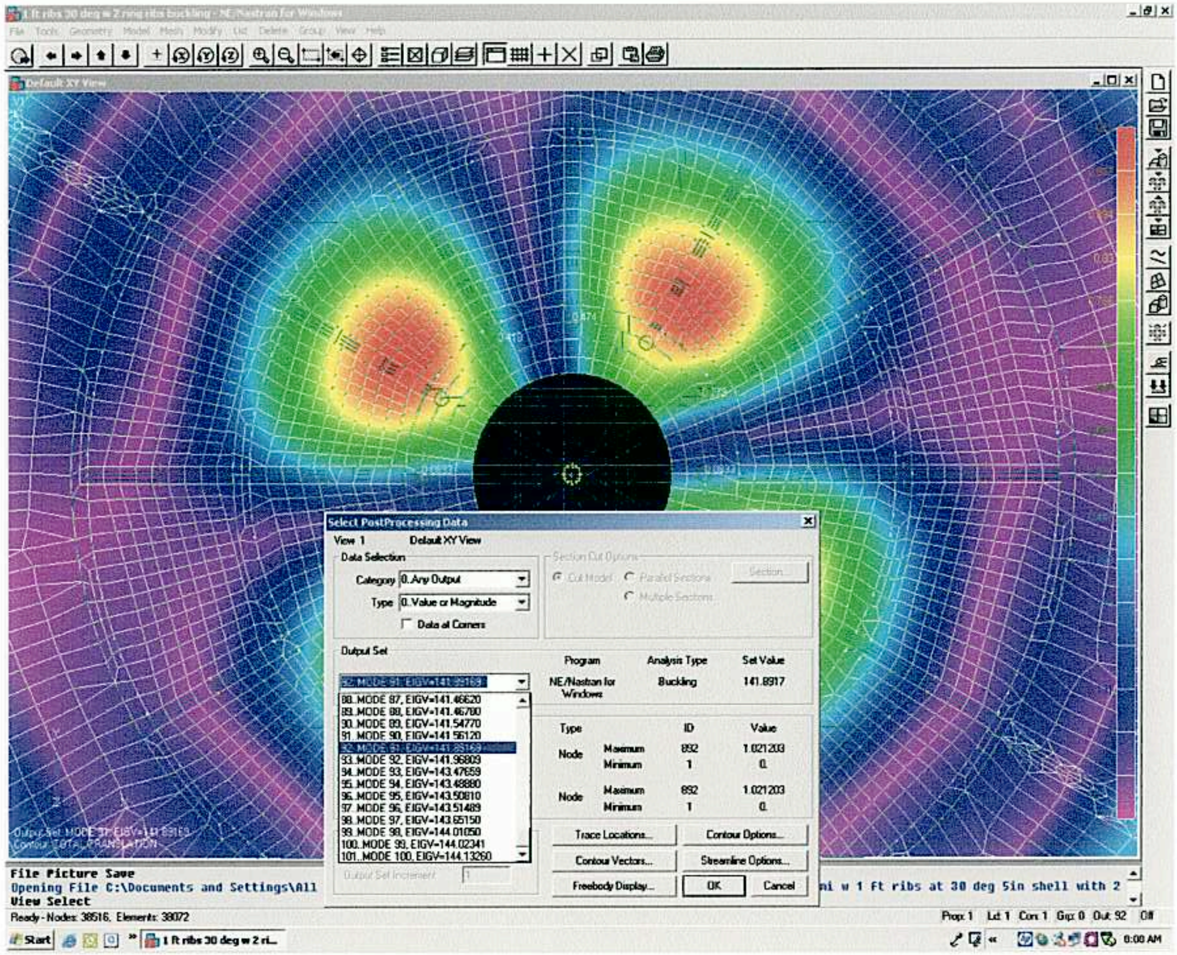

Select PostProcessing Data

View 1 Default XY View

Data Selection

Category: 0..Any Output

Type: 0..Value or Magnitude

☐ Data at Corners

Output Set: 92..MODE 91, EIGV=141.89169

88..MODE 87, EIGV=141.46620
89..MODE 88, EIGV=141.46780
90..MODE 89, EIGV=141.54770
91..MODE 90, EIGV=141.56120
92..MODE 91, EIGV=141.89169
93..MODE 92, EIGV=141.96809
94..MODE 93, EIGV=143.47659
95..MODE 94, EIGV=143.48880
96..MODE 95, EIGV=143.50810
97..MODE 96, EIGV=143.51489
98..MODE 97, EIGV=143.65150
99..MODE 98, EIGV=144.01050
100..MODE 99, EIGV=144.02341
101..MODE 100, EIGV=144.13260

Program	Analysis Type	Set Value
NE/Nastran for Windows	Buckling	141.8917

Type		ID	Value
Node	Maximum	892	1.021203
	Minimum	1	0.
Node	Maximum	892	1.021203
	Minimum	1	0.

```
File Picture Save
Opening File C:\Documents and Settings\All ... ni w 1 ft ribs at 30 deg 5in shell with 2
View Select
```

Ready - Nodes: 38516, Elements: 38072

Prop: 1 Ld: 1 Con: 1 Grp: 0 Out: 92 Off

Figure 9-13--Controlling Buckling Eigenvalue λ = 141 for 101.5 ft. diameter hemisphere with 1′ x 1′ radial ribs 20′ long at 30° off 2′ x 1′ ring at top of dome around 12′ diameter skylight. Two 1′x1′ transverse ribs are located at 10′ and 20′ from ring beam. Shell thickness = 5in.

A closer look at the controlling buckling mode shape is given in Figure 9-14.

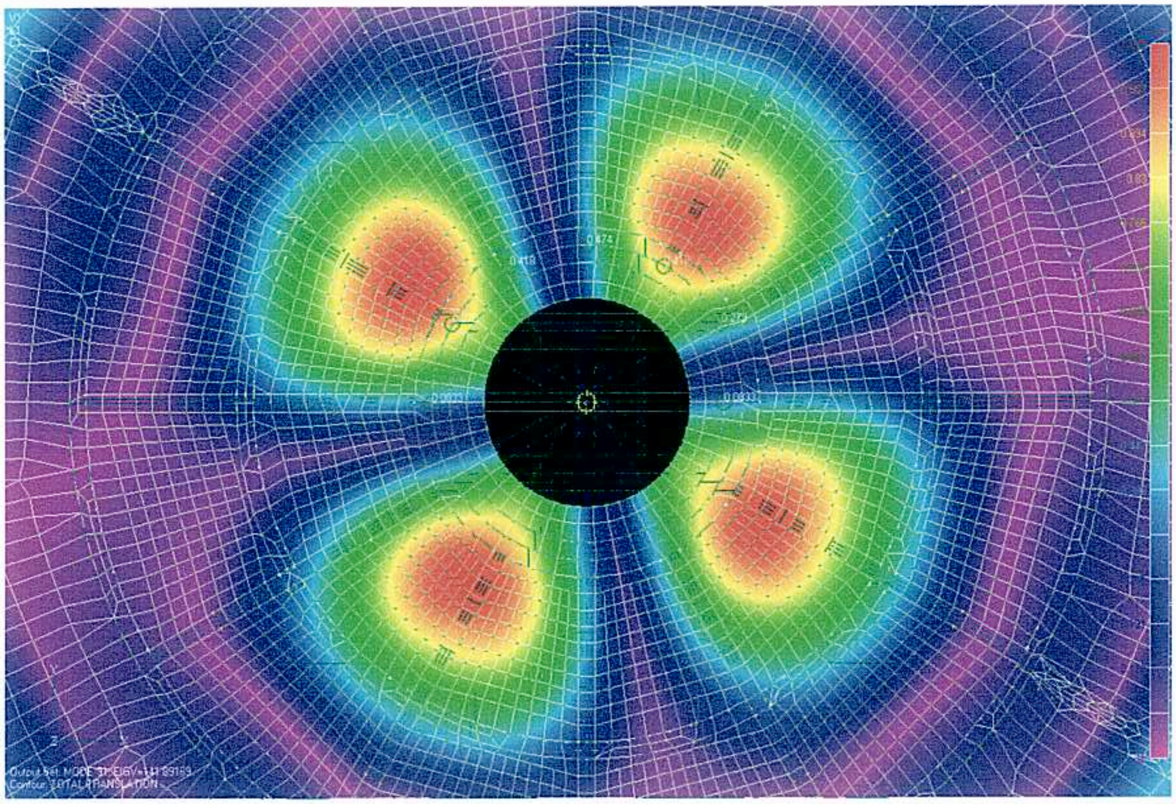

Figure 9-14-- Controlling Buckling Mode Shape Associated with λ = 141.

The factor of safety is satisfactory, so the hoop and meridional stresses are of interest and are shown in Figures 9-15 and 9-16, respectively. Mx and My distributions are similarly shown in Figures 9-17 and 9-18, respectively.

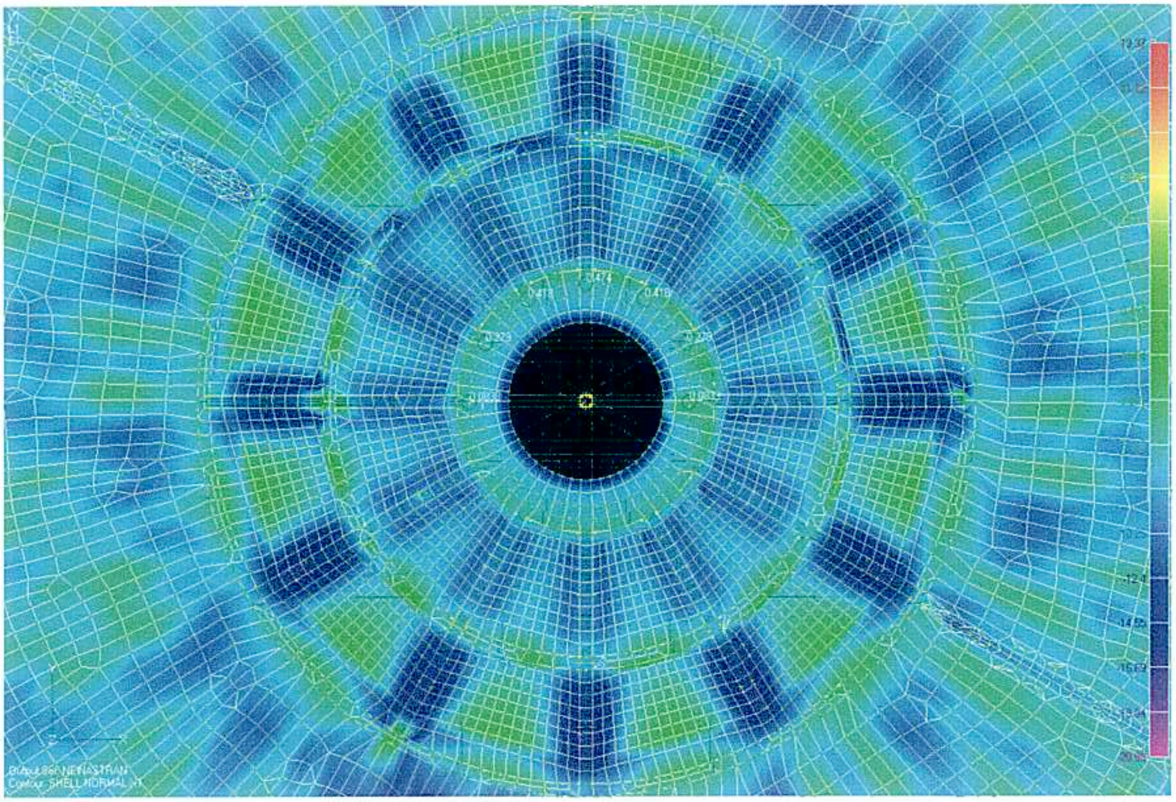

Figure 9-15--Hoop Stresses at the Top of Ribbed Dome. Maximum stress = -21 ksf.

Maximum stress at top of dome = -17 ksf.

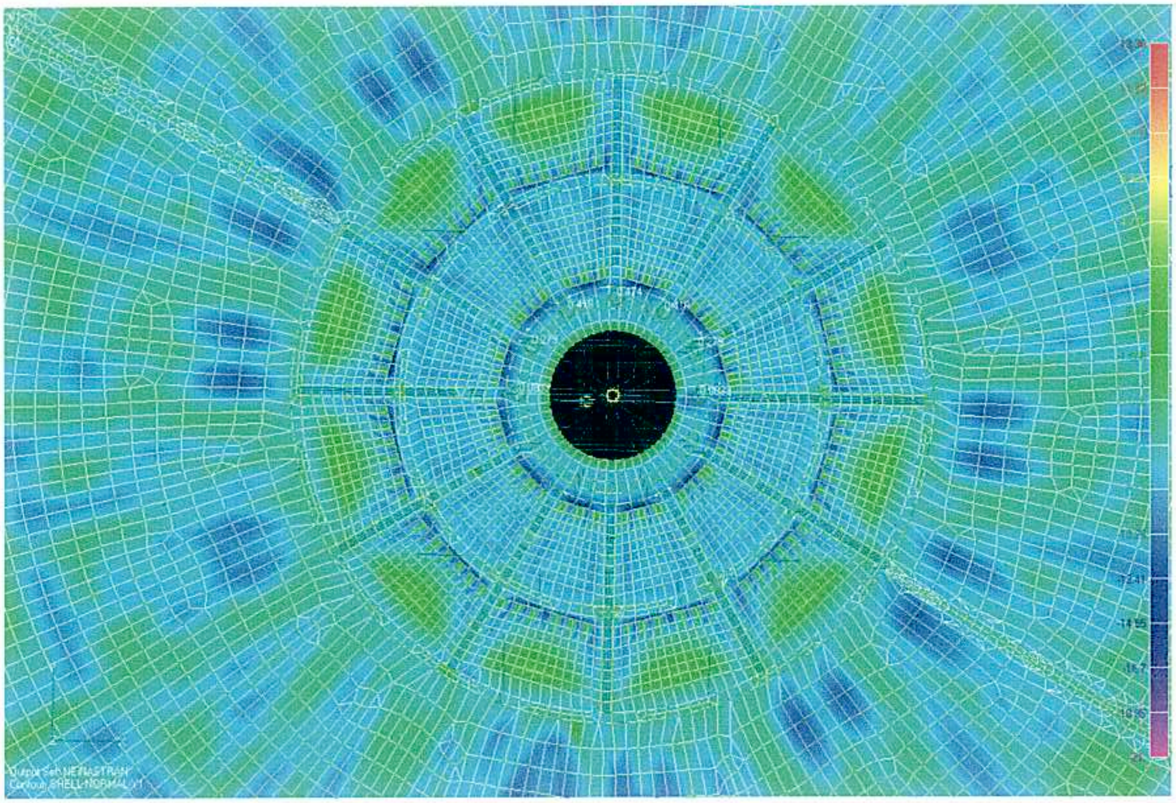

Figure 9-16--Meridional Stresses at the Top of Ribbed Dome. Maximum stress = -21 ksf. Maximum stress at top of dome = -17 ksf.

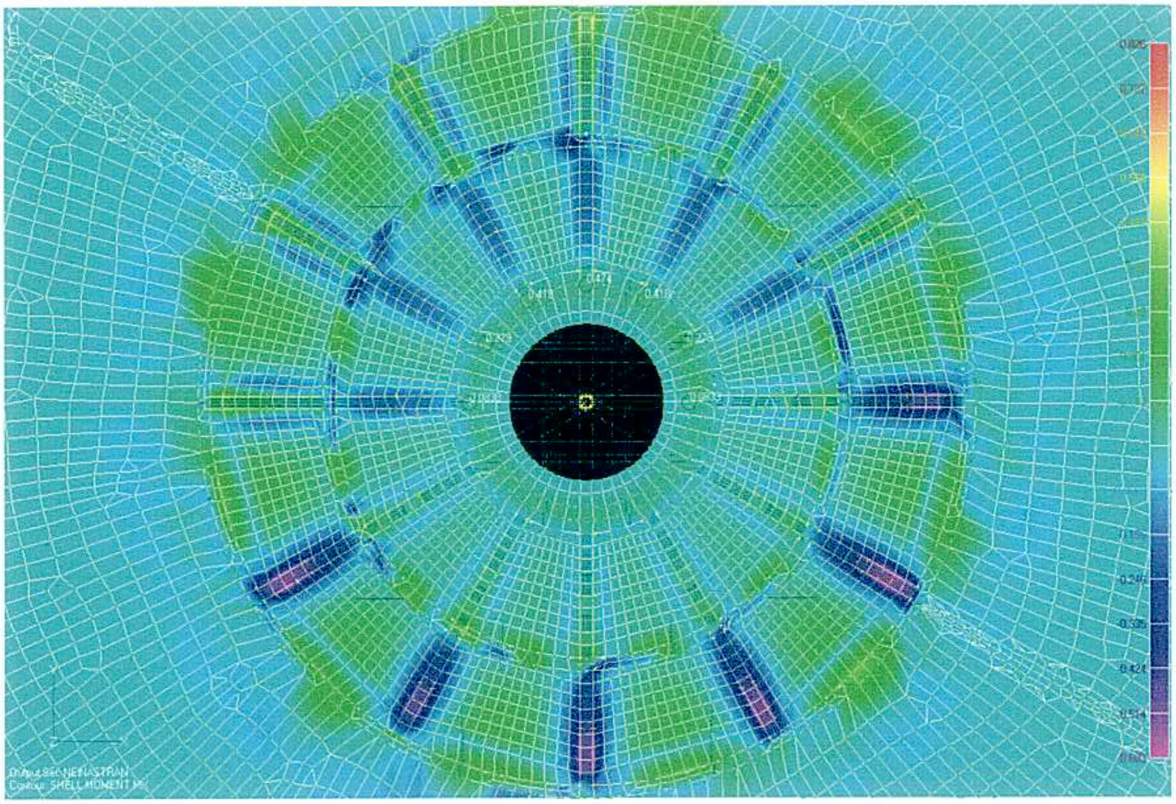

Figure 9-17--Mx = -0.603 kips-ft/ft at top of dome (purple).

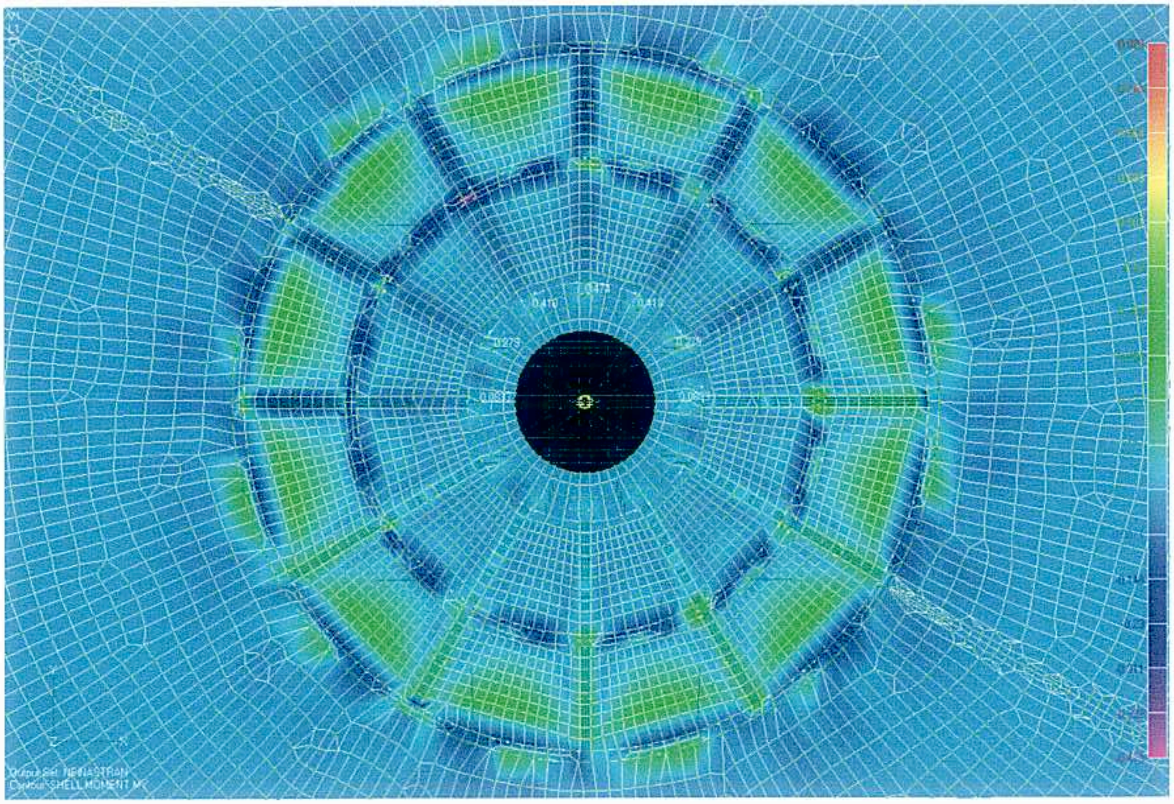

Figure 9-18--My = -0.4 kips-ft/ft at top of dome (blue).

This chapter illustrates the power of the finite element program. Once the initial model is verified by comparing the basic stress equations with the basic FEA results, powerful design conclusions can be drawn and complicated problems can be analyzed by employing the basic finite element analysis and other functions, such as the buckling analysis and dynamic analysis.

Chapter 10

CONCLUSIONS

Conclusions drawn from the study of shell theory, finite element analysis theory, and the comparisons between them are:

- The finite element model must be carefully made as very minor oversights or errors can possibly lead to extremely unreliable data. Compatibility of element boundaries must be verified and constraints must be applied precisely or large errors can result.

- Uniformly and symmetrically meshing the domain will provide well distributed force, moment, and stress resultants.

- Comparison of the results between shell theory and the finite element model indicate that finite element results are reliable and they can be used in analysis and design of these structures with confidence.

- Finite element modeling and analysis could be used for more complicated geometry and loadings where hand calculations are impossible or hard to perform.

REFERENCES

1. Eric M. Hines and David P. Billington, "Anton Tedesko and the Introduction of Thin Shells in the United States," June 9, 2003

2. "Case Histories," http://www.arche.psu.edu/thinshells/module%20I/case_studies.htm, 6/9/05

3. "Memorial Tributes," National Academy of Engineering, Volume 8 (1996), http://www.nap.edu/openbook/030905575X/html/R1.html , 3/24/05

4. Hershey Community Archives, Hershey History, Hershey Sports Arena, http://www.hersheyarchives.org/Default.aspx?Page=HersheyArena , 3/24/05

5. Sara Askari, "Pier Luigi Nervi," http://www.uwgb.edu/galta/333/nervi.htm, 9/7/05

6. Riccardo Cigola, "Art: Artists and Architects," http://www.italycyberguide.com/Art/artistsarchite/nervi.htm, 9/7/05

7. http://www.unpi.com/nervi.html, United Nations Philatelists, Inc., 9/7/05

8. "Felix Candela," http://www.greatbuildings.com/architects/Felix_Candela.html, 9/7/05

9. "Felix Candela," Encyclopedea Brittanica Online, http://www.britannica.com/eb/article?tocId=9019950, 9/7/05

10. "Felix Candela," Architecture, Biographies," AllRefer.com, http://reference.allrefer.com/encyclopedia/C/Candela.html, 9/7/05

11. "Felix Candela," Huddersfieldgem, http://www.monoculartimes.co.uk/huddersfieldgem/texts/candela.shtml, 9/7/05

12. "Eduardo Torroja," Encyclopedea Brittanica Online, http://www.britannica.com/eb/article-9072985, 9/7/05

13. "Eduardo Torroja y Miret," Structurae, http://en.structurae.de/persons/data/index.cfm?ID=d000039, 9/7/05

14. "Torroja y Miret, Eduardo," Bartleby.com, http://www.bartleby.com/65/to/Torrojay.html, 9/7/05

15. C. Andrade, I. Martínez, M. Ramírez, M. García, "Non Destructive Techniques for On Site Measurements of Reinforcement Corrosion in Concrete Structures," BAM, http://www.ndt.net/article/ndtce03/papers/p017/p017.htm, 9/7/05

16. "Modern Architecture," Archpeda, http://www.archpedia.com/Styles-Modern-5.html, 9/7/05

17. "Who We Are -- The Monolithic Story," Monolithic Dome Articles, http://www.monolithic.com/thedome/whoweare/index.html, 9/7/05

18. "Introduction to the Monolithic Dome," Monolithic Dome Articles, http://www.monolithic.com/thedome/thedome/index.html, 9/7/05

19. "Queensgate Market, Huddersfield," The Tiles and Architectural Ceramics Society, http://www.tilesoc.org.uk/huddmarket.htm, 9/7/05

20. Daryl L. Logan, "A First Course in the Finite Element Method," Third Edition, Brooks/Cole 2002.

21. "NE/Nastran for Windows User Guide," Version 8.3, Noran Engineering, Inc. 2003

22. A.C. Ugural , "Stresses in Plates and Shells," New York : McGraw-Hill, 1981.

23. David P. Billington , "Thin Shell Concrete Structures," Second Edition, McGraw-Hill Publishing Company, 1990.

24. "Eye-Catching New Exterior for Faith Chapel," Monolithic Dome Churches, http://www.monolithic.com/gallery/churches/faith_chapel-paint/index.html, 8/18/05.

25. "Plans Continue for Major Expansion of Faith Chapel," Monolithic Dome Churches, http://www.monolithic.com/gallery/churches/faith_chapel-expan/index.html, 8/18/05.

26. "NE/Nastran and Modeler Tutorial," Version 8.2, Noran Engineering Inc. 2002

Photocopy and Use Authorization

In presenting this thesis in partial fulfillment of the requirements for an advanced degree at Idaho State University, I agree that the Library shall make it freely available for inspection. I further state that permission for extensive copying of my thesis for scholarly purposes may be granted by the Dean of Graduate Studies, Dean of my academic division, or by the University Librarian. It is understood that any copying or publication of the thesis for financial gain shall not be allowed without my written permission.

Signature Nanette South

Date Dec. 20, 2005